UNIVERSITY OF CALIFORNIA

Los Angeles

# Developing the Next-generation Biomedical Optical Systems: Higher Sensitivity, Deeper in Tissue, and Faster Dynamics.

A dissertation submitted in partial satisfaction of the

requirements for the Degree of Philosophy

in Bioengineering

by

Jorge Tordera Mora

2022

ABSTRACT OF THE DISSERTATION

Developing the Next-generation Biomedical Optical Systems:

Higher Sensitivity, Deeper in Tissue, and Faster Dynamics.

by

Jorge Tordera Mora

Doctor of Philosophy in Bioengineering

University of California, Los Angeles, 2022

Professor Liang Gao, Chair

This dissertation proposes several solutions to alleviate two of the most fundamental problems in biomedical optics: imaging deep in tissue via photoacoustic imaging (PAI) and capturing fast dynamics through light field tomography (LIFT). On the one hand, photoacoustic tomography can image with chemical specificity up to tens of centimeters in tissue. However, its applicability is still limited due to its relatively poor sensitivity and noise robustness, high cost, and setup bulkiness. In order to overcome such limitations, I present three novel techniques: Photoacoustic Shadow-Casting Microscopy (PASM), All-optical Photoacoustic Microscopy (AOPAM), and Generalized Spatial Coherence (GSC). First, PASM is a technique that detects biological samples with unprecedented sensitivity by using an optical absorber that acts as a photoacoustic signal

amplifier alleviating photothermal damage in tissue samples while enabling fast acquisition and time-lapse applications. Secondly, AOPAM eliminates the use of conventional piezoelectric transducers in PAI setups by introducing an optical resonating ultrasound sensor: a Fabry-Perot etalon. This configuration allows system miniaturization and expands PAI's applicability to intravascular imaging of atherosclerotic plaques and brain imaging in freely behaving rodents. Thirdly, GSC is a PAI beamforming reconstruction algorithm that takes advantage of spatial coherence between signals from multiple transducers to output state-of-the-art imaging quality metrics and noise robustness compared to gold standard techniques, such as delay-and-sum and similar spatial coherence beamforming techniques such as filtered delay-multiply-and-sum and short-lag spatial coherence.

On the other hand, LIFT is a novel imaging method that allows single snapshot capturing of three-dimensional scenes at ultrafast speeds. In a nutshell, LIFT compresses three-dimensional scenes to one-dimensional detectors in order to enhance acquisition speed by adequately rotating an array of cylindrical lenslets thus reformulating optical imaging as a computed tomography problem. LIFT has depth refocusing and extended depth-of-field capabilities as opposed to classical optical microscopy. In this work, LIFT's application is three-dimensional fluorescent microscopy at kilohertz rates of neuronal action potentials, microfluidic flow sculpting dynamics, and cardiovascular voltage waves.

The dissertation of Jorge Tordera Mora is approved.

Jun Chen

Pei-Yu Chiou

Tzung Hsiai

Liang Gao, Committee Chair

University of California, Los Angeles

2022

*Humbly dedicated to my family, friends, and Lu.*
*Tota pedra fa paret*

**Table of Contents**

**List of Tables**

**List of Figures**

**List of Appendices**

**Acknowledgements**

I would like to first acknowledge and express my deepest appreciation to Professor Liang Gao, my PhD advisor; his guidance, patience, and motivation have been always present throughout this journey. He is simply brilliant. Secondly, I am very grateful to the rest of my dissertation committee: Prof. Jun Chen, Prof. Pei-Yu "Eric" Chiou, and Prof. Tzung Hsiai. Thank you for your time, effort, guidance, and all your constructive comments. Moreover, I am also thankful and had the pleasure to work with and learn from my lab mates and project collaborators.

Finally, I would like to also express my deepest appreciation to my family, friends, and Lu. What a ride.

## Vita

### EDUCATION

**Master of Science in Electrical and Computer Engineering** 2017-2019

University of Illinois at Urbana-Champaign

Champaign, IL

**Bachelor of Science in Telecommunications Engineering** 2013-2017

Universitat Politècnica de València

Valencia, Spain

### CURRENT PUBLISHED MATERIALS

- Mora, J. T., Feng, X., & Gao, L. (2022). Ultrafast light field tomography. In Biomedical Spectroscopy, Microscopy, and Imaging II (Vol. 12144, pp. 29-33). SPIE.
- Mora, J. T., Feng, X., Nyayapathi, N., Xia, J., & Gao, L. (2021). Generalized spatial coherence reconstruction for photoacoustic computed tomography. Journal of Biomedical Optics, 26(4), 046002.
- Mora, J. T., Feng, X., & Gao, L. (2019). Photoacoustic shadow-casting microscopy (PASM). In Novel Techniques in Microscopy (pp. NT3C-4). Optica Publishing Group.
- Mora, J. T., Feng, X., & Gao, L. (2019). Photoacoustic shadow-casting microscopy. Optics letters, 44(15), 3897-3900.

# Chapter 1 Introduction

There are three main limitations associated with the development of the next-generation biomedical optical systems: resolution, depth, and speed. On the one hand, a considerable part of the research community has been focused on improving resolution: how can we image smaller structures? This huge effort led to the discovery optical superresolution techniques that surpass Abbe's theoretical diffraction limit, which states that a light beam can be focused up to approximately half of its wavelength [1]. On the other hand, imaging through deep tissue and fast dynamics have no theoretical but current technological limit. Regarding depth, photons travelling through tissue experiment many scattering and absorption events that prevent imaging in relatively thick tissue. Concerning frame rate, many three-dimensional biological dynamics occur at a millisecond temporal resolution and there are no techniques that can image full field of view, three-dimensional scenes at thousands of frames per second with the scanning device and sensor being the main bottlenecks. Obviously, there is a high need to research and engineer biomedical devices that can capture events in deep tissue and fast dynamics. Thus, during my graduate research I focused on solving these two problems: depth through photoacoustic imaging and speed through optically compressive imaging.

## 1.1 Motivations in optical imaging

Although there already exist well-established biomedical imaging techniques such as ultrasound, Magnetic Resonance Imaging (MRI), X-ray Computed Tomography, and Positron Emission Tomography (PET), it is still highly important to use optical imaging for three main reasons. First, light-matter interaction occurs at a molecular level. Thus, light has an advantageous position to

probe molecules inside our body. Secondly, its wavelength is located at the non-ionizing part of the electromagnetic spectrum. Thus, light does not damage tissue. Third, analogous to other non-optical imaging techniques, optical imaging is capable of functional imaging similar to MRI, metabolic imaging analogous to PET, molecular imaging of gene expressions, and histological imaging. Light is at a unique part of the electromagnetic spectrum and an excellent tool suitable image tissue.

### 1.2 Imaging through turbid media

The main difficulty when imaging through the body is turbidity. Tissue is not transparent and that hampers optical penetration due to photons experiencing multiple scattering and absorption events in a relatively short mean free path. Figure 1 shows a diagram representing how different optical imaging techniques can see through tissue. First, in classical optical microscopy, tissue penetration is limited to a few hundred microns of tissue, at such depths, the wavefront is aberrated and we cannot sharply distinguish tissue features.

Nevertheless, there are more advanced optical imaging techniques that can beat the aberration limit such as confocal microscopy, two-photon microscopy, and optical coherence tomography. First, confocal microscopy employs a pinhole to reject the out-of-focus light that is integrated in the detector allowing three-dimensional imaging by axially scanning the sample. Secondly, two-photon microscopy uses non-linear excitation to reduce the out-of-focus fluorescent excitation and thus enhance optical imaging up to 1mm. Lastly, optical coherence tomography typically uses longer wavelengths for higher tissue penetration (2-3mm). All these applications were enabled by the invention of the laser. Imaging at millimeter depths already enables many applications but the final goal is to be able to image through full body. For instance, tumors that are located a few

millimeters below the skin, where the diffusion limit is, will not be seen by aforementioned techniques.

In my graduate research, I used a technique, mainly developed in the 2000s, able to surpass the diffusion limit enhancing imaging penetration by two orders of magnitude: photoacoustic imaging [2]. This technique uses a combination of optical excitation and ultrasound detection.

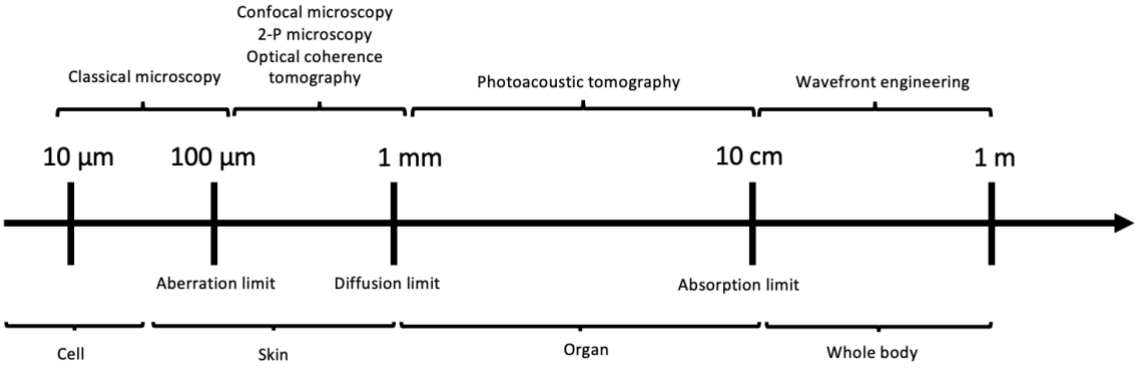

Figure 1: Optical technologies and tissue depth penetration

In photoacoustic imaging, scattering is tolerated and it is absorption what prevents imaging. Thus, we can image up to 10cm deep in tissue, that is where light is completely absorbed by tissue (absorption limit). Lastly, expanding depth imaging to the meter range with high fidelity images has not been achieved yet but there are promising wavefront engineering techniques that might surpass such limit allowing whole body imaging through the use of internal guide stars.

### 1.3 Imaging faster three-dimensional dynamics

High-speed cameras are essential in both fundamental and applied sciences. Many high speed cameras have been already developed but they still lack three-dimensional imaging. In biomedicine, there are many three-dimensional, relatively fast events such as protein folding, neuronal and cardiovascular activity, and microfluidic dynamics that play a fundamental role in the human body. During my graduate research, I focused on imaging three-dimensional fluorescent

activity at thousands of frames per second. To the extent of my knowledge, previous techniques have not been able to image previous dynamics at such frame rate with near full field of view and in 3D. For instance, confocal microscopy relies on axially scanning the sample thus highly reducing the frame rate. Widefield microscopy can only achieve such high frame rates if the sensor's region of interest is reduced but still lacks three-dimensional imaging.

On the other hand, light field imaging has been able to obtain single snapshot three-dimensional images, without relying on scanning techniques, by dividing the main lens aperture into subapertures [3]. Then, each subaperture has a different perspective of the object and a near 3D image can be reconstructed. Note that I mentioned near because it would require a 360 degree view to see around the object. Light field imaging was first introduced by Gabriel Lippmann in 1908 with a concept known as integral photography. Such concept was later revisited by Adelson and Berger with the idea of the plenoptic function [4], a function that describes all the possible information that is captured from a single viewing position; a ray of light can be decomposed by seven parameters: $x$, $y$, and $z$ are the ray coordinates in a three dimensional space. $\theta$, and $\phi$ express ray direction, $\lambda$ is the wavelength of light, and $t$ is a particular time. If we could capture all seven variables, we could exactly represent any scene at any time interval. However, in reality these scenes are normally captured by two-dimensional conventional cameras, one-dimensional line-scan cameras, or zero-dimensional single pixel imagers. In other words, we are encapsulating a high (seven) dimensional object into a low-dimensional detector. Since we cannot currently use a higher dimensional detector, we need to somehow transform the high dimensional function in order to accurately represent the scene. To do so, we cannot practically rely on the classical Nyquist sampling theorem which would require us to use two pixels per voxel, the data cube will be dramatically huge to process. A more efficient idea is to make use of Compressed Sensing (CS)

theory, whose bottom-line is that high dimensional signals can be recovered with high fidelity from low dimensional measurements if the signal is sparse and incoherent in some domain. In this work, I will present Light Field Tomography (LIFT), a compressive technique that allows ultrafast three dimensional imaging and apply it to microscopy in order to image three-dimensional fluorescent activity at thousands of frames per second.

## Chapter 2 Photoacoustic shadow-casting microscopy

Photoacoustic imaging (PAI) is a rapidly emerging biomedical imaging technique that surpasses the optical diffusion limit whose contrast is based on optical absorption instead of scattering, as opposed to other optical imaging techniques. PAI allows centimeter scale tissue depth imaging. When light interacts with tissue, it will absorb its energy and further release it either in form of radioactive decay, fundamental for fluorescence imaging, or non-radioactive decay, meaning it will release heat. Photoacoustic imaging tries to efficiently generate ultrasound waves using light excitation and absorption which produces immediate heat release. In principle, any light absorbing molecule can produce a photoacoustic signal whose origin can be located by using multiple ultrasound transducers or novel photonic integrated circuit detectors (PICs) [5]. However, in practice, it is hard to detect weakly absorbing samples because they are surrounded by thermal, dark, and electric noise sources. In this chapter, I will explain the principles behind photoacoustic imaging and my novel technique: photoacoustic shadow-casting microscopy, which relaxes the high laser power constrain that produces photothermal damage in biological samples and further extends PAI's applicability to, for instance, time-lapse tissue imaging [6].

### 2.1 Fundamentals of photoacoustic excitation

The photoacoustic effect is a physical process in which electromagnetic waves are converted to acoustic waves. From a biological viewpoint, when a tissue or cells absorbs an incoming photon it may release its energy via two paths: radioactive and non-radioactive decay. In radioactive

decay, the absorbed energy will be released in form of another electromagnetic wave but with different wavelength. This is the case of fluorescent imaging (Chapter 5). The latter is essentially thermal energy release. In that case, tissue will absorb light, increase its temperature, rise pressure, and release it via thermoelastic expansion. A key insight in photoacoustic imaging is that, in order to make the ultrasound wave efficiently generated, it is necessary that the duration of the excitation is less than the thermal and stress relaxation times. While thermal relaxation time characterizes the thermal diffusion decay over some tissue region, the stress relaxation time describes how pressure initially propagates. In other words, if the laser pulse duration is less than such times, tissue will heat up and release an acoustic wave before tissue diffuses heat and relaxes stress.

Thermal relaxation time $t_{th}$ is given by Equation 1 [7]:

$$t_{th} = \frac{d_c^2}{\alpha_{th}} \tag{1}$$

where $d_c^2$ is the heated region and $\alpha_{th}$ is the thermal diffusivity. Moreover, stress relaxation time is given by Equation 2:

$$t_s = \frac{d_c}{v_s} \tag{2}$$

where $v_s$ is the speed of sound. For instance, let us assume that we are targeting a 15 μm region, the thermal diffusivity of soft tissue is 1.3E3 $\frac{cm^2}{s}$ , and the speed of sound in tissue is 1400 $\frac{m}{s}$ . Then, $t_{th}$ is 17$s$ and $t_s$ is 1 $\mu s$. This means that we need less than a microsecond pulse to generate efficient photoacoustic signals. In that case, the fractional volume expansion expressed by Equation 3 is negligible:

$$\frac{dV}{V} = -\kappa p + \beta T = 0 \tag{3}$$

where $\kappa$ is the isothermal compressibility, $p$ is the initial pressure, β is the thermal expansion coefficient, and T is temperature. Then, the initial photoacoustic pressure release is:

$$p = \frac{\beta T}{\kappa} \tag{4}$$

which can be rewritten as

$$p_0 = \Gamma \eta_{th} \mu_a^s F_0 \tag{5}$$

where Γ is the Grüneisen parameter, $\eta_{th}$ is the percentage of absorbed energy converted to heat, $\mu_a^s$ is the absorption coefficient of the sample ($cm^{-1}$), and $F_0$ is the laser optical fluence ($J/cm^2$). The initial pressure rise can achieve ~800 Pa from a milliKelvin temperature rise, which is detectable by conventional ultrasound transducers. We can conclude that the initial temperature rise leads to a pressure rise which is later released via thermoelastic expansion and detected by an ultrasound transducer. The overall photoacoustic effect process is illustrated in Figure 2.

Regarding the laser delivery optical design and ultrasound detection configuration, PAI is a scalable technique in which we can target multiple depths, field of view, and resolution depending on the application. In this work, I focused on improving an established modality known as optical-resolution photoacoustic microscopy (OR-PAM) [8]. The typical configuration is shown in Figure 3.

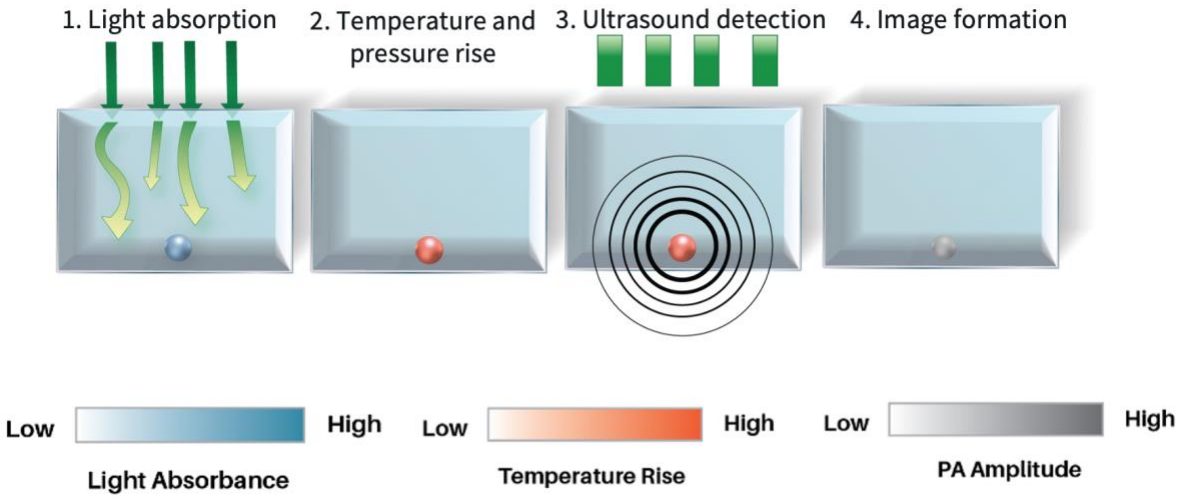


Figure 2: Photoacoustic imaging principle

A laser with selected wavelength depending on the target's absorption spectrum from a given molecule will provide contrast to the image when focused on to an objective lens. Then, the absorber will emit an ultrasound wave that will propagate through tissue and be detected by the ultrasound transducer with the correct acoustic coupling media. Rather than focusing on deep tissue samples, this technique provides a different viewpoint than conventional widefield microscopy: there is chemical specificity since we can choose what to see in the image by selecting the right wavelength. This configuration only provides us single point information so it is necessary to scan the tissue in order to output an image.

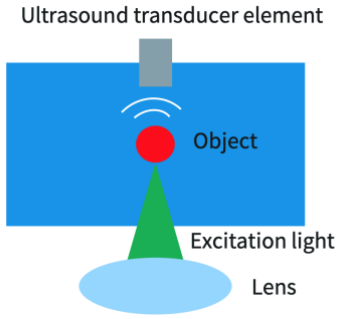


Figure 3: Optical-resolution photoacoustic microscopy

## 2.2 Photoacoustic shadow-casting microscopy principle

Theoretically, any given target will absorb light, increase its temperature and release a photoacoustic wave. However, in practice, weakly absorbers are overwhelmed by environmental noise. A wide range of systems have been focused on improving the sensitivity [9], [10], accuracy [11], and imaging speed [12]. However, such approaches still have a tradeoff between photothermal damage to the sample and the acquisition speed that prevent its applicability. The goal of photoacoustic shadow-casting microscopy (PASM) is to overcome such limitations. PASM is a novel technique that alleviates photothermal damage and enhances acquisition speed by introducing a strong absorber after the biological sample that generates high SNR photoacoustic signals.

PASM's development is inspired on NASA Kepler's mission, where the existence and size of exoplanets is determined by a dip in the brightness of stars. In PASM, the star is the strongly absorbing target and the dip is dictated by the imaged biological sample. Let me first explain this in mathematical terms. The laser fluence at the absorbing background layer $F_0'$ is given by Beer-Lambert's law:

$$F_0' = F_0 e^{-u_a^s d} \tag{6}$$

where $F_0$ is the original laser fluence at the sample stage, $\mu_a^s$ is the absorption coefficient of the specimen, and $d$ is the specimen thickness. As previously mentioned, since OR-PAM does not focus on deep tissue, we can consider the sample as relatively thin. Thus, Beer-Lambert's law can be approximated as a first order term from Taylor's expansion:

$$F_0' \cong F_0\,(1 - u_a^s d)$$

Furthermore, we can also consider that, since the sample is relatively thin, the transducer integrates the signals coming from tissue and the background layer. As a side note, PASM can also work with other PAI modalities with thicker tissue such as acoustic-resolution photoacoustic microscopy (AR-PAM) at the cost of axial resolution. PASM's detected pressure is equal to:

$$p_0' \cong \Gamma\eta_{th}(\mu_a^s + \mu_a^b\,)F_0{}' \tag{7}$$

where $\mu_a^b$ is the absorption coefficient of the background layer. As $\mu_a^b \gg \mu_a^s$, we can further simplify previous Equation 7 into:

$$p_0' \cong \Gamma\eta_{th}\mu_a^b\,F_0{}'$$

Now let us see what is the signal difference between conventional PAM and PASM. Consider that the signal coming from the background layer is:

$$p_0'' \cong \Gamma\eta_{th}\mu_a^b\,F_0 \tag{8}$$

Then, the difference in photoacoustic signals between the background layer and the tissue sample is:

$$\nabla p = p_0'' - p_0' = \Gamma\eta_{th}\mu_a^b\,(F_0 - F_0') = \Gamma\eta_{th}\mu_a^b\mu_a^s\,F_0 d$$

By choosing a background layer with an absorption coefficient $\mu_a^b > 1/d$, then the difference in photoacoustic pressure $\nabla p > p$ and PASM's detected pressure is higher than conventional PAM with a gain factor $M$ given by:

$$M = \frac{\nabla p}{p} = \mu_a^b d \tag{9}$$

### 2.3 System design

Overall, we can consider the PASM system as a minor modification from conventional OR-PAM configuration. This is advantageous because we can obtain higher sensitivity and faster acquisition speed without adding any extra budget. To align the system, we first choose a laser according to the absorbing target. In this case, the ultimate goal is to image hemoglobin (Hb). Thus, the wavelength is 532nm [13]. As Figure 4 shows, there is relatively high absorption at this wavelength from both oxy and deoxyhemoglobin [14].

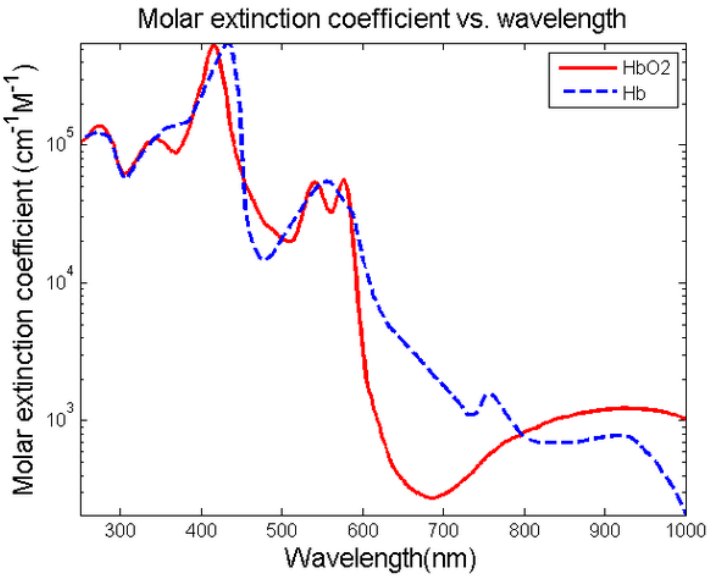


Figure 4: Absorption spectrum of hemoglobin (Hb) [14]

Furthermore, according to stress and thermal relaxation times shown in Equations 1 and 2, it is required no more than a 1 μs pulse duration for targets with similar size to a single red blood cell (RBC). Thus, I chose a nanosecond pulsed laser Elforlight 532nm FQ series which provides up to 400uJ pulse energy with pulsed width durations less than 5ns. PASM's setup is shown in Figure 5. After the laser pulse is fired, the beam is spatially filtered producing homogeneous illumination

at the sample stage and expanded to cover the entire objective's back aperture diameter for diffraction limited spot size at the sample plane.

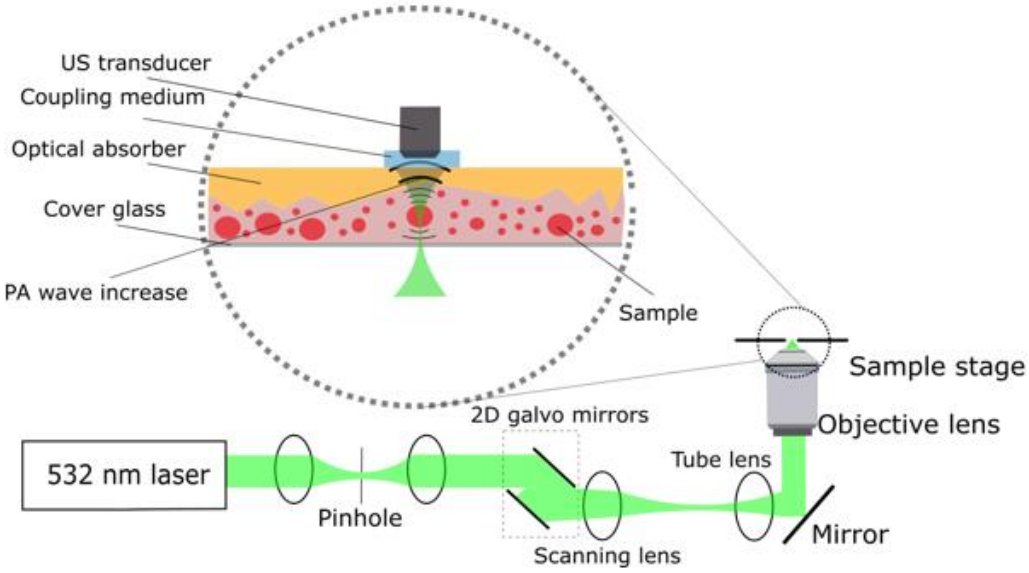


Figure 5: PASM configuration

In order to get an image, it is necessary to raster scan the diffraction limited spot along the objective's field of view, that is why two-dimensional galvanometer mirrors are placed after the spatial filter. Then, a scanning lens is placed at the conjugate plane of the objective lens, the image plane, and one focal length away from the scanning mirrors. This makes the system telecentric: there will be no magnification difference between different scanned points at the sample plane. Lastly, an infinity corrected objective lens and the tube lens act as a conventional microscope.

The zoomed-in circled region in Figure 5 highlights PASM's uniqueness. The biological sample is placed on a thin cover glass. Then, it is sandwiched on the other side with an optical absorbing layer. Such absorber can be any material that strongly absorbs light and emits high SNR ultrasound signal. In this case we choose polymethyl pentene, a transparent thermoplastic that offers a relatively strong acoustic coupling match to help the acoustic signals reach the ultrasound transducer. Finally, water or ultrasound gel is used as a coupling media. The ultrasound signal is

captured by the transducer (Olympus, unfocused, 25MHz central frequency), amplified by two ZFL500NL+ Minicircuit (10-500MHz) in cascade, and digitized by a data acquisition card (GaGe CSE1422, 200MS/s).

Figure 6 shows system's LabVIEW user interface. We select a laser frequency of 1KHz which is synchronized with the scanning mirrors and the digitizer. The number of points (Nx,Ny, Nt) are signals sent to the scanning mirrors that determine the image's field of view and scanning resolution. The amplitude determines the field of view. The sampling rate needs to match Nyquist sampling criteria. The DAQ is externally triggered by each laser pulse at every scanning point within the FOV.

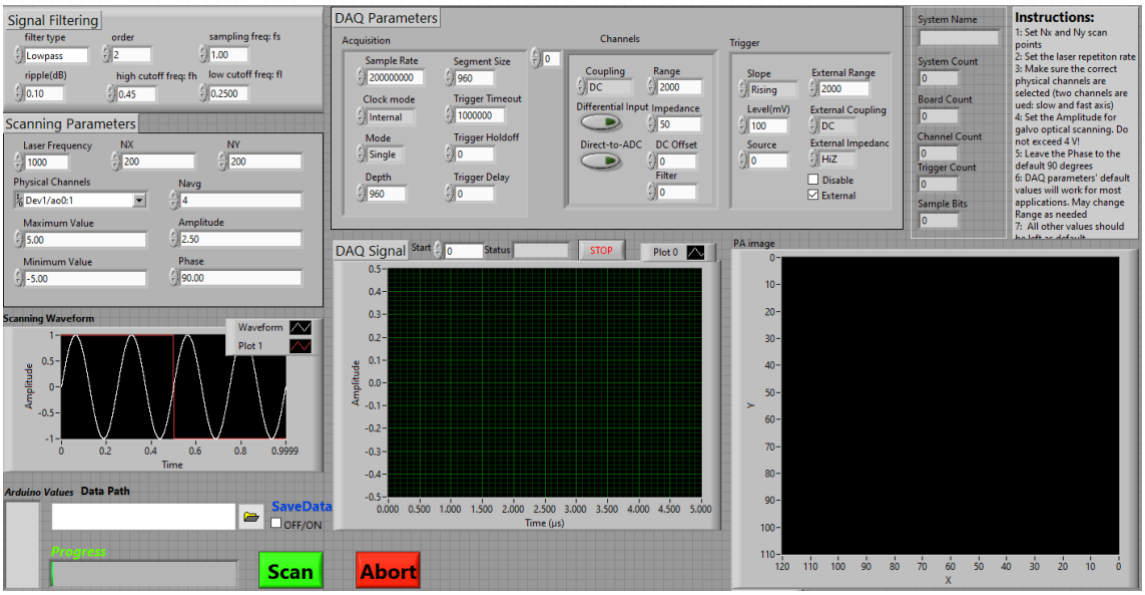


Figure 6: PASM LabVIEW UI

## 2.4 System performance

A 10X, 0.25NA objective lens is used to characterize the system's resolution. In theory, PASM should have the diffraction limited resolution. To probe so, I placed an absorbing USAF resolution target at the sample stage. Then, I scan a relatively small feature and process the image (subfigure in Figure 7).

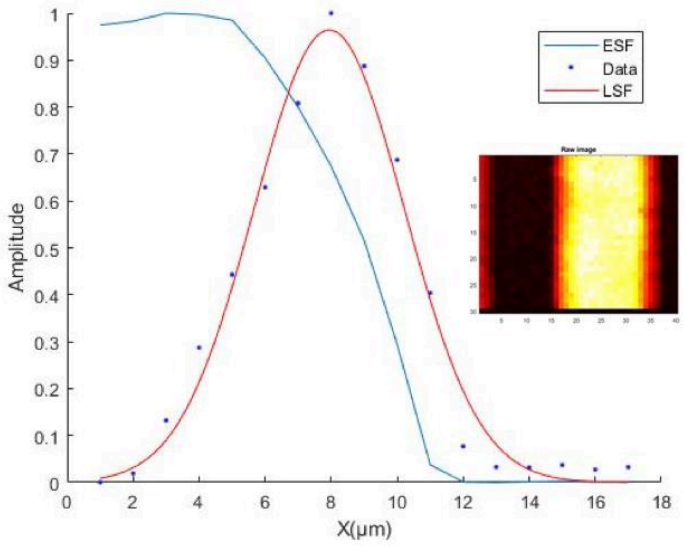


Figure 7: PASM resolution characterization

Figure 7 shows the normalized Edge Spread Function (ESF) of the resolution target in blue, this is the lateral profile. Then, the Line Spread Function (LSF) is derived from the ESF and its full-with at half maximum (FWHM) determines the lateral resolution of PASM's system, which is approximately 5μm. The theoretical resolution is roughly 1 μm so we can consider the system approximately diffraction limited. On the other hand, the axial resolution is determined by the ultrasound's transducer bandwidth, which is 25MHz. Considering that the speed of sound in tissue is around 1500m/s, the axial resolution is 6 μm. Since we are imaging single layers of cells, it is not necessary to experimentally determine it.

### 2.5 Performance evaluation

As a proof of concept, we first need to demonstrate that PASM can achieve better sensitivity, alleviate photothermal damage, and enhance data acquisition speed compared to conventional OR-PAM. To do so, we use 10μm diameter fluorescent beads as weak absorbers since they have relatively low nonradiative thermal energy release approximately equal to $1 - \gamma$, where $\gamma$ is the

fluorophore's quantum yield. To avoid photothermal damage we lower the pulse energy and image using conventional OR-PAM. As shown in Figure 8a, the obtained image is pure noise. This is because the SNR is not strong enough to image the beads. On the other hand, we now place the optical absorber between the sample and the ultrasound transducer to comply with PASM's configuration. As opposed to conventional PAM, PASM (Figure 8b) can image the fluorescent beads due to a high increase of SNR from the optical absorbing layer.

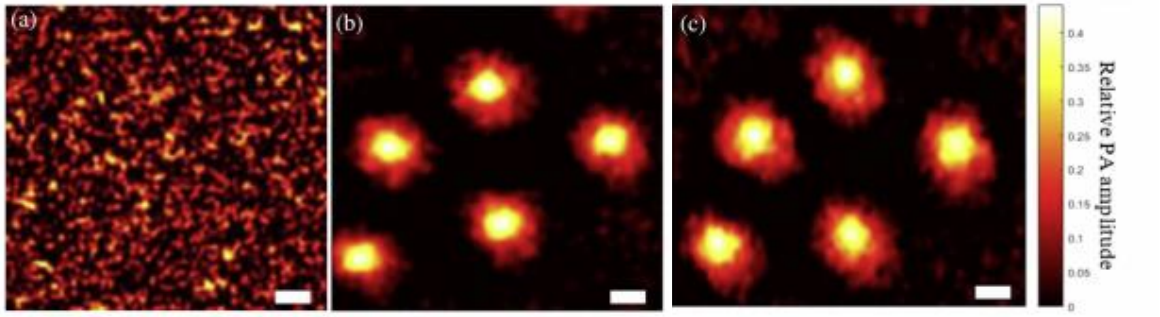


Figure 8: a) PAM fluorescent bead imaging. B) PASM imaging, first scan. C) PASM's tenth scan. Scalebar 10um

To further demonstrate that PASM alleviates photothermal damage in the sample we scan the sample up to ten times and see that the relative photoacoustic amplitude in Figure 8c is still intact. If we were to image the system using PAM and increase the laser power, we would only be able to scan the sample a few times. Thus, PAM is not a suitable technique for time-lapse imaging. Moreover, Figure 9 shows a comparison between raw photoacoustic signals from such fluorescent beads at the sample laser fluence. The blue plot is PAM, which achieves a 15dB SNR and the red plot is PASM's signal, achieving a 50dB SNR. This experiment is proof of concept of PASM's capabilities to highly increase the SNR expanding PAM applications.

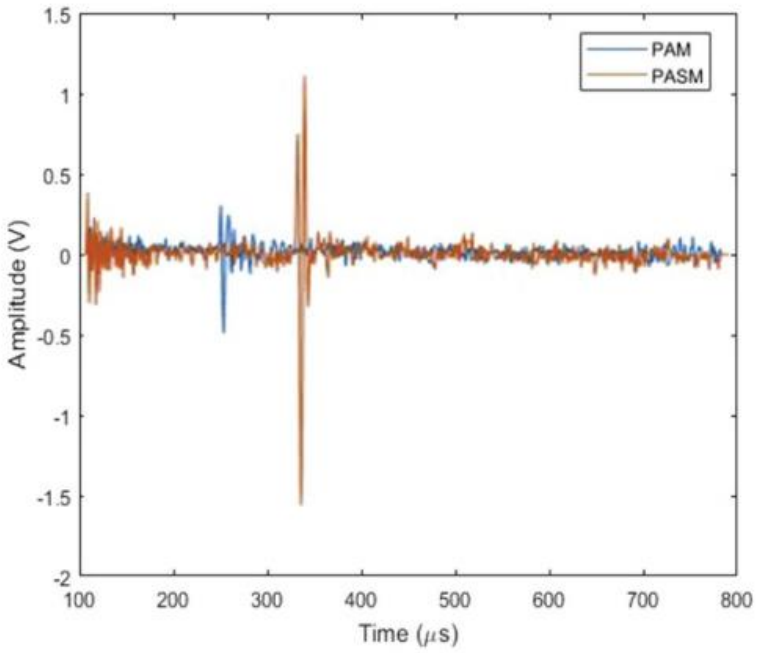


Figure 9: Comparison between PAM and PASM's SNR

### 2.6 Application: red blood cell imaging.

PAI is an ideal candidate to monitor hemoglobin (Hb) for many applications such as pulse oximetry or cancer detection in deep tissue and one of the main absorbers in the human body. In order to demonstrate PASM's capabilities to image biological samples at low laser fluences versus PAM, I imaged red blood cells (RBCs). The chosen sample is a fresh smear of bovine RBCs, we placed a single RBC layer on a 0.17mm cover glass. Similar to the previous fluorescent bead experiment, we lower the pulse laser energy avoiding photothermal damage. PAM's RBC image is shown in Figure 10a. As expected, the SNR is not strong enough to reconstruct the signal. However, when we introduce an optical absorber made of polymethyl pentene (TPX) [15] the SNR highly increases and we can get a high resolution image (Figure 10b).

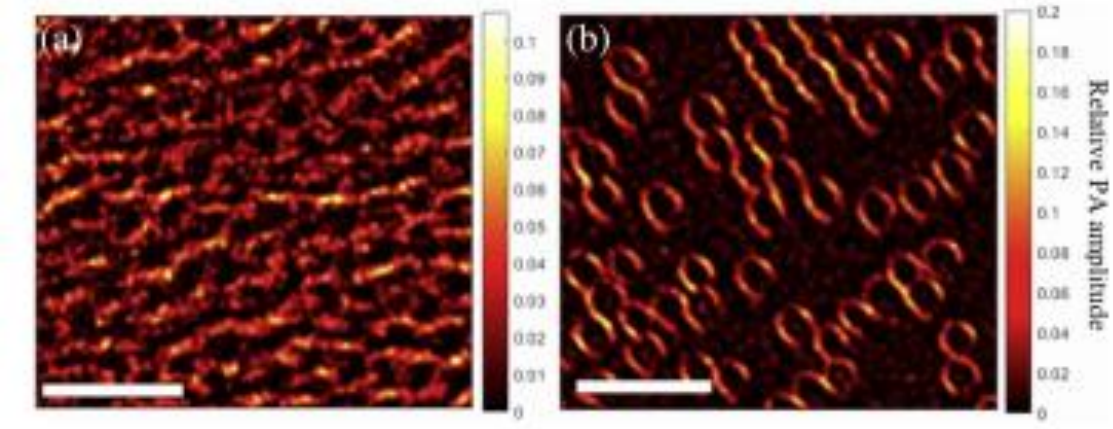


Figure 10: Bovine RBC imaging using a) OR-PAM b) PASM. Scale bar 40um

### 2.7 Discussion and future work

In PAM, there exists a lack of sensitivity at relative low fluences due to the highly inefficient conversion from optical to ultrasound energy [16]. This limits PAM's to many applications that require low laser fluence, inefficient absorbers, fast dynamics, and time-lapse imaging.

In contrast, PASM is an ideal imaging technique for low SNR scenarios and to meet such temporal dynamic requirements. Since PASM does not produce photothermal damage to cells, samples can be imaged many times. PASM maximum amplitude projection images are inverted due to PASM's shadow casting nature. In other words, the optical absorber sets the highest signal value and light that passes through biological tissue generates less photoacoustic signal due to light scattering and absorption events in tissue. Hence the name 'shadow-casting'. PASM is a simple and powerful add-on to PAM. We only need to place a costless optical absorber at the sample stage, which could even be a substitute to the common microscope slide glass seal since glass has a high acoustic impedance mismatch with respect to water/tissue and it introduces unwanted reflections and artifacts. Regarding the material chose for our experiments, TPX was used due to its transparency and acoustic impedance match with the ultrasound transducer and water; however, any thin material that highly absorbs light at the excitation wavelength can be used.

Moreover, in PAM, when avoiding photothermal damage or imaging weak absorber, a common technique to get reliable images is to average the laser pulses at one specific location. Unfortunately, this introduces a data speed acquisition limitation proportional to the number of points acquired per image. In PASM, a single scan is enough to get high quality metrics. Thus, it is an ideal candidate for high-speed photoacoustic microscopic imaging.

Furthermore, PASM could also be used for low-cost PAI systems. Typically, nanosecond pulsed lasers are used to generate high enough signals to output an image. Continuous wave lasers with frequency modulation is a cheaper alternative that suffers from low SNR [17]. PASM could compensate for that loss with the use of an optical absorber. PASM might also eliminate the need to use contrast agents in certain tissue imaging experiments. Typically, weakly absorbers are loaded with exogeneous contrast agents such as gold nanoparticles to highly increase the SNR [18], [19].

In conclusion, PASM is a novel technique that provides unprecedented sensitivity in imaging biological samples compared to similar techniques. By using a highly optical absorber close to the tissue, an integrated ultrasound signal is obtained at the transducer. The signal is inverted with respect to conventional PAM: a high absorber will be shown as a lower signal in the final image since less laser fluence hits the optical absorbing layer at such position.

# Chapter 3 All-optical photoacoustic imaging

While the last chapter focused on photoacoustic shadow-casting microscopy, a technique that can change the system's sensitivity without changing the sensor there is still a highly need to change the architecture of photoacoustic imaging systems for several reasons. For instance, many applications such as brain or intravascular imaging require sensor miniaturization which is nontrivial when using conventional piezoelectric ultrasound transducers due to the active element's sensitivity being proportional to its area, bulky casing, isolation material, and preamplifiers [20]. This is where the idea of using optical sensors to have miniaturized and more sensitive photoacoustic imaging systems comes from. Hence the name 'all-optical photoacoustic imaging' [21], ultrasound transducers are the non-optical element in a conventional PAI setup. In all-optical PAI, we will use optical excitation, ultrasound emission, and optical detection with interferometric resonance detectors. The fundamental basis of optical resonating photoacoustic sensors is that we can create a resonance using multiple optical cavity architectures such as whispering galleries modes [22], [23] or Fabry-Perot etalons [24] and later detect a shift in the resonant frequency when an ultrasound waves interacts with the sensor. In this chapter, I will explain the fundamentals of such sensors and explain the fabrication process of a Fabry-Perot sensor for photoacoustic imaging.

## 3.1 Fabry-Perot ultrasound sensors

Fabry-Perot architecture is one of the simplest forms of resonant cavities. Figure 11 shows an schematic Fabry Perot ultrasound sensor in an all-optical photoacoustic imaging setup. In a nutshell, a spacing layer is sandwiched between two mirrors, the interrogation laser reflects from both mirrors creating interference and a resonance. An ultrasound wave from tissue produced by

the laser excitation's wavelength travels to the Fabry-Perot sensor through an impedance matching layer (water), passes through the first mirror of the cavity, and reaches the spacer. The spacer should be fabricated from a material that has relatively Young's modulus such that changes its length when being pushed by the ultrasound wave so that it modifies the resonant cavity properties. The sensor's sensitivity is given by [25]:

$$S = \frac{dP_r}{dp} = I_s A_s \tag{10}$$

Equation 10 shows that the sensitivity depends on $P_r$, the optical power modulation's rate of change with respect to the change in pressure $p$ due to thermoelastic expansion explained in Chapter 1. Then, the overall sensitivity is a combination of optical and acoustic sensitivity: $I_s$ and $A_s$, respectively. Let me address each one separately in the following subsections.

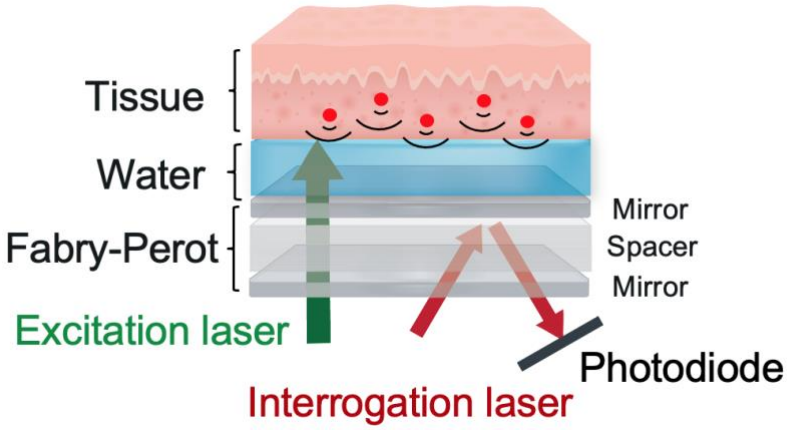


Figure 11: All-optical PAI with Fabry-Perot ultrasound sensor

### *3.1.1 Optical sensitivity*

Equation 11 shows the optical phase after light wave has completed one roundtrip starting from first mirror, spacer, second mirror, spacer, and back to the first mirror.

$$\phi = \frac{4\pi nl}{\lambda} \tag{11}$$

It can be inferred from Equation 11 that if the cavity parameters are fixed and there is no incident ultrasound wave, the only parameter that will affect resonance is wavelength. Figure 12 shows the interferometric transfer function (ITF) simulation of the Fabry-Perot sensor, which shows how the cavity behaves then scanning different wavelengths [24]:

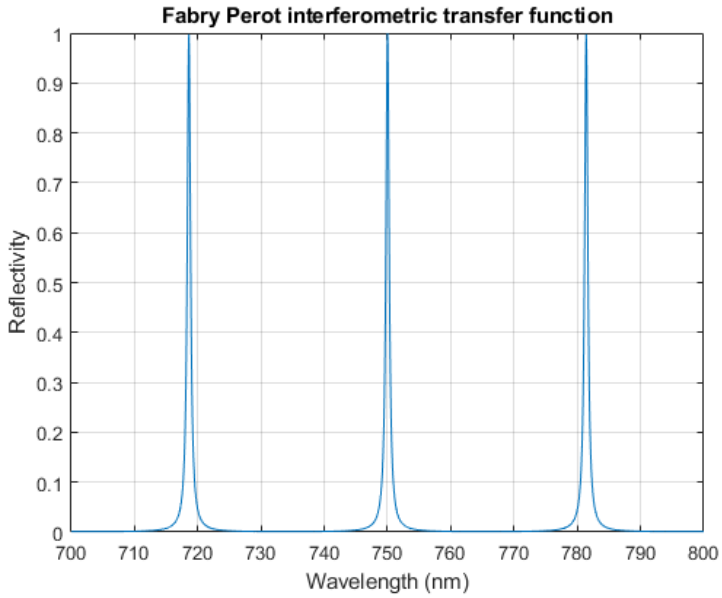


Figure 12: Interferometric transfer function of Fabry-Perot ultrasound sensor

From this graph we can extract that if we have a tunable laser source and we set the frequency to the highest slope of $dR/d\lambda$, a small change in the incident pressure could potentially cause a change in the reflectivity. Two main parameters can be inferred from the interferometric transfer function (ITF): free spectral range (FSR) and FWHM. The former indicates what is the frequency range between two resonant peaks while the latter showcases how strong and sensitive is each resonant peak.

For photoacoustic sensing purposes we need to make sure that the FSR is wide enough so that there is only one peak within the measuring range, otherwise we would have undetermined dynamic range scale. Secondly, the FWHM should be small enough that we can sense photoacoustic waves but big enough so that the Fabry-Perot does not saturate, that means transitioning from resonant to non-resonant state with a minimal amount of pressure. This ultimately depends on the reflectivity of the mirrors in the cavity [26].

### *3.1.2 Acoustic sensitivity*

Acoustic sensitivity can be described as how much does the phase delayed with upcoming pressure changes [27], [28]. This is shown in Equation 12 :

$$\mathrm{A_s} = \frac{\mathrm{d}\phi}{\mathrm{dp}} \tag{12}$$

which can be expanded as:

$$\mathrm{A_s} = \frac{\mathrm{d}\phi}{\mathrm{dp}} = \frac{4\pi \mathrm{nl}}{\lambda}\frac{1}{\mathrm{E}}\left(1 + \frac{\mathrm{n}^2 \mathrm{p}\sigma}{2}\right)|\mathrm{P_I(k)}| \tag{13}$$

where $n$ is the refractive index, $l$ is the Fabry-Perot spacer thickness, $E$ is the spacer Young's modulus, $p$ is the photoelastic constant, σ is the Poisson ratio, and $|P_I(k)|$ is an acoustic frequency dependent term that is inversely proportional to the acoustic's frequency. Thus, as we set a thickness value or the cavity, there is a trade-off between acoustic sensitivity and sensor's bandwidth.

### *3.1.3 Fabry-Perot sensor configuration*

The sensor's configuration is as follows: the first mirror is made of a dielectric thin film stack of alternating layers of relative low and high refractive index materials to transmit the excitation wavelength and reflect the interrogation wavelength. Since the mirror is not 100% reflective, some light will couple into the cavity, made of Parylene C and reflect back from second mirror, which is made of the same material as the first. Let me first introduce the idea behind the thin film stack mirror for Fabry-Perot ultrasound resonating sensors [29] , shown in Figure 13:

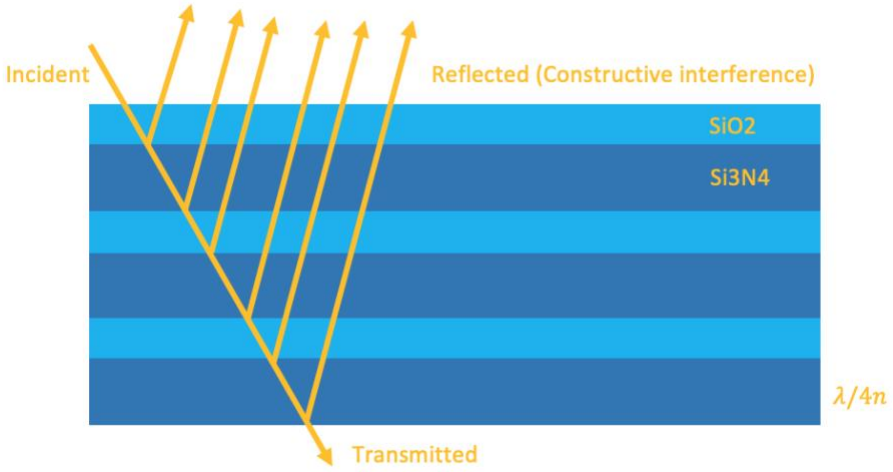


Figure 13: Bragg mirror concept

Light traveling from air encounters a higher refractive index material. The refracted wave experiences a 180° phase shift and travels through the material until it encounters another lower refractive index material. When light is traveling from high to low index there is no phase shift. Furthermore, part of this wave will be reflected and will interact with the reflected wave from the first air-high index refractive material creating constructive or destructive interference. The condition to create destructive interference is:

$$2t = \frac{m\lambda}{2n} \tag{14}$$

where $t$ is the material thickness, $m$ is the order, $\lambda$ is the wavelength of light, and $n$ is the refractive index. In such case, there will be no reflected wave and full transmission. Interference is the basis behind such high reflectance mirrors. We will create a stack of double layers of high and low refractive index materials with  quarter wavelength thickness. The choice of the materials is such that reflects ~770 nm, which is within interrogation laser tunable wavelength range and the bandwidth is proportional to the difference between refractive indices. The number of double layers is eight due to the required reflectivity >97% to produce an strong resonance in the cavity. Unless otherwise noted, incident light is always normal to the surface of the Fabry Perot sensor. The sensor is designed for two different wavelengths: excitation and interrogation. While the excitation wavelength is targeted to generate efficient photoacoustic waves at the tissue's peak absorption, interrogation is to probe the sensor. In this particular application, we choose to target hemoglobin imaging so the excitation wavelength is 532nm.

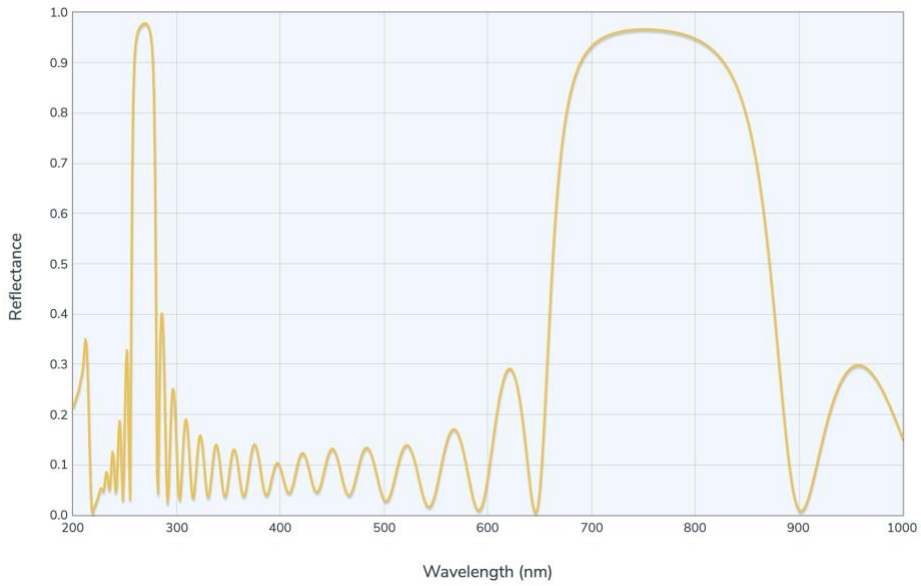


Figure 14: Bragg mirror reflectance spectrum

Figure 14 shows the mirror's reflectance spectrum. As it can be seen, it is designed to have its peak wavelength and 770nm and transmit 532nm. It is made of double layers of silicon nitride (n = 2.04), as the high refractive index material and silicon dioxide (n = 1.45) as the low. Each layer $t = \frac{\lambda}{4n}$ is 93nm and 130nm thick, respectively, and the total mirror thickness is 1.7µm. Furthermore, the selected thickness of the Parylene C is 20µm to strike a balance between acoustic sensitivity and desired bandwidth (20MHz). After the second mirror is built, we will also add a thin layer of Parylene C to protect the sensor from the water coupling media. The overall sensor design is shown in Figure 15.

Lastly, the selected substrate is polymethylmethacrylate (PMMA). Its function is the same as a backing stub material in conventional ultrasound transducers: avoid reflections and attenuate the signal. This means that there must be an acoustic impedance match between Parylene C and the substrate since the mirror is not considered due to the thickness size compared to the acoustic frequency and the substrate must attenuate the ultrasound signal to avoid further reflection. Thus, the substrate thickness is 1cm.

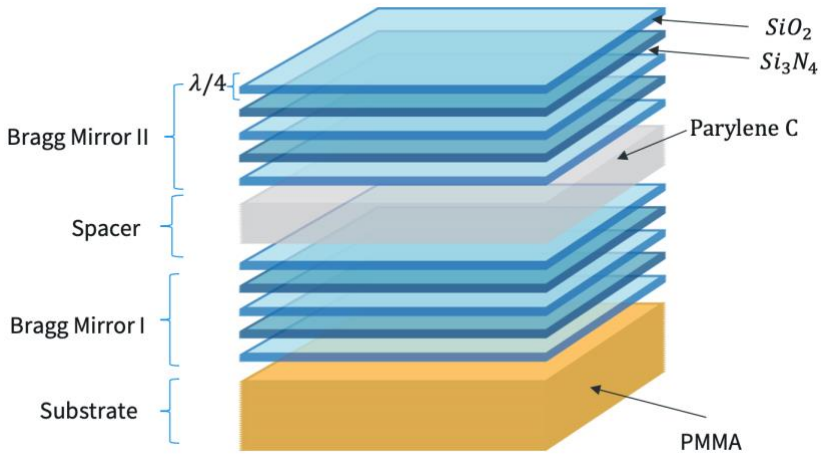


Figure 15: Fabry Perot sensor configuration

### *3.1.4 Fabry-Perot sensor fabrication*

The entire fabrication process must be done at relatively low temperature since the melting point of the PMMA substrate is 160°C . Hence, material deposition is performed through plasma-enhanced chemical vapor deposition (PECVD) [30]. Conventional chemical vapor deposition techniques use high temperature to provide enough energy for the deposition reaction. In a PECVD setup, show in Figure 16, plasma provides the energy and the substrate is placed on a platen. At the top of the chamber there is a gas inlet and a high voltage radiofrequency (RF) source which provides sufficient energy to produce plasma. Once RF source activates the plasma, the gases inside the chamber become chemically reactive and a thin film is created at the sample. The gas selection will depend on the desired deposited material.

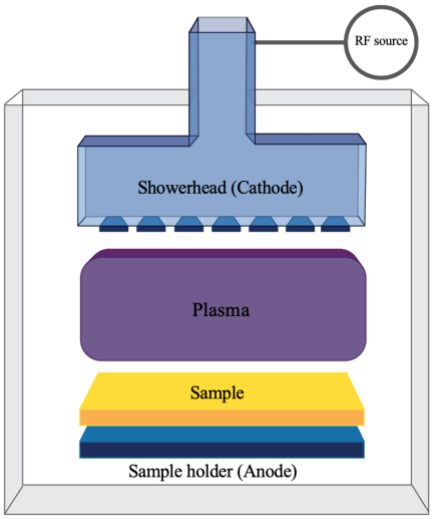


Figure 16: Plasma-Enhanced Chemical Vapor Deposition process

I empirically calculated the deposition rate by placing a test target and depositing silicon nitride and silicon dioxide for thirty minutes. Then, the thickness is calculated according to its reflection spectrum. After the first mirror is fabricated, the sensor is translated to a Parylene C coater machine [31]. Such coating process has three main steps: sublimation, pyrolysis, and polymerization. In

sublimation, the Parylene C dimer is placed in a boat-like structure and partial vacuum. Temperature is risen to 150°C and the dimer is converted to gas. Then, the gas dimer is further heated to 690°C until its molecular shape and the dimer is split into monomers. Finally, the sensor is placed at the polymerization chamber at room temperature where monomers form chain like structures and are deposited on the sensor. Figure 17 illustrates this process. Lastly, after Parylene C is coated, the sample is brought back to the PECVD machine where I deposited the second mirror.

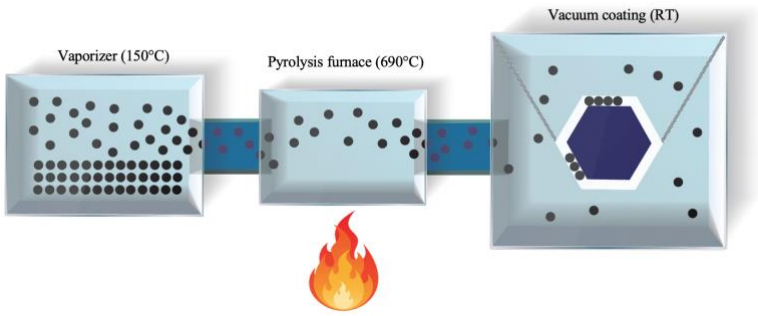


Figure 17: Parylene C deposition process

### *3.1.5 Fabry-Perot sensor test*

The Fabry-Perot sensor is tested according to Figure 11. A tunable laser source (TLB-6712 Velocity, New Focus) is used to interrogate the laser from 760nm to 780nm and create a strong resonant dip. Once we have a map of the spectral response of the sensor, we can set the sensing wavelength at the maximum slope of the interferometric transfer function (ITF). That is the most sensitive point where incident pressure will cause a change in the system's reflectivity. The experimental ITF is shown in Figure 18 and the selected resonant wavelength is 775.23nm. Furthermore, on the other part of the sensor, water is used as a coupling media and electrical tape is used as an optical absorber to produce high SNR PA signals.

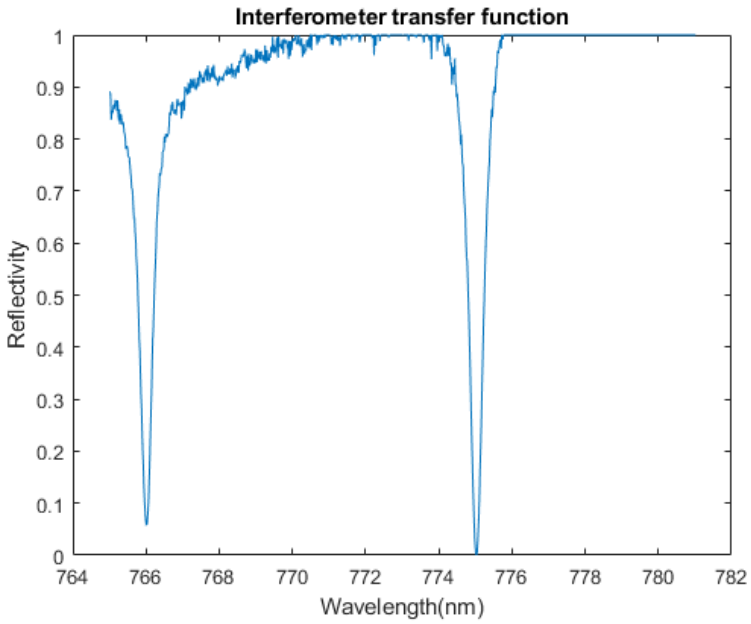


Figure 18: Experimental Interferometric Transfer Function

As it can be seen in Figure 19, the Fabry-Perot sensor is able to sense photoacoustic signals, the arrow indicates the characteristic bipolar ultrasound signals. The frequency response (20MHz) is calculated by calculating the Fourier transform of such pulse.

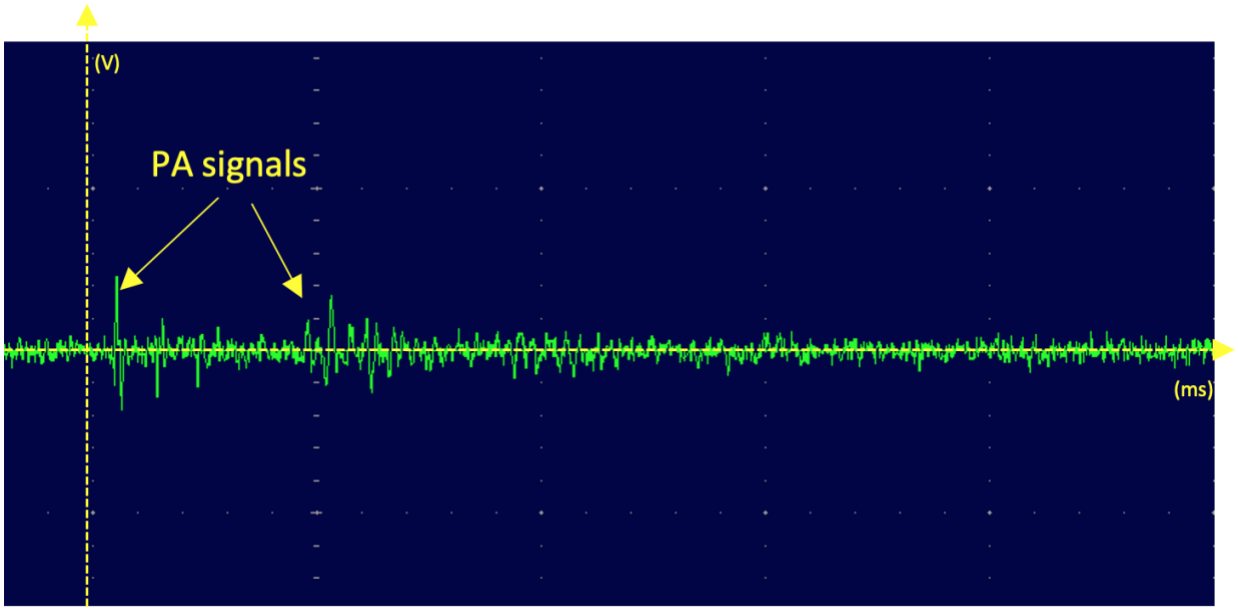


Figure 19: Fabry-Perot sensor PA signals as a proof of concept

### *3.1.6 Conclusions and future work*

The main advantage of all-optical photoacoustic systems with respect to conventional ultrasound transducers is that it enables many different applications due to its scalable miniaturization and high sensitivity. For future work, we will work on intravascular of atherosclerotic plaques and functional brain imaging. On the one hand, due to vulnerable atherosclerotic plaque rupture there are many cardiac deaths and strokes. In 2015, the World Health Organization estimated that out of the nearly 20 million cardiovascular deaths worldwide, 6 where due to coronary heart attack and 7 due to stroke [32]. Atherosclerotic plaque vulnerability is related to its chemical composition, stress distribution, and inflammation. The key of intravascular imaging is miniaturization and the Fabry-Perot sensor can potentially provide that. Currently, the gold standard technique to image atherosclerosis is intravascular ultrasound (IVUS) [33]. However, IVUS can only provide around 100 μm resolution at 40MHz and only structural information so it is hard to distinguish soft tissue and fat. Moreover, IVUS cannot be introduced in smaller vessels and capillaries since reducing the transducer's size also reduces its active sensing element producing a sensitivity loss. To enable both structural and molecular imaging we will build a multimodal technique using optical coherence tomography (OCT) and PAI [34] for atherosclerotic plaque intravascular imaging. This is shown in Figure 20.

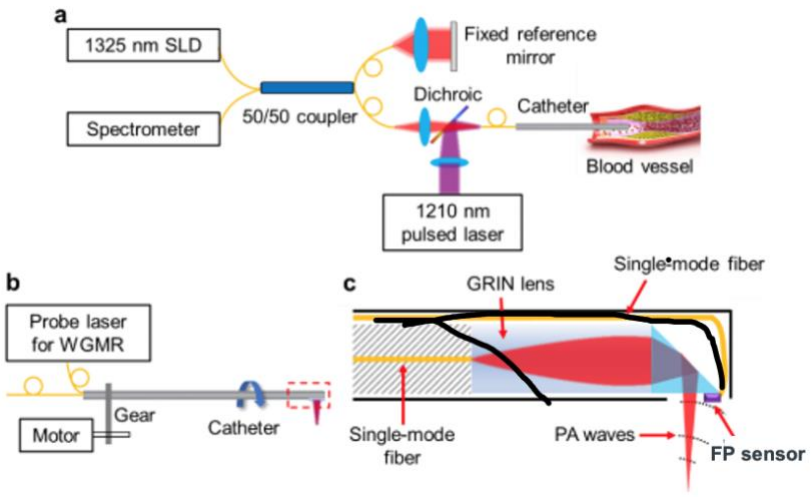


Figure 20: Multimodal OCT and PACT probe for intravascular imaging

Figure 20a shows the OCT subsystem. A super luminescent diode (SLD) centered at 1325nm maximizes tissue penetration and the 1210nm laser is used for photoacoustic excitation. The OCT light source is then coupled into a single-mode fiber and focused onto tissue using a gradient refractive index (GRIN) lens. Then, OCT signals from tissue interfere with the fixed reference mirror and a spectral interferogram is analyzed after passing through the spectrometer. Moreover, PA waves are detected by the Fabry-Perot sensor and sent to the detector. Since this configuration only provides one pixel at a time we can use a motor to rotate the catheter probe and image both the structure and composition (Figure 20b).

Moreover, our Fabry Perot could be potentially used for freely behaving mouse brain imaging [35], [36]. It has already been demonstrated PAI's feasibility to do functional deep brain imaging compared to conventional optical techniques[37]. Figure 21 shows our proposed application:

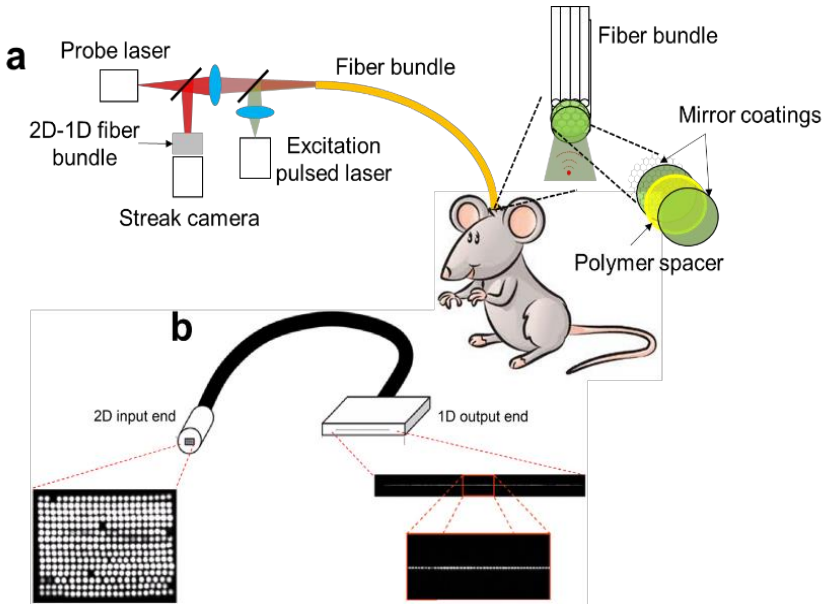


Figure 21: PACT probe for brain imaging in freely behaving animals

Figure 21a shows excitation and probe (interrogation) lasers as previously explained in Figure 20. A fiber bundle, shown in Figure 21b maps the 2D input from each spatial position from the Fabry-Perot sensor into a one-dimensional streak camera which would enable high speed imaging. The use of a fiber bundle and the miniaturized optical sensors enables freely moving since the probe can be attached to head with low impact unlike conventional ultrasound transducer arrays.

In conclusion, all-optical photoacoustic imaging enables many applications compared to conventional ultrasound transducers due to its size independence. A miniaturized sensor can be used for intravascular and brain imaging applications. There are different optical resonant architectures that can be used as ultrasounds sensors. The selection of the Fabry-Perot sensor is simple but powerful: it does not involve complicated fabrication process, and it is easily repeatable so that it could be translated to clinical scenarios as opposed to whispering gallery mode resonators, which are also commonly used in research. My main goal with this research project was the proof of concept so that it can be later used for aforementioned applications in our laboratory.

## Chapter 4 Generalized Spatial Coherence for Photoacoustic Tomography

In this chapter, I will present a novel algorithm to reconstruct photoacoustic signals using conventional ultrasound transducers and optical resonators for ultrasound sensing (Chapter 3). There already exist many beamforming ultrasound reconstruction algorithms with multiple sensor geometries such as spherical, circular, and linear [38], [39]; from simple backprojection (delay and sum) [40] to time-reversal approaches [41], f-k migration [42], [43], adaptive minimum variance [44], [45], to even deep learning-based algorithms [46]. However these methods still do not show an optimal noise robustness and photoacoustic signals that are generated at deeper regions in tissue cannot be imaged due to low light fluence and weakly absorbers are buried in noise. To overcome such limitations, spatial coherence beamforming techniques, which take advantage of correlation calculation between transducer elements, were studied. In this chapter, I will first present the standard reconstruction algorithm, delay-and-sum. Then, I will deepen into spatial coherence algorithms that enhance imaging quality metrics, mainly resolution and contrast. Lastly, I will explain my algorithm, generalized spatial coherence, and demonstrate how it performs compared to delay-and-sum and similar spatial coherence reconstruction techniques.

### 4.1 Delay-and-sum reconstruction.

Delay-and-sum is the most basic and common reconstruction algorithm in ultrasound imaging. Since in PACT we reconstruct the signal using multiple transducers, same principles apply. Figure 22 shows an absorber emitting a photoacoustic wave which is detected by an array of ultrasound transducers. Delay-and-sum (DAS) reconstruction algorithm exploits the fact that the signals will arrive at different transducers at different times. Then, since the speed of sound and the spatial location of each transducer are known, the signal is time delayed for each transducer and summed. This is shown in Equation 14, the DAS beamforming equation:

$$y_{DAS}(n) = \sum_{i=1}^{N-1} s_i(n) \tag{14}$$

where $s_i(n)$ is the delayed PA signal from the $i-th$ transducer element at the $n-th$ sample. Although DAS is a gold-standard algorithm, its signal-to-noise ratio and imaging quality is known to be fairly low due to its simplified modeling of ultrasound propagation in tissue and its lateral resolution is limited by the ratio of the main to the side lobe levels.

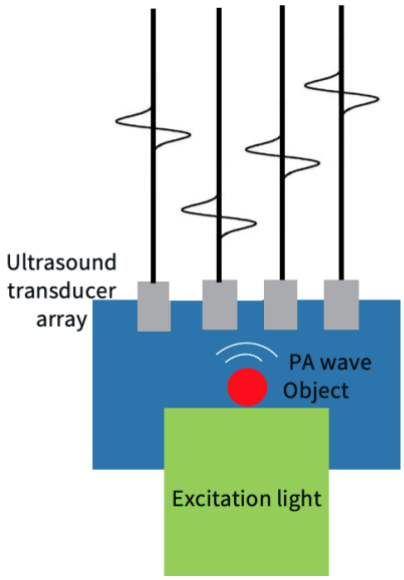


Figure 22: Delay-and-sum beamforming algorithm

### 4.2 Algorithms employing spatial coherence

In order to improve imaging quality, some algorithms have previously employed spatial coherence, a fundamental property of waves, to abate noises exploiting the fact that noise and side lobes do not interfere coherently [47]. For instance, [48] used a phase and sign coherence to weight the DAS' output for ultrasound imaging. Currently, there are two main algorithms that use spatial coherence of ultrasound waves as a contrast source: filtered delay-multiply-and-sum (FDMAS) [49], [50] and short lag spatial coherence (SLSC) [51]. Both algorithms have been used separately for PACT and combined with each other [52]–[62]. In this section we will visit these algorithms

in depth and identify their major advantages and disadvantages that will then lead to my algorithm: generalized spatial coherence (GSC).

FDMAS is a modified version of DAS that adds a multiplication step between the delayed signals and posterior filtering. Multiplying signals from different transducers is essentially computing a spatial correlation operation that implicitly incorporates information about the spatial coherence between signals. DMAS' equation is shown below:

$$y_{DMAS}(n) = \sum_{i=1}^{N-1} \sum_{j=i+1}^{N} sign\left[s_i(n)s_j(n)\right] \sqrt{\left|s_i(n)s_j(n)\right|} \tag{15}$$

where $sign()$ is the signum function and $N$ is the number of transducers in the array. In this way, the ultrasound signals can maintain its sign and be correctly scaled to the same dimensionality. Furthermore, while DAS outputs a zero-mean signal similar to the original signal amplitude spectrum, DMAS multiplies signals with the same frequency content generating two output signals, one being the same as with DAS, centered at $f - f_0 = 0$ and a second harmonic component centered at $f_0 + f_0 = 2f_0$. Thus, an bandpass filtering step can be added to maintain the higher frequencies and attenuate the lower ones.

Compared to DAS, FDMAS provides better resolution due to the wavelength decrease as a consequence of the multiplication step and the second harmonic frequencies. Also, it has more noise robustness due to the use of the correlation operation that effectively increases the synthetic aperture. To put this in mathematical terms we can first rearrange terms in Equation 15 in Equation 16, where the absolute value operator will be shown implicitly and aforementioned filter will be added:

$$y_{FDMAS}(n) = h_1(n) * \sum_{i=1}^{N-1} \sum_{j=i+1}^{N} \frac{s_i(n)s_j(n)}{\sqrt[4]{s_i^2(n)s_j^2(n)}} \tag{16}$$

where $h_1(n)$ is the bandpass filter, and $*$ denotes the convolution operation defined as:

$$[f * h](n) = \sum_{\tau=-L}^{L} f(\tau)h(\tau - n) \tag{17}$$

On the other hand, SLSC is an algorithm based on the same principle, taking advantage of the spatial coherence between multiple signals but with a different route taken. This algorithm was presented to compete with DAS. SLSC's beamforming equation uses normalized spatial coherence directly as the imaging contrast. The normalized spatial coherence at an arbitrary lag $m$, number of separation elements between transducers, is given by Equation 18:

$$R(m) = \frac{1}{N-m} \sum_{i=1}^{N-m} \frac{\sum_{n=n_1}^{n_2} s_i(n) s_{i+m}(n)}{\sqrt{\sum_{n=n_1}^{n_2} s_i^2(n) \sum_{n=n_1}^{n_2} s_{i+m}^2(n)}} \tag{18}$$

The kernel size $K = n_2 - n_1$ is selected to strike a balance between correlation calculation and axial resolution. The first $M$ lags are summed while reaching a balance between lateral resolution and signal-to-noise ratio (Equation 19) [63]. As expected, SLSC has lower point resolution than FDMAS but its spatial covariance calculations makes it have higher noise robustness.

$$RI = \sum_{m=1}^{M} R(m) \tag{19}$$

Generally, both FDMAS and SLSC have advantages with respect to DAS but still have drawbacks that limit their applicability. On the one hand, SLSC discards signal magnitude evidence by normalizing the coherence values between multiple transducers. For instance, quantitative information might be useful for one of PACT's main applications: blood oxygenation measurements. On the other hand, FDMAS increases imaging contrast compared to DAS without losing signal magnitude relative strength but has lower contrast-to-noise ratio for reasons that are still not fully understood [64] and will be explained later.

For such reasons, I present Generalized Spatial Coherence (GSC) beamformer [65], a novel reconstruction algorithm that combines the strength from previous spatial coherence beamforming techniques and generalizes them into a single equation. Compared to DAS, FDMAS, and SLSC, GSC provides superior imaging quality metrics.

### 4.3 Generalized Spatial Coherence beamforming equation

First, I will rewrite FDMAS' beamforming Equation 16 to make it similar to SLSC's equation and make the comparison between both algorithms obvious.

$$y_{FDMAS}(n) = \sum_{m=1}^{N-1} \sum_{i=1}^{N-m} h_1(n) * [s_i'(n) s_{i+m}'(n)] \tag{20}$$

where $s_i'(n) = \frac{s_i(n)}{\sqrt[4]{\sum_{n=n_1}^{n_1} s_i^2(n)}}$. In other words, FDMAS is a technique that adds all lags up to $N-1$. Similarly, we can rewrite Equation 20 as:

$$\begin{aligned} RI &= \sum_{m=1}^{M} \frac{1}{N-m} \sum_{i=1}^{N-m} \frac{\sum_{n=n_1}^{n_2} s_i(n) s_{i+m}(n)}{\sqrt{\sum_{n=n_1}^{n_2} s_i^2(n) \sum_{n=n_1}^{n_2} s_{i+m}^2(n)}} \\ &= \sum_{m=1}^{M} \frac{1}{N-m} \sum_{i=1}^{N-m} \sum_{n=n_1}^{n_2} \frac{s_i(n)}{\sqrt{\sum_{n=n_1}^{n_2} s_i^2(n)}} \frac{s_{i+m}(n)}{\sqrt{\sum_{n=n_1}^{n_2} s_{i+m}^2(n)}} \\ &= \sum_{m=1}^{M} \frac{1}{N-m} \sum_{i=1}^{N-m} \sum_{n=n_1}^{n_2} h_2(n) * [s_i'(n) s_{i+m}'(n)] \end{aligned} \tag{21}$$

where $s_i'(n) = \frac{s_i(n)}{\sqrt[2]{\sum_{n=n_1}^{n_2} s_i^2(n)}}$ and $h_2(n) = [1, 1, \dots, 1]$, a low-pass filter. Now the differences between FDMAS (Equation 20) and SLSC (Equation 21) are obvious and we can generalize both into a single equation:

$$y(n) = \sum_{m=1}^{M} w(m) \sum_{i=1}^{N-m} h(n) * \{g[s_i(n)]g[s_{i+m}(n)]\} \tag{22}$$

where $w(m)$ represents a weight function, $h(n)$ is a filter, and $g[s_i(n)]$ is given by:

$$g[s_i(n)] = \begin{cases} \dfrac{s_i(n)}{\sqrt[4]{\sum_{n=n_1}^{n_1} s_i^2(n)}}, \text{FDMAS} \\ \dfrac{s_i(n)}{\sqrt[2]{\sum_{n=n_1}^{n_2} s_i^2(n)}}, \text{SLSC} \end{cases}$$

Let us take a closer look at function $g[s_i(n)]$ in Equation 22. It highlights the key differences between FDMAS and SLSC. In the upper function, FDMAS can preserve the signal magnitude due to the use of a weaker normalization factor compared to SLSC. We can name this quasi-normalization through fourth root. On the other hand, SLSC uses a more aggressive normalization (square root) that loses amplitude signal information. Furthermore, SLSC has a stronger robustness to noise due to the use of a larger kernel, it takes more samples in the time domain to calculate correlation. This does not happen in FDMAS with a one kernel that introduces noise in the coherence calculation [66]. We can further prove this; let us consider a real photoacoustic signal $\mathrm{s}_i(n)$ that arrives at a transducer element as a sum of the original signal $\mathrm{f}_\mathrm{i}(n)$ and uncorrelated noise $\Phi_\mathrm{i}(n)$ [67]:

$$\mathrm{s}_i(n) = \mathrm{f}_\mathrm{i}(n) + \Phi_\mathrm{i}(n) \tag{23}$$

Then,

$$\sum_{n=n_1}^{n_2} s_i^2(n) \sum_{n=n_1}^{n_2} s_{i+m}^2(n) \cong \left[ \sum_{n=n_1}^{n_2} f_i^2(n) + \sum_{n=n_1}^{n_2} \sigma_i^2(n) \right] \cdot \tag{24}$$

$$\left[\sum_{n=n_1}^{n_2} f_{i+m}^2(n) + \sum_{n=n_1}^{n_2} \sigma_{i+m}^2(n)\right]$$

$$\cong \left[\sum_{n=n_1}^{n_2} [f_i^2(n) + \sigma^2] + \sum_{n=n_1}^{n_2} \varphi_i(n)\right]$$

$$\cdot \left[\sum_{n=n_1}^{n_2} [f_{i+m}^2(n) + \sigma^2] + \sum_{n=n_1}^{n_2} \varphi_{i+m}(n)\right]$$

where $\sum_{n=n_1}^{n_2}[f_i(n)\,\sigma_i(n)] \cong 0$ determines the uncorrelation between the signal and the noise. $\phi_i^2(n)$ can be decomposed into its zero-mean component $\varphi_i(n)$ and variance $\sigma^2$ . A larger kernel $K$ effectively reduces the effect of noise $\varphi_i(n)$ relative to $[f_{i+m}^2(n) + \sigma^2]$ by a factor of $\sqrt{K}$, leading to a statistically more robust evaluation of spatial coherence in SLSC [68].

Furthermore, FDMAS and SLSC make use of filtering differently, according to Equation 22. As previously mentioned, FDMAS attenuates the zero-mean frequencies and passes the second harmonic component in contrast to SLSC algorithm, which implements a low-pass filter. In theory, both filters should yield the same spatial coherence calculation if the kernel is large enough. Otherwise, second harmonic filter might miss the development of higher frequencies components. The kernel should be at least one period of the transducer's center frequency. Nevertheless, using the second harmonic filter can be beneficial in certain applications such as Doppler ultrasound, where the use of a higher frequency is desired [69].

Lastly, the weight function $w(m)$ attributes a score to each correlation calculation. FDMAS assigns a coherence weight of $N - m$ by summing the $N - m$ quasi-normalized signal pairs at lag $m$ without dividing by $N - m$. In contrast, SLSC uniformly assigns the $N - m$ signal coherence at lag $m$ and divide it by $N - m$. Since coherence is greater at smaller lags, short-lag coherence

contributes more than larger lags. Thus, to overcome previous limitations with FDMAS and SLC, I present the GSC equation:

$$y_{GSC}(n) = w(n)\sum_{m=1}^{M}\sum_{i=1}^{N-m} h(n) * \left[\frac{s_i(n)}{\sqrt[4]{\sum_{n=n_1}^{n_2} s_i^2(n)}}\frac{s_{i+m}(n)}{\sqrt[4]{\sum_{n=n_1}^{n_2} s_{i+m}^2(n)}}\right] \tag{25}$$

where $g(n) = \frac{s_i(n)}{\sqrt[4]{\sum_{n=n_1}^{n_2} s_i^2(n)}}$ preserves signal magnitude and $h(n)$ is a low-pass filter that extracts DC components. $w(n) = 1$ for m<M and 0 to give preference to contributions from small lags. The quasi-normalization and non-uniform weight function $w(m)$ from FDMAS and a larger kernel from SLSC gives GSC not only a generalized beamformer equation but it combines the strengths from multiple algorithms providing higher contrast and noise robustness compared to previous techniques.

### 4.4 Imaging metrics

In this section, I will define the imaging metrics used to compared DAS, FDMAS, SLSC, and GSC algorithms: contrast, signal-to-noise ratio, and generalized contrast-to-noise ratio. Equations 26, 27, and 28 define these metrics, respectively:

$$C = 20\log\frac{S_i}{S_o} \tag{26}$$

$$SNR = 20\log\frac{|S_i|}{\sqrt{\sigma_o^2}} \tag{27}$$

$$gCNR = 1 - \sum_{k=0}^{N-1} \min\{h_i(x_k), h_o(x_k)\} \tag{28}$$

where $S_i$ and $S_o$ are the mean brightness values inside and outside the imaging target, respectively. $h_i(x_k)$ and $h_o(x_k)$ are the histograms inside and outside the imaging target and $x_k$ is the bin index, and $\sigma_o^2$ is the variance outside the target. It is worth noting that although contrast and SNR are standardized imaging metrics, generalized CNR is a relatively new metric that measures target detectability score from 0 to 1, with 1 being maximum detectability. Compared to traditional CNR, gCNR provides an improved linear relationship [70], [71].

### 4.5 Reconstruction simulation

To confirm GSC's feasibility to improve contrast, SNR, and gCNR with respect to DAS, FDMAS, and SLSC I first run simulations using K-wave MATLAB toolbox [72], a software designed to solve time-domain acoustic equations in complex media such as tissue. In this case, I set a 2D grid with 512x512 points and a total grid size of 20x20mm. In FDTD, to maintain a balance between numerical model stability and computational speed, we use the Courant-Friedrichs-Lewy (CFL) parameter defined as:

$$CFL = \frac{c_o \Delta t}{\Delta x} \tag{29}$$

where $c_o$ is the speed of sound in tissue (~1500 $m/s$), $\Delta t$ is the time step, and $\Delta x$ is the grid step size. Furthermore, the ultrasound sensor parameters, shown in Table I, are chosen so that there are similar to the one that we will use in experiments (Section 4.6).

Table 1: Transducer parameters

| Parameters | Value |
|---|---|
| **Number of elements** | 128 |
| **Pitch** | 0.67 mm |

| | |
|---|---|
| **Sampling frequency** | 14.925 MHz |
| **Center frequency** | 2.5 MHz |
| **Fractional bandwidth** | 80% |

I performed four different simulations. Firstly, to determine the ultimate resolution from each beamformer, I set a point source 10mm away from the detector and reconstructed it using DAS, FDMAS, SLSC, and GSC. Figure 23 represents the PSFs from such beamformers:

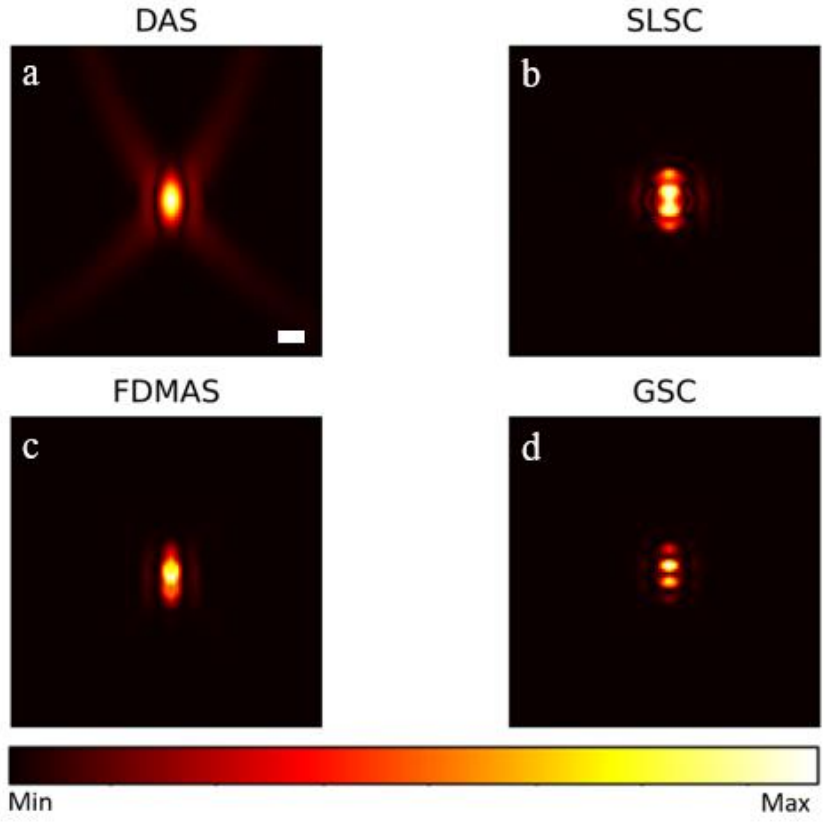


Figure 23: Noise-free PSF reconstruction from a) DAS, b), SLSC, c) FDMAS, and d) GSC. Scale bar: 1mm

Although DAS and FDMAS do not have configurable parameters, in SLSC and GSC we selected a $M$ lag of 0.7 to strike a balance between lateral resolution and other imaging metrics. Without noise, SLSC might yield unrealistic results due to the fact that uses spatial coherence as the

imaging contrast and the point source should not have any coherence difference between transducer elements. Moreover, the kernel size is set two one wavelength to balance correlation stability and axial resolution. Normalized lateral PSFs from Figure 23 are shown in Figure 24a representing the ideal system resolution with aforementioned transducer configuration and a -40dB noise amplitude. FDMAS has the lowest resolution with 152μm. GSC has 158μm, SLSC 181μm, and DAS 193 μm. These results are expected since FDMAS improves resolution by implementing a second harmonic filter to remove low frequencies and DAS does not take advantage of spatial coherence between elements. GSC shows the lowest side lobes.

Moreover, Figure 24b shows the normalized axial profile from Figure 23. GSC outputs the highest contrast (difference in low-to-high points). Although GSC can be already compared to state-of-the-art techniques in noise free environment, we will now see realistic results with added noise.

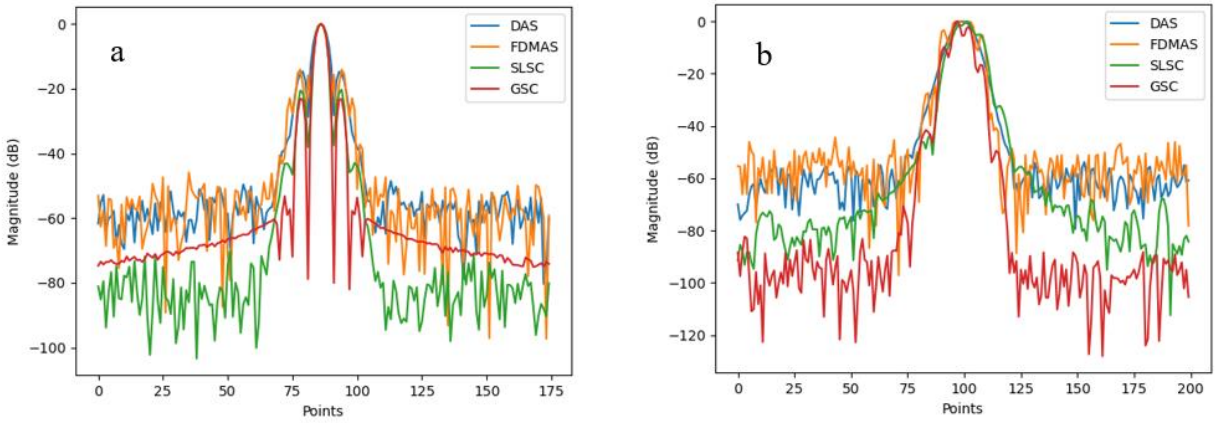


Figure 24: a) Lateral PSF b) Axial PSF

Figure 25 represents reconstructed PSF with -12 dB noise added to the sensor data. From a qualitative perspective, we can see that our algorithm, GSC is more robust to noise compared to other techniques. As expected, DAS has a low noise tolerance and the image is already corrupted. FDMAS has higher tolerance than DAS but uses a one point kernel and that makes correlation calculations unstable. SLSC and GSC have similar noise robustness. Quantitatively, I calculated

the image contrast and SNR based on Equations 26, 27, and 28 and the outlined regions in Figure 25. Results are outlined in Table 2:

Table 2: Contrast and SNR comparison for -12dB noise PSF reconstruction

| Algorithm | Contrast (dB) | SNR (dB) |
|---|---|---|
| **DAS** | 14.8 | 21.1 |
| **FDMAS** | 24.8 | 24.8 |
| **SLSC** | 40.6 | 40.6 |
| **GSC** | 41.2 | 41.8 |

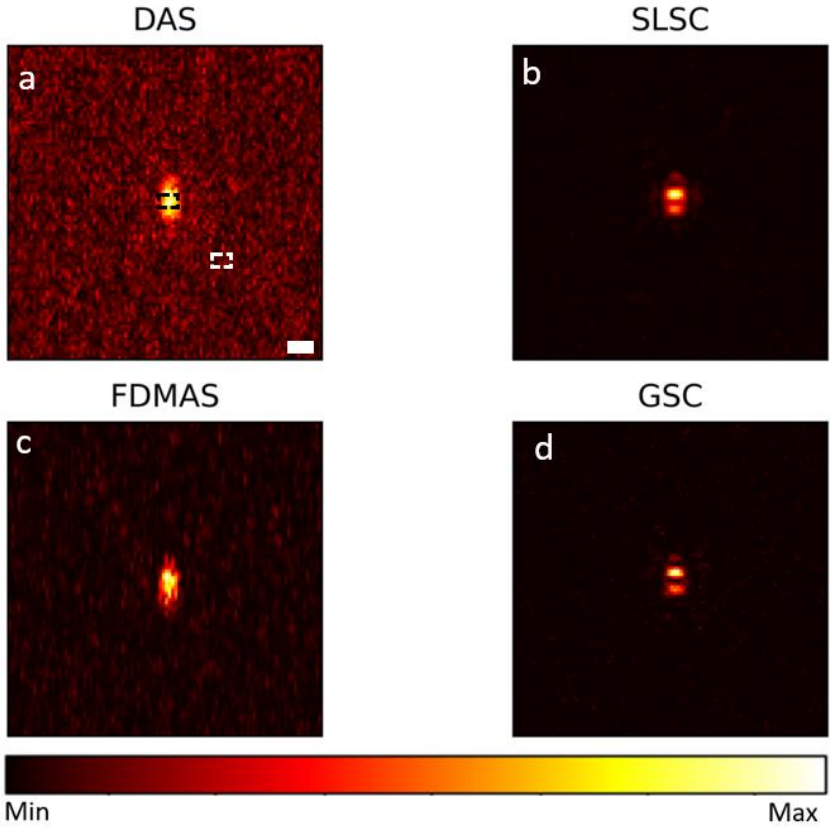


Figure 25: -12dB noise PSF reconstruction using a) DAS, b) SLSC, c) FDMAS, and d) GSC. Scale bar: 1mm

Although GSC and SLSC have similar quantitative imaging metrics, we need to recall one of SLSC's main flaws: loss of quantitative information due to its aggressive normalization. To highlight this property, I reconstructed three point sources located at different spatial locations with normalized absorption coefficients of 0.4, 0.8, and 1, this is shown in Figure 26. The lateral line profile from each reconstructed image is shown in Figure 27 compared against its ground truth. The difference between SLSC and the rest of beamformers is notable: SLSC cannot preserve relative signal magnitude. This makes now clear that although SLSC can have similar noise robustness as GSC it cannot be applied to quantitative imaging techniques.

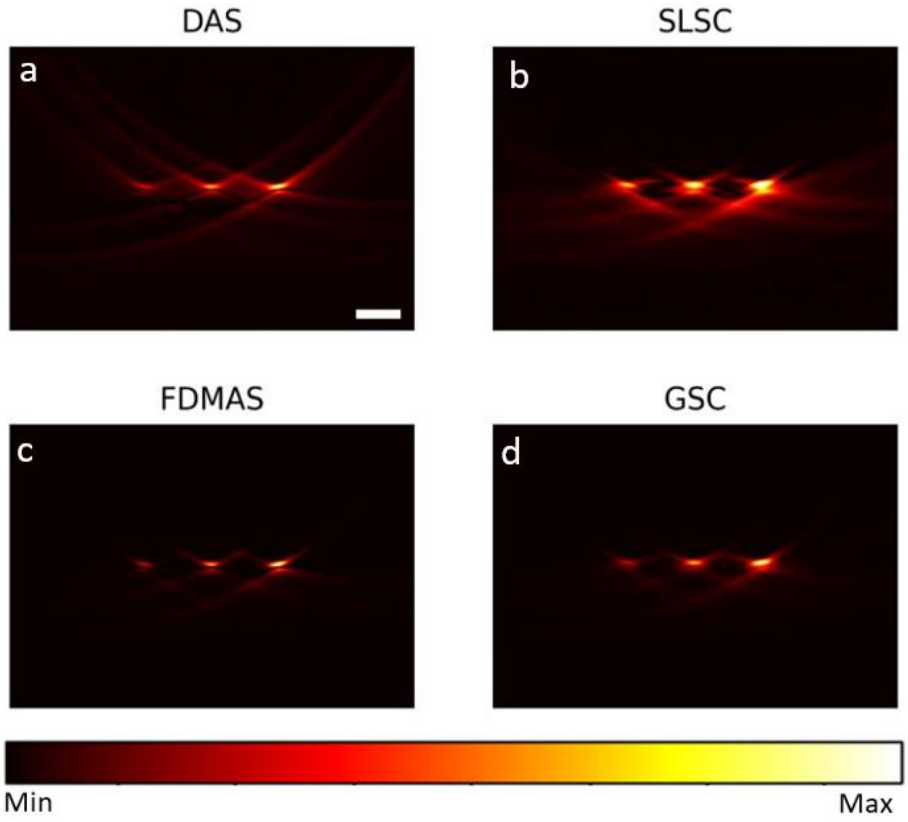


Figure 26: Three-point reconstruction for signal magnitude preservation experiment using a) DAS, b) SLSC, c) FDMAS, and d) GSC. Scale bar: 1mm

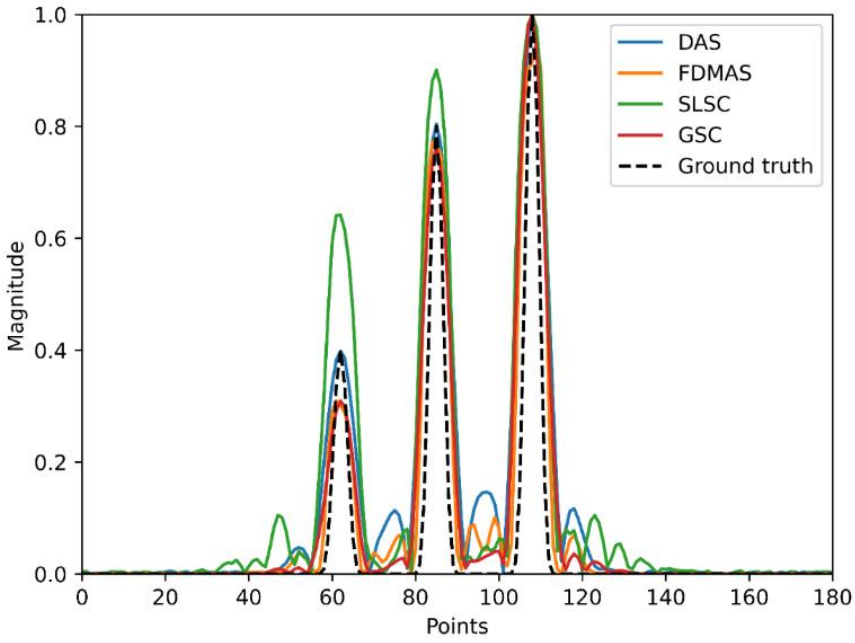


Figure 27: Lateral weight profile of reconstructed points in Fig.26

Moreover, one the main doubts when reconstructing images is how to adjust the M lag parameter in GSC. In Figure 28, we performed a study where we reconstruct the same point source from the simulation in Figure 25 using different lags. The qualitative results are as expected: using a small aperture (10-30%) yield results with low resolution since the difference with spatial coherence is relatively large. However, as we increase the synthetic aperture (50-90%) we obtain better resolution. In a low noise level scenario, larger lags will yield better imaging quality metrics until the SNR starts decreasing. This is quantitatively determined in Table 3. Imaging quality metrics reach a peak at 60% aperture and start lowering down due to trade-off between resolution and SNR.

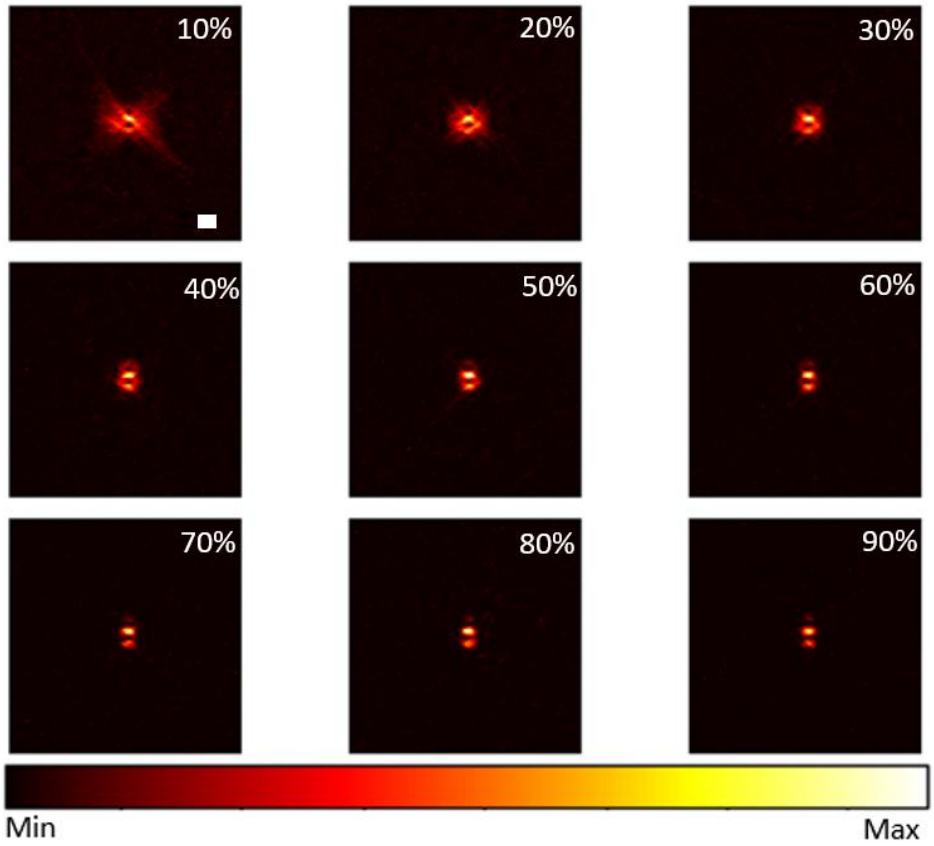


Figure 28: GSC's point source reconstruction with different lags (10-90%). Scale bar: 1mm

Table 3: GSC's imaging metrics at different lags

| Lag (%) | C (dB) | SNR (dB) | gCNR (dB) |
|---|---|---|---|
| 10 | 28.94 | 34.96 | 0.8 |
| 20 | 30.06 | 35.02 | 0.8 |
| 30 | 32.76 | 38.79 | 0.9 |
| 40 | 33.44 | 39.46 | 0.9 |
| 50 | 40.1 | 40.1 | 0.9 |
| 60 | 40.74 | 40.74 | 0.9 |
| 70 | 40.66 | 40.66 | 0.9 |
| 80 | 40.50 | 40.48 | 0.9 |
| 90 | 37.08 | 39.47 | 0.9 |

Now that we have a general idea of how GSC outperforms DAS, FDMAS, and SLSC when reconstructing a point object, let us see a more realistic object. Since one of the main applications of PACT is cardiovascular imaging we will simulate a vessel-like phantom, shown in Figure 29:

Figure 29: Ground truth vessel-like phantom. Scale bar: 1mm

Figure 30 shows the reconstruction results from vessel-like phantom from DAS, SLSC, FDMAS and GSC at different noise levels determined by σ, the noise standard deviation. Noise levels from a) to e) are -20dB, -12dB, -10dB, -5dB, and -1dB, respectively. In general, we can see that the phantom cannot be well reconstructed, this is due to the well-known limited view problem: since the transducer's geometry is linear, structures that are oriented orthogonal with respect to the transducer will not be well reconstructed. We would need to change the transducer orientation to see them. Nevertheless, we can see that the last column (GSC) gives overall better result in qualitative terms at all noise levels. Starting at -20dB noise level, all techniques can yield an accurate reconstruction. All techniques behave similarly in terms of imaging metrics as with PSF reconstruction in Figure 25 due to noise robustness and filtering steps.

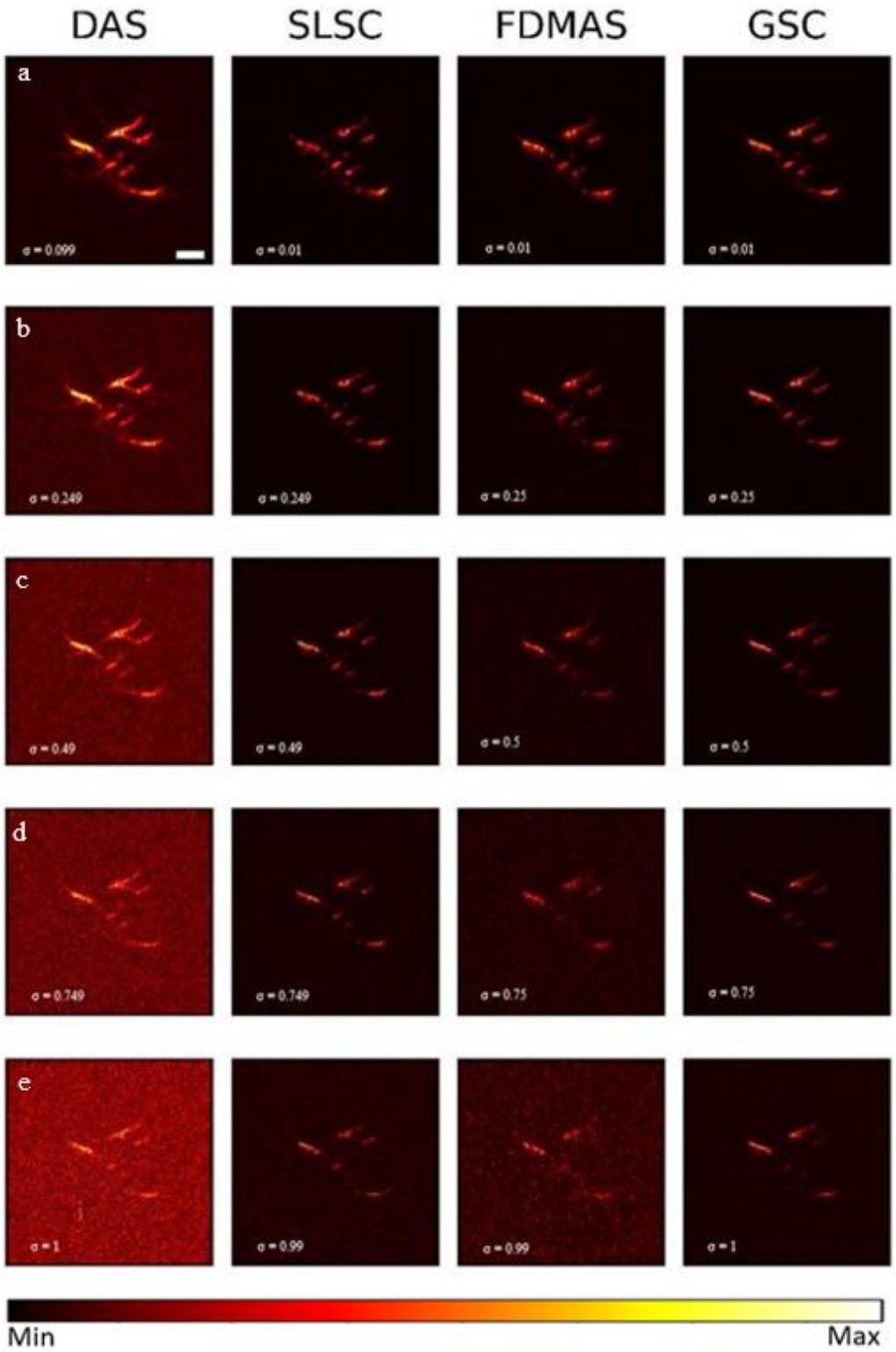


Figure 30: Vessel-like phantom reconstruction at five different noise levels (dB): a) -20; b) -12; c) -10; d) -5; e) -2. σ indicates noise standard deviation for each reconstruction. Scale bar: 1mm

As noise increases in rows B and C from Figure 30, we can see that DAS quickly starts to lose its imaging quality and the vessel is surrounded by noise. Moreover, due to FDMAS' use of only one point kernel, we can see it is not able to handle -10dB noise level and noise slowly starts to dominate the image. In row D, which corresponds to -5dB noise level, DAS and FDMAS can barely reconstruct the vessel. Lastly, at row E, with -2dB noise level, DAS and FDMAS cannot reconstruct the vessel with fidelity while SLSC and GSC can still differentiate between its features and noise. It is worth noting that in SLSC, vessel might be brighter than GSC in some regions due to signal magnitude loss which was previously demonstrated in Figure 27. Overall, we can see that GSC outperforms qualitatively all other techniques in PACT and ultrasound realistic scenarios, meaning, with a medium to high level of noise.

On the other hand, Figure 31 shows quantitative results from Figure 30. We extracted information from inside and outside the target shown in the highlighted area for every beamformer at every noise level. In terms of contrast (Figure 31a), it is clear that DAS and FDMAS exhibit a higher negative gradient as noise level (dB) increases due to poor noise robustness, this is also applicable to other metrics such as SNR (Figure 31b) and gCNR (Figure 31c).

At -10dB, GSC differs 4dB, 14dB, and 26dB from SLSC, FDMAS, and DAS, respectively, and consistently achieves a better contrast. Note that FDMAS starts obtaining better imaging metrics than SLSC but poorly handles higher noise levels. In addition, in SNR terms, GSC also shows the highest values consistently while FDMAS and DAS still show less noise robustness.

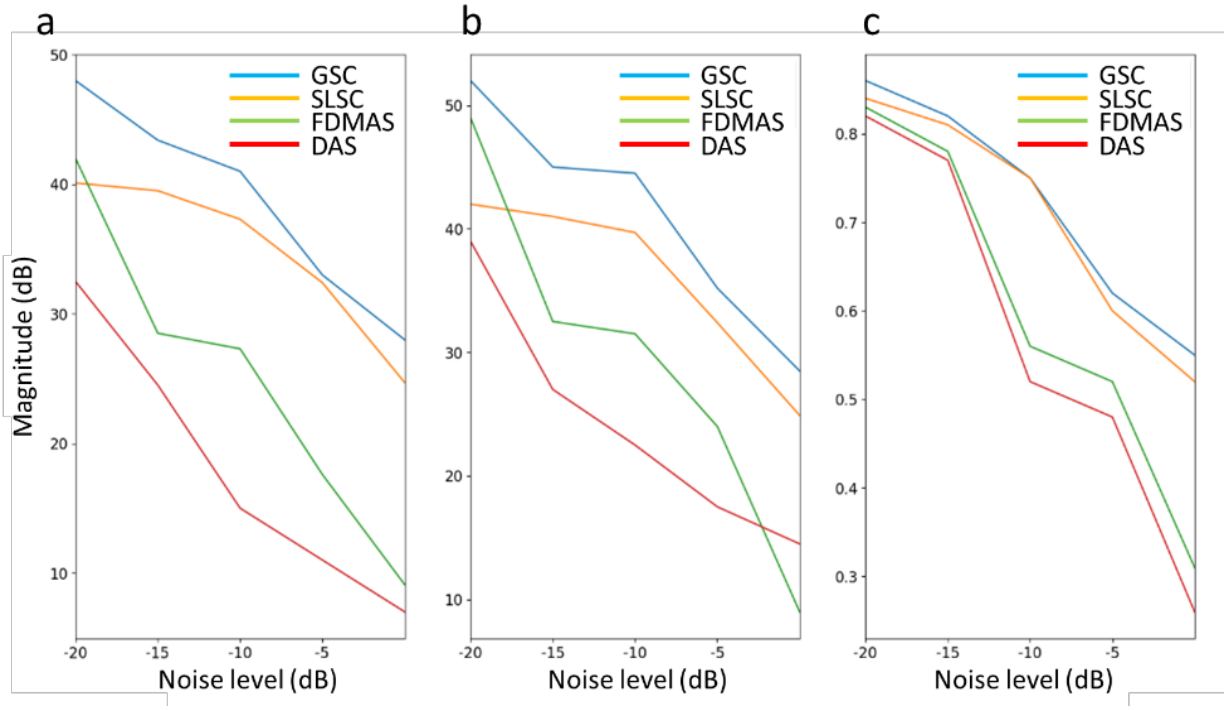


Figure 31: Imaging metrics a) Contrast; b) SNR; c) CNR for different noise levels in Fig. 30

At -20dB and -15dB, GSC outperforms SLSC, FDMAS, and DAS by 9dB, 3dB, and 17dB, respectively. At the highest noise level (-2dB), the difference become 5dB, 22dB, and 15dB, respectively. Lastly, in Figure 31c we can see that all beamformers output between 0.8 and 0.8 gCNR (feature detectability) with the lowest noise level. As noise increases, two groups can be clearly differentiated, the short-lag techniques, with a selected lag of 30% to balance resolution and noise robustness, and DAS and FDMAS. The gCNR shows a similar dependence on noise as with contrast and SNR. All beamforming techniques show between 0.8 and 0.9 detectability with a -20 dB noise level. At the second noise. At -5 dB and -2 dB, GSC outperformes others with highest lesion detectability values, 0.6 and 0.55, respectively, followed by SLSC with 0.2 difference. At the highest noise level, DAS and FDMAS cannot reconstruct the vessel with high fidelity, and their gCNR are 0.27 and 0.32, respectively. It is also worth adding that GSC outperforms SLSC using the same lag. Figure 32 justifies why a 30% lag was selected for vessel phantom reconstruction and shows how GSC and SLSC compare. GSC improves SLSC

reconstruction in every metric at each noise level. In realistic simulations, the aperture needs to be reduced compared to the results with PSF with no noise added and PSF with various noise levels due to the sparsity of the object, which leads to a good reconstruction even when the noise level is high. In this case, the vessel has high frequency features which can be easily buried in noise so that is why a shorter lag provides better reconstruction results:

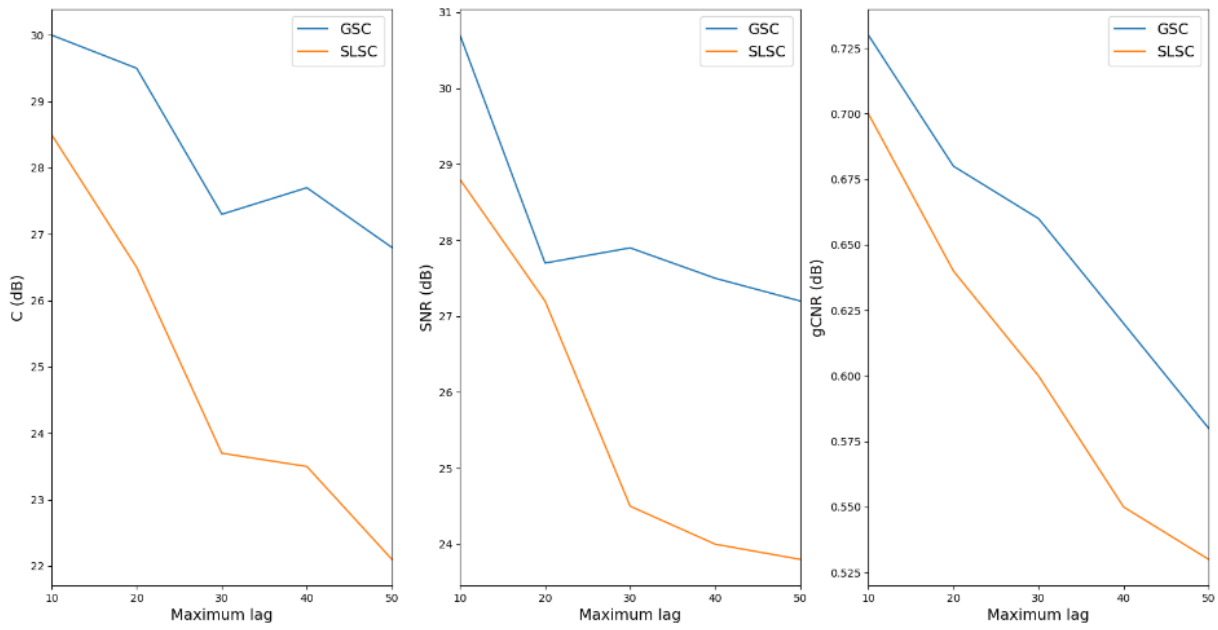


Figure 32: Contrast and SNR in SLSC and GSC with different maximum lag selection in vessel phantom

In conclusions, I performed four simulations that show that GSC outperforms four considered beamformers: classical DAS and spatial coherence algorithms FDMAS and SLSC. First, calculating the PSF in the absence of noise. Secondly, simulated noise effects. Third, evaluated beamformers in preserving signal magnitude and lastly, tested all beamformers with a realistic phantom at different noise levels.

### 4.6 Experimental setup

In order to experimentally demonstrate GSC's capabilities to produce state-of-the-art imaging quality reconstruction results, we built a PACT setup for hand palm imaging shown in Figure 33:

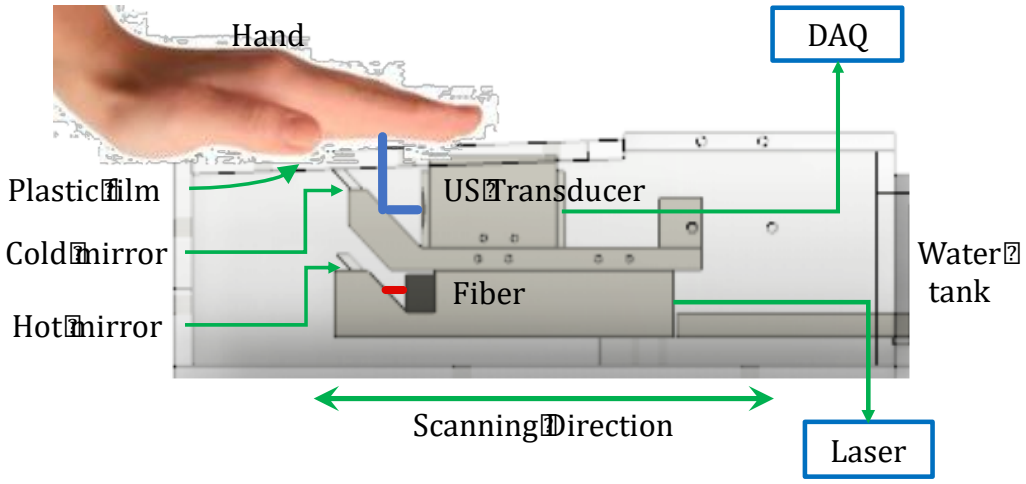


Figure 33: schematic drawing of human palm PACT imaging setup

Overall, the setup is a water tank with suitable acoustic coupling of ultrasound signals in an opening made of Fluorinated Ethylene Propylene (FEP) plastic film used as the imaging window. To ensure the correct functioning of the system, pulse-echo measurements were used before imaging to make sure there are no reflections or high attenuation through the FEP film (50μm thick). The excitation light source is a nanosecond pulsed ND:YAG laser with 1064nm wavelength output and pulse repetition frequencies of 10Hz (Continuum, SL III). The light source is delivered to the sample through a fiber. A cold mirror reflects 90% of the light and a hot mirror transmits 97% to the sample. It has also been tested that the light transmission trough the FEP film is 97%. The light delivery setup ensures maximum transmitted light at the sample plane. Furthermore, the cold mirror reflects incoming ultrasound waves to the transducer. In this way, we make sure that both light delivery and acoustic detection are coplanar. A 20 cm stroke translation stage

(McMASTER-Carr) mounted on an optical breadboard was used to ensure linear scanning. Moreover, the ultrasound transducer array (Imasonics, Inc) is custom-made with 128 linear units and curved features to achieve acoustic focusing without using an acoustic lens. Element pitch and central operating frequency are 0.67mm, and 2.25MHz, respectively.

All human procedures were performed in compliance with the University at Buffalo IRB protocol. All volunteers were enrolled after consent documents were signed. During imaging, the palm was placed on the plastic film (imaging window) with ultrasound gel as the coupling agent (Parker Laboratories, Inc.). The transducer-fiber bundle set (scan head) fixed in the 3D printed holder was immersed into the water tank. Energy irradiated on the palm was far below the ANSI safety limit of $100\mathrm{mJ/cm^2}$ for 1064 nm wavelength, measured as $21\mathrm{mJ/cm^2}$ [73]. For imaging, the palm was scanned linearly with a step size of 0.1mm per laser pulse. The total imaging window size was 20cm × 10cm [74]–[76].

Figure 34 shows reconstruction results from palm imaging. We reconstructed each slice separately using the same four beamforming algorithms discussed in the simulation section: DAS, FDMAS, SLSC, and GSC. Then, we took a maximum amplitude projection (MAP) along the depth direction to show a final 2D image. In Figure 34a, we can see DAS reconstruction, the main structures of the hand vessels can be seen but they are surrounded by noise. Also, in the bottom right, we can see a feature showing relatively low contrast. In Figure 34b SLSC's image reconstruction with a lag of 30% as with vessel phantom high level noise reconstruction is surprisingly poor and its artifacts may be due to the slicing process during acquisition.

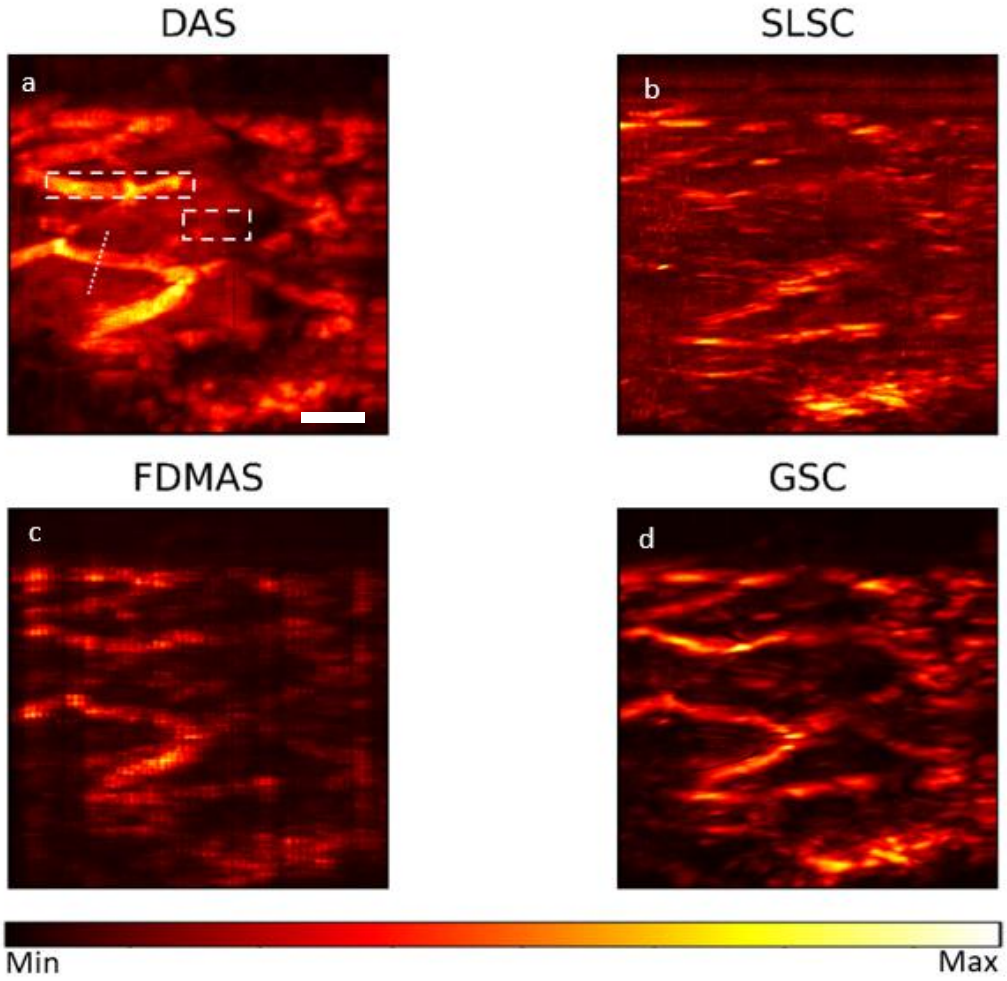


Figure 34: Human palm PACT imaging reconstruction using a) DAS; b) SLSC; c) FDMAS; d) GSC. Scale bar: 2mm

Furthermore, FDMAS shows the highest resolution, that was measure by taking a line profile of an arbitrary vessel (see outlined region in Figure 34a). FDMAS measured 1.7mm while others (DAS and GSC) showed 2.0mm. We did not measure resolution in SLSC due to slicing artifacts. However, FDMAS shows a poor contrast to noise ratio compared to GSC and many feature cannot be seen unless the signal is considerably higher compared to noise.

Quantitative imaging metrics for reconstructed images from Figure 34 are shown in Table 4. GSC outperforms FDMAS, DAS, and SLSC by 8 dB, 10 dB, and 13 dB respectively. GSC also has the highest gCNR followed by FDMAS with 0.05 difference, DAS, and SLSC. SLSC's SNR and

gCNR is the lowest due to slicing artifacts. GSC ‘s SNR is more than 3 dB higher than all other beamformers. Overall, human hand palm imaging experimental results show that GSC outperforms DAS, FDMAS, and SLSC in all imaging metrics, as predicted by our previous simulations.

Table 4: Imaging metrics from human palm PACT imaging

| | **Contrast (dB)** | **SNR (dB)** | **gCNR** |
|---|---|---|---|
| **DAS** | 8.94 | 25.2 | 0.73 |
| **SLSC** | 6.67 | 17.3 | 0.54 |
| **FDMAS** | 11.29 | 20.9 | 0.81 |
| **GSC** | 19.63 | 28.0 | 0.86 |

## 4. Discussion and conclusions

First, it is worth noting that in GSC and similar to SLSC, choosing the lag is empirical since it is hard to calculate how it will exactly affect the lateral resolution and contrast. In objects surrounded by relatively low levels of noise, we can use a shorter lag to improve lateral resolution. However, in deeper tissue regions, where the laser fluence is low and thus there is a small photoacoustic signal amplitude, there is no reason for using short lag for two reasons: higher frequencies will be attenuated faster through tissue due to exponential relationship between absorption and frequency, and secondly because it will affect the reconstructed SNR. Thus, it is convenient to use a larger lag. In conclusion, using a larger $M$ lag will produce a better resolution since the effective aperture is increased while using relatively small lag values improves imaging contrast. Moreover, the second parameter to optimize is the kernel, the number of time points chosen for each correlation calculation. The rule of thumb is to select a value that balances axial resolution and correlation

stability; an acoustic wavelength is typically enough. Lastly, the filter in GSC beamforming equation should be selected depending on the application. For comparison, in FDMAS, the filter is used due to the doubled signal frequency produced by multiplying signals with similar content. Its goal is to attenuate lower frequencies and use half wavelength content which improves the resolution. In GSC, we can effectively achieve nearly the same resolution due to noise robustness. In addition, we could use a bandpass filter if we want to improve the resolution in critical applications. For instance, in elasticity imaging, the low-frequencies highly decrease lateral resolution.

GSC is not only a combination and generalization formula for FDMAS and SLSC. It improves its strengths with no known weaknesses. As with FDMAS, GSC preserves relative signal magnitude. As with SLSC, it has larger noise robustness due to a larger kernel used to evaluate coherence calculations. GSC further improves contrast, SNR, and gCNR with respect to classical and similar beamforming reconstruction techniques. GSC's lateral resolution improvement depends on its parameters selection: filter, lag, and kernel.

Although there are many other techniques that have modified and combined versions of FDMAS and SLSC, GSC takes the best from both technique into a single equation. SLSC has been previously modified with M-weighted and locally non-uniform weighted versions but still do not preserve relative signal magnitude for quantitative imaging applications [39], [55]. Similarly, there have also been improved versions of traditional FDMAS with a coherence factor that has enhanced resolution and SNR. However, CNR has still been a problem with a one point kernel when there is a relatively high noise level. In conclusion, GSC is a versatile and generalized spatial coherence algorithm that can span many more applications.

In terms computational cost terms, GSC has a similar cost compared to SLSC and FDMAS. DAS still remains more simple due to less calculations. Particularly, its cost compared to FDMAS and SLSC depends on the kernel selection. If we were to use kernel equal to one, it would be the same. In order to achieve real-time imaging in GSC, FDMAS, or SLSC, we can use parallel beamforming using a graphical processing unit (GPU) [77]. For a 512x512 reconstruction grid, our achieved frame rate was 10 Hz using Nvidia RTX2080Ti GPU.

To conclude, we generalized FDMAS and SLSC beamformers into a single equation named generalized spatial coherence (GSC) which goes beyond combining the strengths from both beamformers: it has state-of-the-art noise robustness and preserves relative signal strength.

**4. Future work and applications**

We foresee that GSC will have many applications in biomedical imaging. This is because it is a general technique that could be implemented in any beamforming reconstruction setup. Particularly for PACT, GSC could be used in laparoscopic and hysterectomy procedures to visualize and differentiate ureter and uterine arteries avoiding injuries during surgical procedure [78]–[81]. Furthermore, PACT's focus on cancer imaging applications has immensely grown in the past years [82]. GSC could potentially help locate tumors in deeper regions of any tissue where light delivery is non optimal and hence the absorber molecules are poor and surrounded by noise in the final image. In future work, we would like to test this technique in a more focused clinical application to help develop the next-generation photoacoustic imaging systems or in elastography for ultrasound imaging [83].

# Chapter 5 Light field tomographic microscopy

In previous chapters, I have focused on the problem of imaging through deep tissue beyond the optical diffusion limit. Chapter 5 is different since it focuses on imaging tissue at high speeds. In many biological imaging problems as shown in Chapter 1, it is not only important to image at a required spatial resolution and contrast but also have enough temporal resolution. For instance, neuronal dynamics can occur at thousands of frames per second and if frame rate is not high enough, the scene will contain motion artifacts and blur. Common widefield microscopy can enhance its acquisition speed by either reducing the sensor's dynamic range and region of interest but still lack high field-of-view, three-dimensional fast imaging and the speed acquisition problem obviously relies on the sensor.

In fluorescence tissue imaging, capturing images at thousands of frames per second has already been done [84]–[91]. However these techniques also lack full field of view and three-dimensional imaging. In this Chapter, I focus on imaging fast and three-dimensional dynamics. How can we get three-dimensional scenes at a desired frame rate? To solve this problem, we will first visit the plenoptic function.

## 5.1 The plenoptic function

In 1991, Adelson and Berger [4] revisited a concept first introduced by Gabriel Lippman in 1908 that mathematically explains what our eyes capture and depict from our surroundings: the plenoptic function. Plenoptic, from Latin, *plenus* and *optics*, can be etymologically translated as 'complete' 'optic'. Such function contains all possible light fields parametrizations represented in Figure 35:

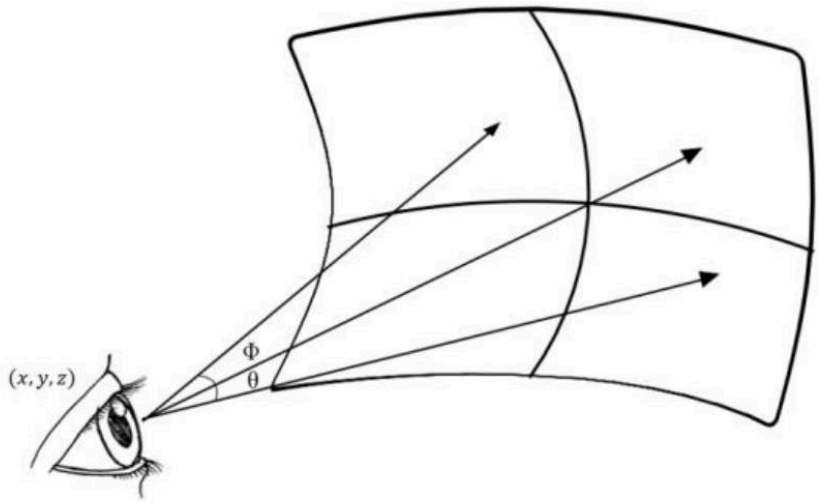


Figure 35: Representing the plenoptic function

In theory, we can represent any scene, at any point, if we know where the ray of light is located in a three-dimensional space, that is : $x$, $y$, $z$, its angular direction $\theta$ and $\phi$, wavelength $\lambda$ at time t. However, it is hopeless expecting to accurately determine even a small part of such function since in reality, we use two-dimensional charge-coupled devices (CCD) and complementary metal oxide cameras (CMOS), one-dimensional line scan detectors, and zero-dimensional single pixel sensors to capture the world. This means that if we wanted to capture the plenoptic function we would have to compress seven dimensions into a two-dimensional detector, at best. To do so, we cannot rely on classical Nyquist sampling theorem, which states that we need at least twice the sampling rate two accurately represent a scene; the data cube would be huge creating problems with data acquisition, processing, and rendering. A more efficient option is to make use of compressed sensing (CS), a technique that can recover high fidelity, high dimensional information, from a lower dimensional measurement. In mathematical terms, this means solving an undetermined linear system given that the signal is sparse and incoherent in some of the given dimensions.

### 5.2 Light field imaging

Light field imaging can be considered as a re-interpretation of conventional two-dimensional photography. Let us first consider the light rays entering the aperture plane of a camera lens and the sensor plane shown in Figure 36. This is a two-dimensional representation of a light field. Each possible light ray shown has its corresponding location in $x$, $u$ coordinates where the former represents the spatial location of the image at the sensor plane and the later parametrizes the angular component of the rays at the camera [92]–[94].

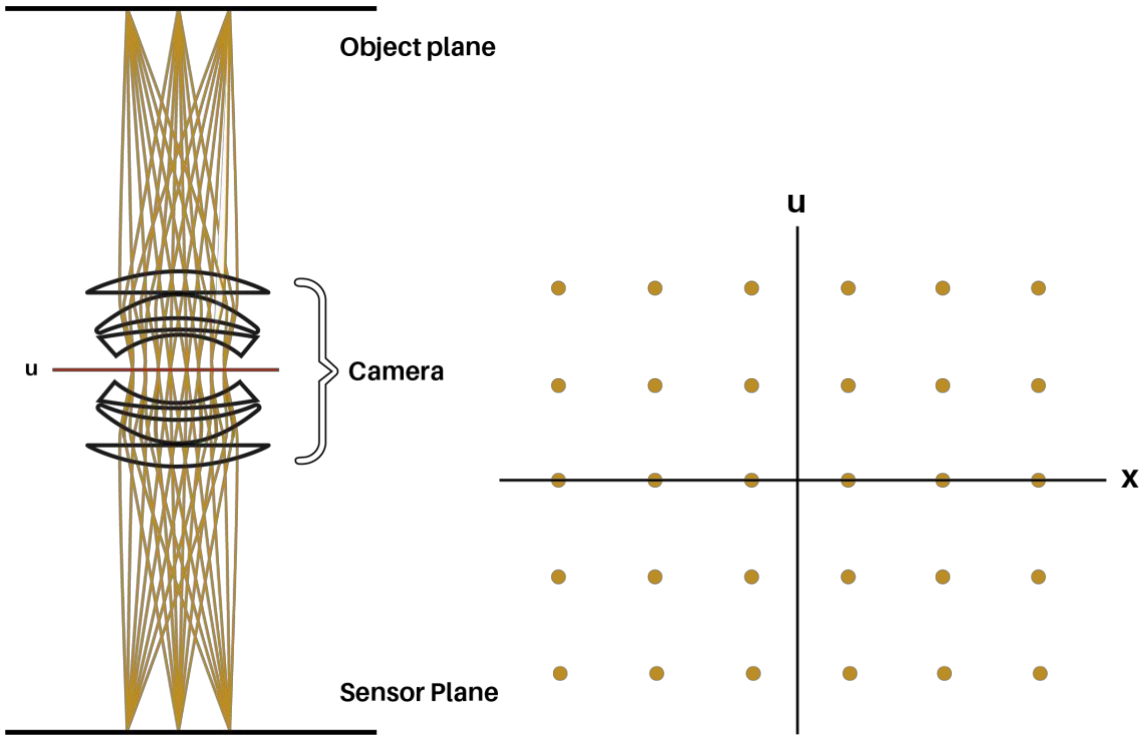


Figure 36: Light field parametrization

Let us take a closer look at ray space diagram. The main reason why conventional photography cannot extract three-dimensional information is because all angular rays in $u$ are integrated for each spatial sensor position. Thus, if we want to capture light from different angular components and see through occlusions we need to preserve the $u$ component. Light field photography and

microscopy uses a microlens array at some plane to divide the aperture and image the same object from multiple perspectives with a single snapshot. In other words, the angular component $u$ is preserved for each sub aperture. Figure 37 shows how a representation of a light field image.

In field imaging, the spatial resolution will be worse than classic photography due to the aperture division. However, we can computationally refocus the image and extend the camera's depth of field since we capture the scenes from multiple angular perspectives.

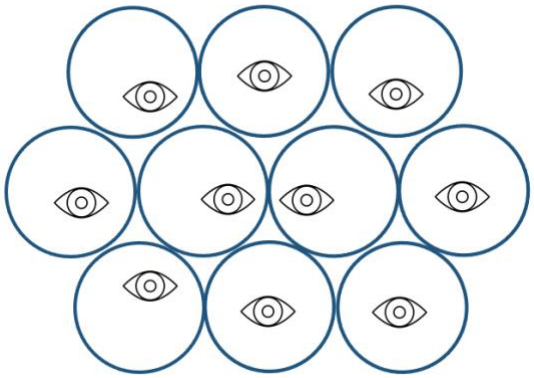

Figure 37: General representation of a light field raw image

For biomedical applications, light field microscopy was first introduced to see through occlusions in semitransparent samples [95]. Its applicability has been hugely extended to brain imaging; since neurologists are interested in capturing neuronal activity in 3D [96]–[99]. However, one of the main drawbacks in conventional light field imaging is its frame rate, limited to a few hundred frames per second which is one order of magnitude less than what is required to capture neuronal action potentials. This is because to accurately reconstruct the scene from different perspectives, the back aperture of the objective lens must be relatively large and hence the CCD or CMOS sensor must be too. This can also be extrapolated from the raw light field image in Figure 37: there are only tiny differences with respect to each images that depend on the viewing position. Thus, light

field imaging through spherical micro lenses is a fairly inefficient technique. As the imaging speed bottleneck in light field imaging is the detector size, we can introduce the frame rate equation:

$$Frame\ rate = \frac{1}{Frame\ acquistion\ time + Frame\ readout\ time} \tag{30}$$

Let us consider that the acquisition time is low in high-speed applications so that the only tunable parameter is the frame readout time, which changes with sensor technology. A typical CCD camera uses global shutter where all pixels are exposed at the same time. The advantage is that a single image is taken relatively fast and that may beneficiate when imaging a fast moving object within a single frame but the drawback is that there is a single analog-to-digital (ADC) converter so the time between frames is relatively low. On the other hand, conventional CMOS cameras have a rolling shutter in which different rows of the sensor are exposed sequentially. Depending on the number of pixels, each row might take up to 10μs to read out. Such exposure mode might produce motion artifacts known as rolling-shutter effect in which fast objects are detected in both upper and lower exposed rows. Obviously, in CMOS cameras, the readout time is proportional to the number of extracted rows. If we were to increase the frame rate in conventional photography with a CMOS sensor, we could either reduce the dynamic range such that the number of pixels per second is lower or reduce the region of interest (ROI). In fluorescent imaging, which is our main application, reducing the dynamic range is usually not possible since the number of photons emitted by tissue is relatively low and the signal will be buried inside camera noise. The latter option is available if the field of view is small but this still limits many applications.

### 5.3 Light field tomographic microscopy principle

From previous sections we can conclude that it is nontrivial to acquire high resolution, high dynamic range, and large field of view images at high speeds. In general, there is lack of tools that hamper single-shot acquisition of large two-dimensional time resolved data preventing many applications in biology, chemistry, and physics. Even more difficult is to extend high speed imaging to three-dimensional scenes that might be able to see around occlusions or non-line-of-sight imaging applications. In order to overcome such limitations, I present light field tomographic (LIFT) microscopy. In a nutshell, LIFT is a technique that compresses three-dimensional scenes into a one-dimensional line detector [100].

Let us see how to compress the data. First, in order to compress a three-dimensional scene into a two-dimensional detector we can use the same exact concept as light field: locate multiple lenses at multiple spatial locations within the aperture plane and take advantage of the disparity between them. This is show in Figure 38. Each lens will form its image with a different object perspective.

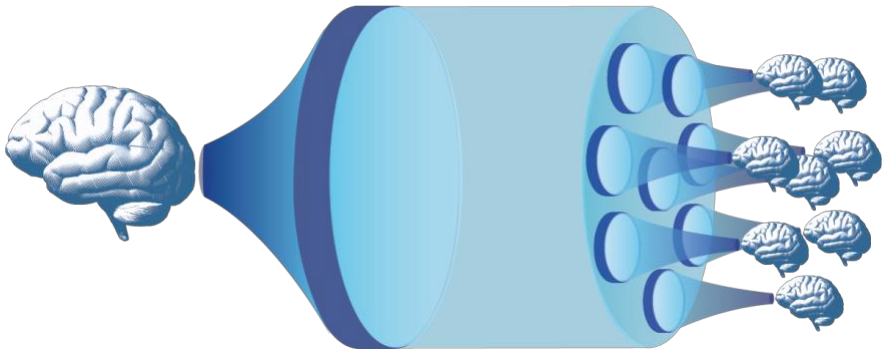

Figure 38: Aperture division light field concept

LIFT's contribution is to further compress the conventional light field image into a one-dimensional detector. To-do so, the key step is to substitute the spherical microlens array with a

cylindrical one and rotate each lens by a known angle. This process is explained in Figure 39, LIFT's image formation process. In Figure 39a, we use a two-plane parametrization for light field analysis in which the spatial axis $x$ is the sensor plane, and $u$ is the lenslet array plane which provides angular information.

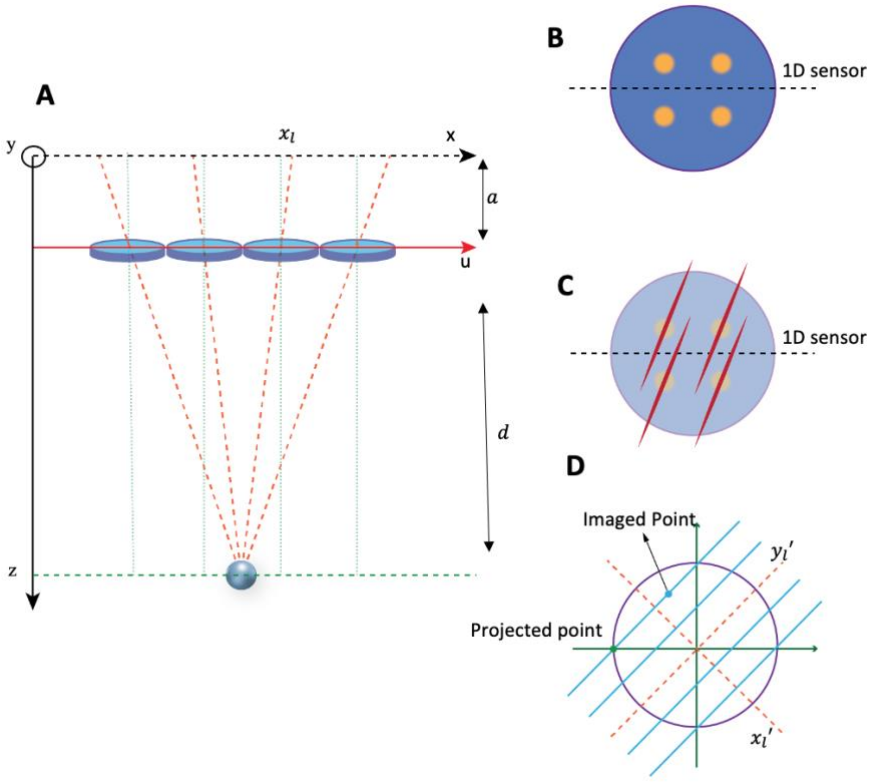


Figure 39: LIFT imaging principle a) LIFT parameterization; b) Imaging through spherical lenses; c) Imaging through cylindrical lenses; d) Projection view of the object

Furthermore, each lenslet has its own local coordinate plane $x_l$ whose origin is located where a point source located at infinity is imaged by each sub aperture. In this case, only four lenslets are shown for simplicity. This diagram is representing the parametrization of the $x$ and $u$ planes depending on where the object and the microlens array are located, same parameterization as with Figure 36. In LIFT, the classical imaging process is the same except for the cylindrical lens'

invariant optical axis direction. If a point source is located at position $x_o, y_o, d$, the subimage of each local coordinate will be located at:

$$\begin{cases} x_l = \dfrac{a}{d}(u - x_0) \\ y_l = -\dfrac{a}{d} y_0 \end{cases} \tag{31}$$

where $a$ is the distance from the lenslet array to the sensor. Figure 39b, shows such pin-hole image formation model. As it can be inferred, if we use conventional spherical microlens array, the point images of each lenslet would not be detected by a line sensor. However, if we use a cylindrical lens oriented along arbitrary rotation angle, the point spread function (PSF) will be converted into a line spread function. This is because the cylindrical lens does not have optical power along one axis (invariant optical axis). In this case, as shown in the PSF convolution in Figure 39c, part of the image will hit the sensor and that is how we can compress a two-dimensional scene into a one-dimensional line detector. The line-shaped PSF disperses each point in the image space onto a pixel on line sensor. The line length is given by the image magnification factor and the lenslet size:

$$l = \left(1 + \frac{1}{m}\right) q \tag{32}$$

where $m$ is $d/a$ and $q$ is the lenslet diameter. In other words, the image formation process is a parallel beam projection of the image that is obtained along the invariant optical axis direction. This is a key concept which means that optical imaging is reformulated as a computed tomography problem: we can relate the one-dimensional projection with a two-dimensional object via the Fourier slice theorem, we will delve into this concept in the next chapter. Overall we can recover a two-dimensional scene from the fact that we receive its one-dimensional projections and further get the three-dimensional scene if we consider that each projections has its own unique perspective of the object (Figure 39d).

Let us now focus on the last step of the image formation process: resampled projection. For now, we know that a point like object will be transformed into a line spread function rotated along an arbitrary angle dictated by the cylindrical lenslet's invariant optical axis. Generally, the line sensor is not perpendicular to such line and to relate the unknown object to such data, via the Fourier slice theorem (Section 5.40), we need to make it perpendicular. This can be done by computationally resampling. Let us denote θ as the angle between the invariant optical axis and the line sensor, the projection angle. The new virtual sensor local coordinates $x'$and $y'$perpendicular to the projection are given by:

$$\begin{bmatrix} x' \\ y' \end{bmatrix} = R_\theta \begin{bmatrix} x \\ y \end{bmatrix} \tag{33}$$

where $R_\theta$ is a rotation matrix expressed as:

$$R_\theta = \begin{bmatrix} cos\theta & -sin\theta \\ sin\theta & cos\theta \end{bmatrix}$$

by combining Equations 32 and 33, the new image local coordinates are:

$$\begin{cases} x_l' = \dfrac{1}{m}(u - x_0)cos\theta - \dfrac{1}{\mathrm{m}} y_o sin\theta \\ y_l' = \dfrac{1}{m} y_o sin\theta + \dfrac{1}{\mathrm{m}} y_o cos\theta \end{cases} \tag{34}$$

Considering that the sensor is one-dimensional, $y_l' = 0$. We can also rewrite $x_l'$ as:

$$x_l' = \frac{cos\theta}{m}(u - x_0 - y_0 tan\theta) \tag{35}$$

Equation 35 is LIFT's imaging equation where cosθ is the resampling factor, $u$ describes the light field component that enables depth retrieval and refocusing capabilities, and the last two terms explain the projection process.

### 5.4 Fourier slice theorem

The Fourier slice theorem is illustrated in Figure 40. Let us assume that we want to image an object $f(x,y)$ which has some Fourier transform $F(k)$. In LIFT, the object $f(x,y)$ is unknown but we have access to a number of projections $p(x)$ along arbitrary angles. The Fourier slice theorem states that a one-dimensional Fourier transform at an angle θ is the same as a line to the origin with angle θ of the two-dimensional Fourier transform representation of the entire object. Obviously, if we take multiple projections we can fill the entire Fourier space to later reconstruct the object in the spatial domain through a two-dimensional inverse Fourier transform.

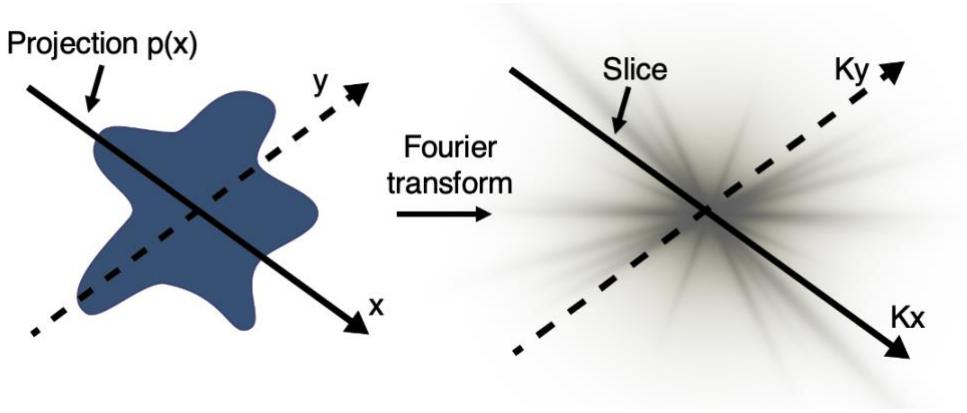


Figure 40: Fourier slice theorem representation

In practice, the number of projections is fairly limited. Specially in LIFT, limited by the number of lenses that fit in the objective's back aperture. The low frequencies are oversampled compared to the higher thus limiting the image quality depending on the sample sparsity in the spatial domain. For an accurate image reconstruction, we would need to fill the complete spatial frequency space by acquiring a sufficient number of projection data spanning from 0° to 180°. As a rule of thumb, in order to reconstruct a $N\ x\ N$ image, $N$ projections with $N$ number of pixels are needed. In LIFT, we use a 1D sensor whose pixels are limited to several thousand so this casts LIFT as a sparse computed tomography problem, we can only fit a very limited number of projections.

### 5.5 Limited view problem

Considering that the one-dimensional line sensor is fixed, we are restricted to the range of angular projections that we could extract from the object. In the worst case scenario, the optical invariant axis of the cylindrical lens would be colinear to the line sensor and occupy a relatively big number of pixels thereby limiting the number of projections to a couple. This is known as the limited view problem [101]. This makes the angle selection key, especially when the number of views is fairly limited in LIFT compared to traditional computed tomography scans. The general rule is that, since the object is unknown, a uniformly distributed number of projections will produce the best results although there are current algorithms that are able to calculate the optimal projection angles [102], [103].

There are several methods to mitigate limited view problem. The first one is to rely on deep learning methods by training a neural network that can learn the statistical distributions and patterns of the system with a limited view problem by comparing the ground truth images with the LIFT ones and correct them after [100]. This solution requires system calibration and does not really eliminate the problem. The second choice is hardware-based: introduce Dove prisms as image rotators in front of the cylindrical lens.

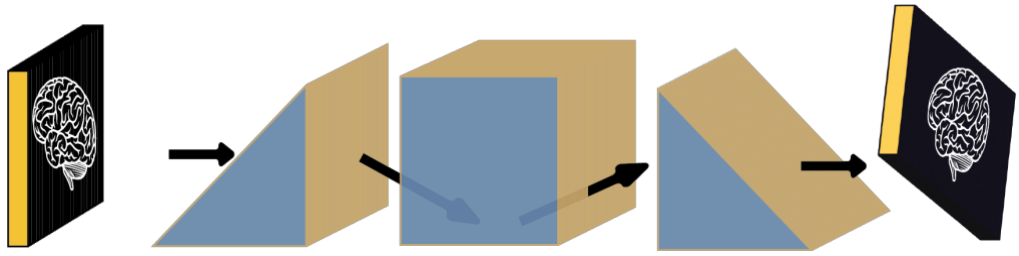

Figure 41: Dove prism as an image rotator

Figure 41 shows a Dove prism rotating the image. If the rotation angle is θ, the image is rotated by 2θ. In such way, we can partially solve the limited view problem and project the object along

any rotation angle while optimizing the number of pixels used per projection at the sensor plane by placing the cylindrical lens invariant optical axis perpendicular to the sensor. The disadvantages of the Dove prism are chromatic aberration for broadband illumination and astigmatism if light is uncollimated.

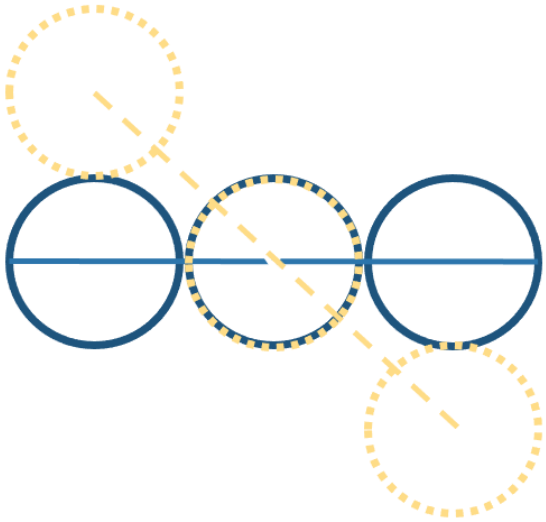

Figure 42: Line camera rotation

Another choice is rotating the camera or building a camera array as depicted in Figure 42. This requires the camera to be compact and rotate with an accurate angle. By rotating the sensor camera with 7 lenslets by 3 times will not only enrich the projections to 21 for eliminating the limited view problem but also extend the light field to 2D.

### 5.6 Limited field of view

In LIFT, the use of line sensor limits the field of view (FOV) compared to conventional light field imaging. Figure 43 represents the last point, located at the extreme spatial XY location within the FOV in LIFT. This point will be imaged as a line along certain angle according to the invariant axis and the edge of its line spread function will be detected by the sensor. Thus, the last detectable

point of the line sensor is limited to $h = lcos(\theta)/2$ and the LIFT's FOV is determined by $2h = lcos(\theta)$.

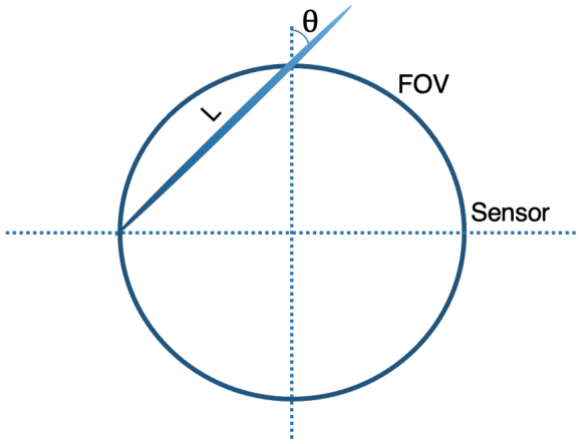


Figure 43: Limitations in LIFT's FOV

### 5.7 LIFT refocusing abilities

Analogous to conventional light field imaging, LIFT has refocusing capabilities due to the existence of subaperture lenses located at different spatial locations that produce disparity cues. Figure 44 illustrates the refocusing process:

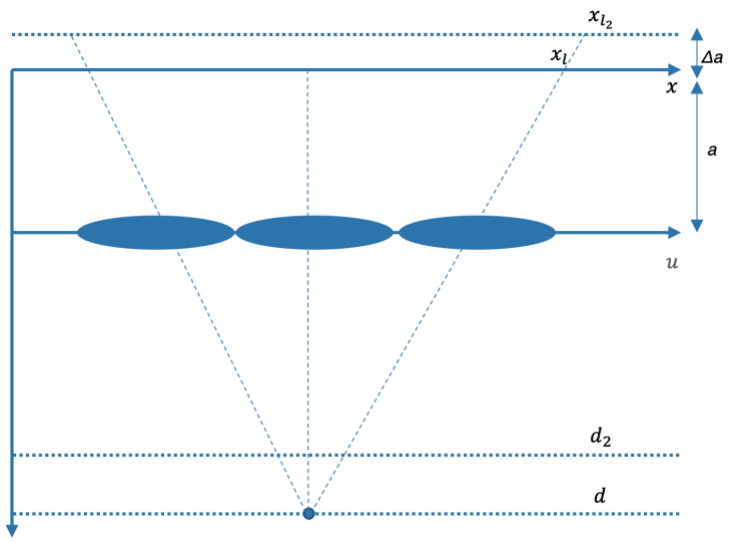


Figure 44: LIFT's refocusing capabilities

We can locate a virtual sensor plane at a distance $\Delta a$ from the original sensor and extract the image from the second depth $d_2$. Then, the new light field imaging equation is given by:

$$x_{l2} = \left(1 + \frac{\Delta a}{a}\right) x_l - \frac{\Delta a}{a} u = \left(1 + \frac{\Delta a}{a}\right) [x_l + su] \tag{35}$$

where $s = -\frac{\Delta a}{\Delta a + a}$. We can further ignore the magnification factor $\left(1 + \frac{\Delta a}{a}\right)$ since it is constant across the refocused imaged. Finally, the refocusing equation is:

$$x_{l2} = x_l + su \tag{36}$$

LIFT's refocusing formula, Equation 36 is the same one in the ray space as conventional light field cameras but along one angular axis instead of two. Shearing the acquired light field will refocus the image onto different depths. From this equation we can extract two conclusions. First, LIFT is a one-dimensional light field, there is only angular disparity along the $u$ axis, as opposed to conventional light field cameras. This is different than 1D light field cameras which produce a 1D blurring effect, shown in in Figure 45 [104]:

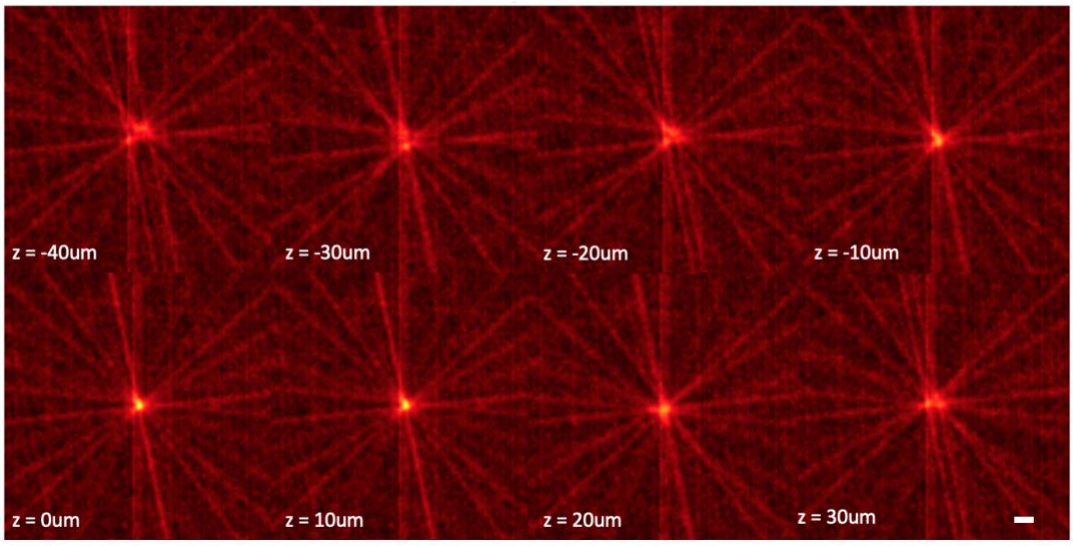


Figure 45: LIFT's blurring effect. Scale bar: 10um.

In LIFT, when the image of a point source is being focused, all projections intersect in the same lateral position forming the PSF. However, when the image is defocused and the number of projections is relatively low, different projections will have more than one intersection point and ghost images will appear. If we increase the number of projections we will see a similar blurring bokeh as with standard photography. This process also happens with conventional light field cameras with low angular resolution, ghost images will appear.

### 5.8 Extending depth of field

LIFT's depth of field can be extended by computationally refocusing the image at different depths and identifying the sharpest feature around some determined ROI for each pixel in the focal stack. Then, an all-in-focus image can be extracted from graph cut algorithms [105] at the expense of computational reconstruction time.

### 5.9 Depth retrieval

Figure 46 shows the image processing pipeline employed to reconstruct a 3D image from 1D data. As previously mentioned, in LIFT, we reformulate light field imaging as a computed tomographic problem so that 1D data from multiple projections is reshaped as a 2D sinogram where $\theta$ corresponds to each rotation angle. Then, the image is decompressed to 2D using tomographic reconstruction that we will see in depth in further sections. In this section we focus on how to obtain depth, similar to conventional light field.

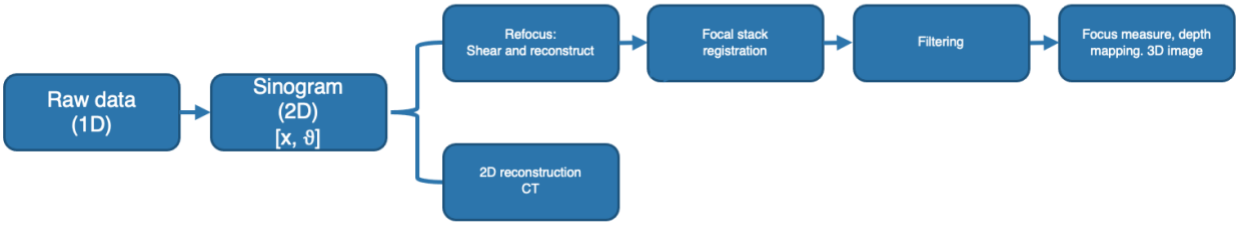


Figure 46: LIFT's image reconstruction pipeline

LIFT retrieves depth using depth-from-focus (DfF) algorithm [106]. The fundamental idea is to sweep the scene focal plane to get a focal stack and use a scoring technique to determine what is the best focused point within the stack and then estimate the depth of the point. The amount of focus (or defocus) is mainly determined by the high frequency content in the each image. Such quantity can be determined by algorithms such as sum of Laplacians. We take a small patch within the image and calculate the second derivative for each pixel and sum it. This is shown in Equation 37:

$$M(x,y) = \sum_{i=x-K}^{x+K} \sum_{j=y-K}^{y+K} \nabla_M^2 f(i,j) \tag{37}$$

where $i$ and $j$ are the different pixels in the 2D reconstructed image, and $K$ is the rectangular window size. Then, the focus measure $M(x,y)$ can be mapped to a depth value.

In practice, refocusing the light field image induces shift between multiple slices within the focal stack. Thus, we first use one image as a reference and we calculate the geometric relationship with respect to other images and apply a transformation. Furthermore, defocused images display artifacts that are denoised using a block matching and 3D filtering algorithm (BM3D). BM3D is a collaborative filtering process in which groups of similar blocks are extracted from the image if

some dissimilarity measure falls below a threshold. All blocks are then stacked in 3D and Wiener filtering is performed equally.

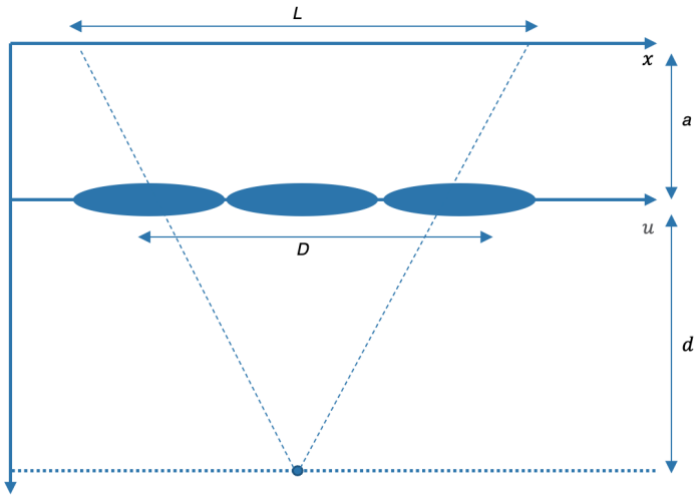


Figure 47: Focus-to-depth LIFT

Figure 47 illustrates the focus-to-depth process. If an object plane is located at distance $d$ from the lenslet array, the total distance between the leftmost and rightmost subapertures images is equal to:

$$L = \frac{d + a}{d} D$$

where $D$ is the baseline lenslet array length and $a$ is the distance from the array to the sensor plane. To connect distance $d$ with the computationally image refocusing parameter $s$ we can consider that the array length at infinity is $L_\infty = D$. We can now calibrate the system to generate a quantitative 3D map by translating a point source across the depth of field of our LIFT microscope. Then, we generate a curve to match the ground truth axial position with the lateral shift of the line spread function at each measurement. Finally, we can fit that measurement and output a focus-depth calibration curve, which is shown in Figure 48:

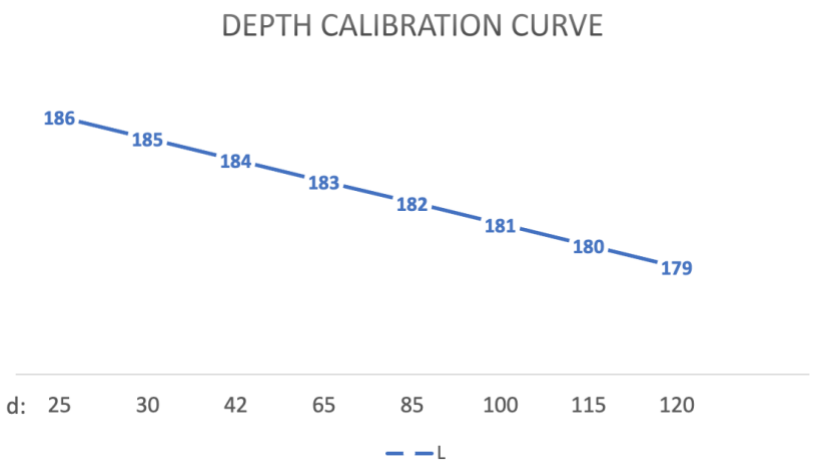


Figure 48: Focus-to-depth calibration curve

### 5.10 Image compression

Figure 49 shows how conventional light field and LIFT pixel extraction differ from each other from an artificial brain image. In light field, since we normally use spherical lenses, we need to utilize every row from the CMOS sensor. However, LIFT only requires 3 rows in the case where the microlens array is a 3x3 matrix. Thus, LIFT's image compression enables high speed imaging.

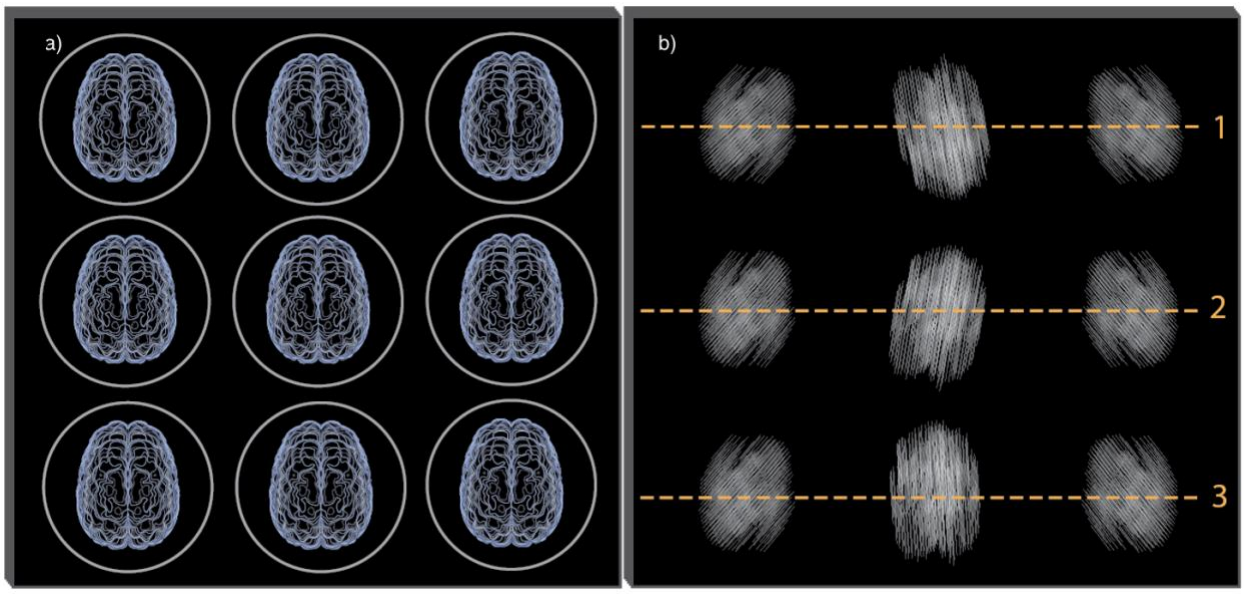


Figure 49: CMOS sensor plane using a) Light field imaging; b) LIFT imaging

### 5.11 Fourier LIFT

In LIFT microscopy, we will implement an optical design that is based on Fourier light field imaging due to its benefits that are explained later in this section. Let us first see a conventional light field optical system where the microlens array (MLA) is placed at the native image plane of the tube lens. Figure 50 is a schematic of such concept. The camera sensor is placed at one focal distance away from the microlens array. To avoid overlapping between different sub images at the sensor plane, the numerical aperture (NA) at the imaging plane must match the MLA's NA. This is expressed in Equation 38.

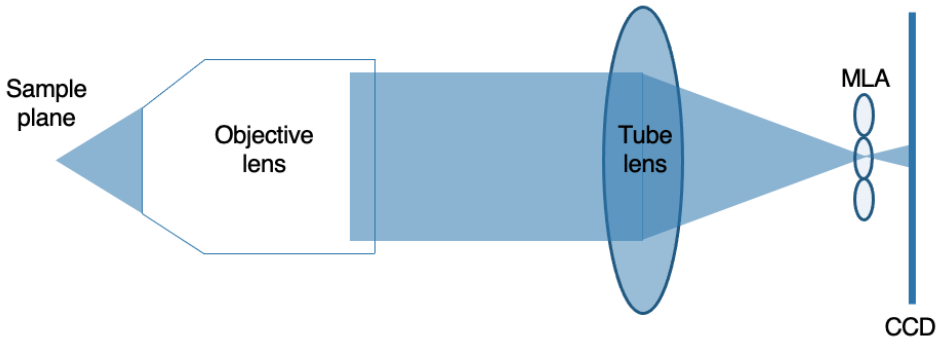


Figure 50: Conventional light field microscopy

$$\frac{NA_{objective}}{M} = \frac{p}{2f_{MlA}} \tag{38}$$

where $M$ is the objective's magnification, $p$ is the MLA's pitch, and $f_{MLA}$ is the MLA's focal length. This implementation presents practical problems in which if the MLA pitch is relatively low because we need to either increase the objective's magnification and reduce the objective's NA thus reducing the resolution. An alternative is to place the microlens array at the back focal plane of the objective lens. This is concept is known as Fourier light field microscopy illustrated in Figure 51:

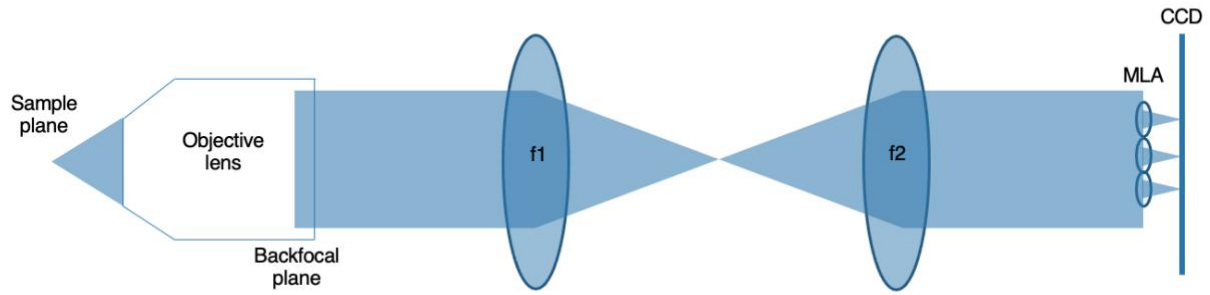


Figure 51: Fourier light field microscopy

In this case, since we do not have direct access to the Fourier plane of the objective lens, we can place relay it using a 4f system with lenses L1 and L2. Then, the MLA has direct access to the pupil plane and divides its aperture retaining both spatial and angular information.

### 5.12 Unfocused LIFT

One of the main drawbacks in LIFT is low light throughput due to the image along invariant optical axis size at the sensor plane. Information from a single pixel in the object plane is spread along rotation direction in the image space with a magnification dependent on the size of the lenslet and the focal length ratio. This hamper's LIFT's application especially in fluorescent imaging since this is a photon starving application and line spread function might be buried in sensor's shot noise. For this reason, we need to modified Fourier LIFT setup into unfocused Fourier LIFT microscopy, shown in Figure 52:

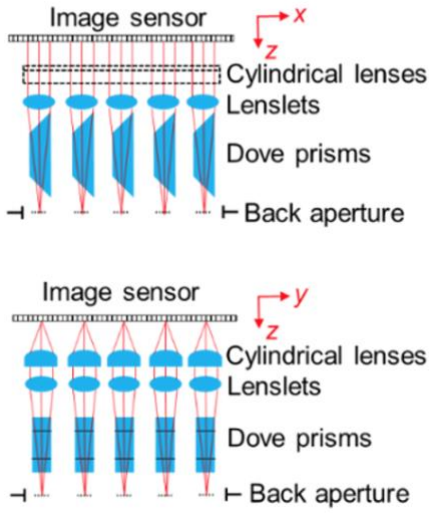


Figure 52: Unfocused LIFT

Here, we introduce a spherical microlens array behind the Dove prism at one focal length away from the objective lens' back aperture. Figure 52a represents XZ plane, where the cylindrical lens has no optical power. Then, the chief rays will collimated by the lenslet, pass through the cylindrical lens without being refracted and form an image at the sensor plane. In contrast, at the YZ plane, where cylindrical lens has optical power, the collimated chief rays will be focused by the cylindrical lens on the sensor. This means that on the y-axis we will image each sub pupil corresponding to the exit pupil image of the back aperture of the objective lens in Fourier light field configuration. Since the LIFT camera is imaging the light field of the pupil, we consider this setup as unfocused LIFT [107] [108].

### 5.13 System design

LIFT is a general technique that can be applied to multiple setups including microscopy, non-line-of-sight, and hyperspectral imaging. In my research, the main goal is to image fluorescent, fast

dynamics events such as neuronal action potentials so all my systems are applied towards fluorescent microscopy.

### *5.13.1 First order design*

Figure 53 shows a general schematic of a LIFT microscope's first order design. The targeted resolution is roughly 2-3μm and the FOV should be no less than 200μm for our imaging applications.

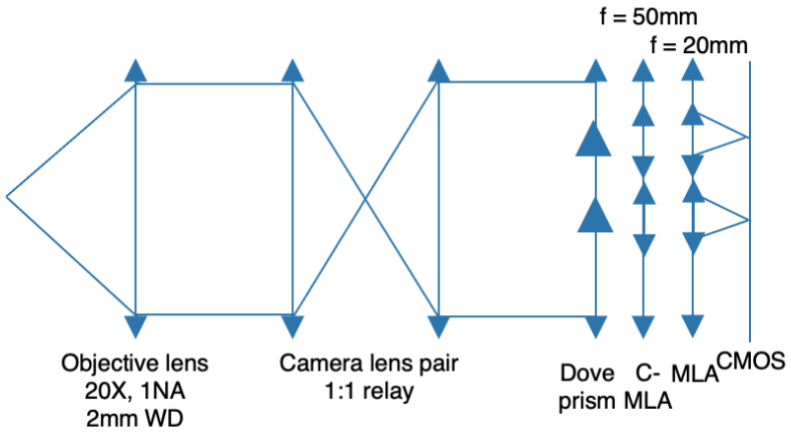


Figure 53: First order paraxial design of an unfocused Fourier LIFT microscope

Since LIFT is a computed tomography based imaging technique, we want to have as many projections or views of the object as possible to accurately reconstruct the object. Thus, the back aperture of the objective lens, given by Equation 39, should be as large as possible:

$$D_{backaperture} = 2fNA \tag{39}$$

Thus, the focal length and the NA of the infinity corrected objective lens should be maximized. I selected a low magnification, which provides longer focal length, high NA objective lens: 20X Olympus XLYMPLFLM Objective, 1.00 NA, 2.00mm WD. Although the relative long working distance is not an LIFT requirement, it will be a sample requirement in future sections such as in

vivo mouse brain imaging. With these parameters, the back aperture diameter should be around 18mm. Then, a 1:1 system is used to relay the back aperture plane of the objective lens to an accessible point, since it is usually inside the objective's housing. I used two SLR Magic Lens II 50mm f/1.1 due to its relatively large entrance and exit pupils in order to avoid spherical aberrations. Furthermore, the Dove prisms are placed at the relayed pupil plane. Collimated light should avoid astigmatism. There is a tradeoff between the chosen number that will fit in the back aperture (number of projections in CT reconstruction) thus affecting the imaging quality reconstruction and the lateral resolution. This is not determined by the Dove prisms but the cylindrical lens array instead, since there needs to be a one-to-one match for every sub pupil position and we need to the PSF needs to be twice the camera's pixel size to meet Nyquist's sampling criteria.

The selected camera is a Teledyne Kinetix CMOS camera. There are several reasons why I choose this 2D camera instead of a 1D sensor for LIFT imaging. Firstly, due to its multi ROI capabilities, this means that we can convert the sensor into a multiplexed LIFT system where we extract a few rows from the sensor and we can highly increase the number of projections. The back part of the LIFT microscope illustrates such idea (Figure 54):

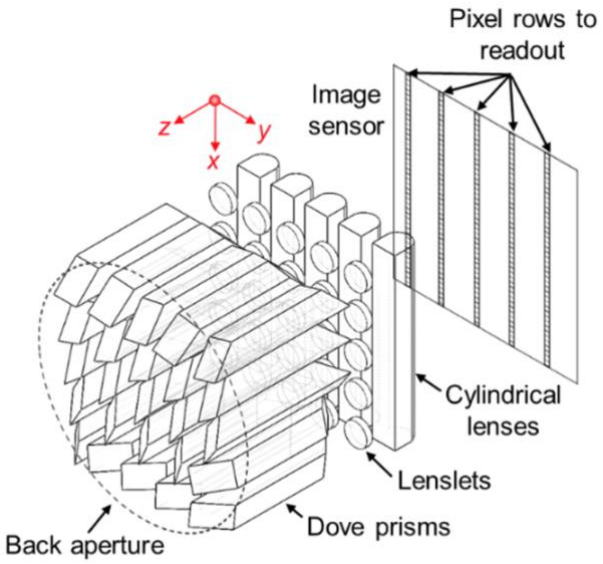


Figure 54: Unfocused LIFT ROI multiplexing concept

If we were to use a single row to readout data, a line sensor would be sufficient. However, the number of projections would be limited to less than ten considering the optical design parameters and the reconstruction results for very sparse CT problems would be considerably poor in biological samples, which are considered as non-sparse. The increase of the number of projections comes at a cost: speed. As we increase the number of pixel rows to readout, the frame rate is reduced (see Section 5.10) but the data compression is still much higher than conventional light field imaging.

The second reason behind camera selection is quantum efficiency, which is 95%. As mentioned, fluorescent imaging is a light starving application. Thus, it is key to convert as much photons into electrons as possible. The third reason is the large diagonal field of view, almost 30mm, which allows a big number of projections. Finally, the Kinetix model allows high frame rate imaging, we will see the exact frame rate in future calculations.

Regarding the cylindrical lens' parameters, they are designed and optimized using ZEMAX and later fabricated. Its focal length and diameter depends on the desired pupil plane image size. This

is the line spread function length mentioned in unfocused LIFT section: we want to make it as small as possible to optimize light throughput. Lastly, the conventional MLA that images the object needs to be designed considering desired resolution and FOV. Overall, LIFT's first order design calculations are shown below. The total system magnification is equal to:

$$M = \frac{f_{MLA}}{f_{obj\ lens}} = \frac{f_{cyl\ lens}}{\frac{f_{std.tube\ lens}}{M}} = \frac{50}{180/20} = 5.55X \tag{40}$$

The lateral resolution is determined by the MLA's NA (Equation 41). The selected parameters are at an optimal tradeoff between number of projections and lateral and angular resolution.

$$NA_{MLA} = \frac{R_{MLA}}{f\_MLA} = \frac{1}{50} = 0.02 \tag{41}$$

Moreover, the PSF at the sensor plane will be:

$$PSF = \frac{\lambda}{2NA} = \frac{532E-9}{2 * 0.02} = 12\ \mu m \tag{42}$$

which is approximately twice the Kinetix's pixel size (6.5μm) so Nyquist sampling criteria is met. Then, the pixel at the at the object plane will be:

$$Lateral\ resolution = \frac{PSF}{M} = \frac{12\ \mu m}{5.6} = 2.14\ \mu m \tag{43}$$

and the field of view limited by the MLA:

$$FOV = \frac{D_{MLA}}{M} = \frac{2mm}{5.6} = 350\ \mu m \tag{44}$$

On the other hand, the vertical direction that images the pupil for unfocused LIFT configuration will have a size of:

$$d_{MLA}\frac{f_{cl}}{f_{MLA}} = 2\frac{10}{50} = 0.4\ mm \tag{45}$$

which is equivalent to approximately 66 rows in the Kinetix camera and an output of 4800Hz at 8 bit dynamic range and 1000Hz at 16bit. This is a one order of magnitude increase with respect to

conventional light field imaging. In conclusion, LIFT unfocused Fourier configuration can reconstruct three dimensional scenes with a 350µm FOV, 2µm lateral resolution at thousands of frames per second.

### *5.13.2 Application design: fluorescence imaging*

Figure 55 shows a LIFT microscope configured for our main application: fluorescent imaging. Starting from the top side, in LIFT, we image the pupil along the invariant optical axis and the object along the plane perpendicular to the sensor rows.

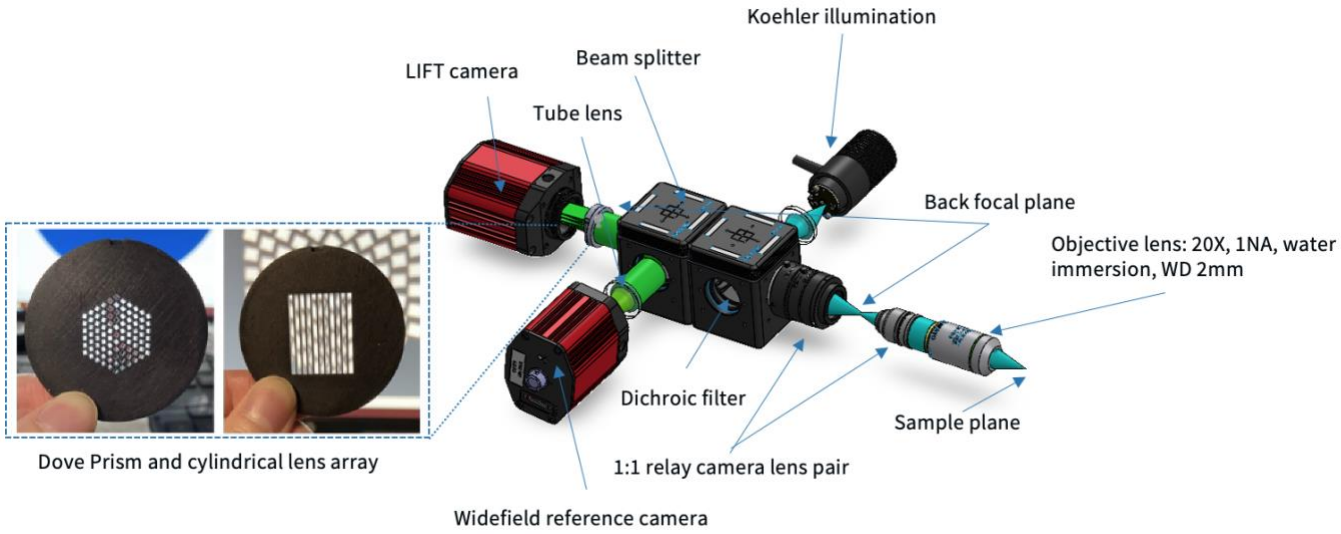


Figure 55: LIFT reflective fluorescence microscope

A 90:10 beam splitter is placed on the optical path to have two arms: a reference arm with a conventional tube lens for widefield acting as a reference camera and capturing 10% of the light while still maximizing the transmitted (90%) of light to the LIFT arm. Finally, a replaceable filter cube is used to maximize both fluorescent excitation light at the sample stage by using a excitation filter, a 45º degree dichroic mirror, and emission wavelength coming from the sample. The LED light source is at the conjugate plane of the objective's lens back aperture thus providing Koehler illumination. For more information of the setup please refer to previous section 5.13.1.

## 5.14 Reconstruction techniques

Now that we know how to compress three-dimensional scenes into one-dimensional sensors and understand LIFT's refocusing, extended depth-of-focus, and high speed imaging capabilities, we can focus on 1D to 2D image reconstruction. As mentioned before, LIFT reformulates imaging as a sparse computed tomography (CT) reconstruction problem and this is a well-established field. We will review the algorithms that we used to reconstruct LIFT images.

### *5.14.1 Backprojection*

The most rudimentary algorithm in CT reconstruction is backprojection [109]. It consists of mathematically mapping the attenuation pathway at every angle measured. In order to understand backprojection algorithm let us first visit the mathematical description of analytical projection $L$ from a certain angle $\theta$ at $t$ intersection with respect to some detector of a two-dimensional object $f(x, y)$ represented in Figure 57. This is the same concept as the Fourier slice theorem.

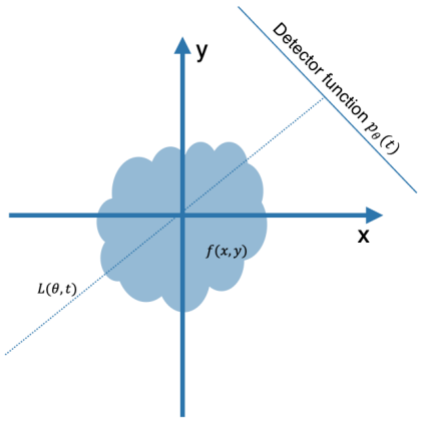


Figure 56: One-dimensional projection of a two-dimensional object along arbitrary angle

The detector function $p_\theta(t)$ is the resampled line sensor describe in previous sections (see Section 5.3). The projection can be described by Equation 46:

$$L(\theta, t) = \{(x, y) \in R\ x\ R: x cos\theta + y sin\theta = t\ \} \tag{46}$$

If we project the object along all possible angles we will end up with an integral known as the Radon transform that captures the all necessary information to reconstruct the object in the projection domain:

$$Rf = \int_L^L f(x, y) ds \tag{47}$$

In practice, the Radon transform is discretized and does not contain all possible viewing positions. Instead, a set of discretized limited integral is organized into a 2D function with $x$ and $\theta$ variables. This is known as a sinogram, since a Delta function in the object domain will be expressed as a sinusoidal pattern in the projection domain. Figure 58 shows a typical LIFT sinogram from a USAF resolution target. This is a linear operator so we can consider that any object is expressed a sum of sinusoidal waves. The x-axis contains the line integral and the y-axis the cylindrical lens rotation angle. The backprojection algorithm will map the sinogram to the object domain.

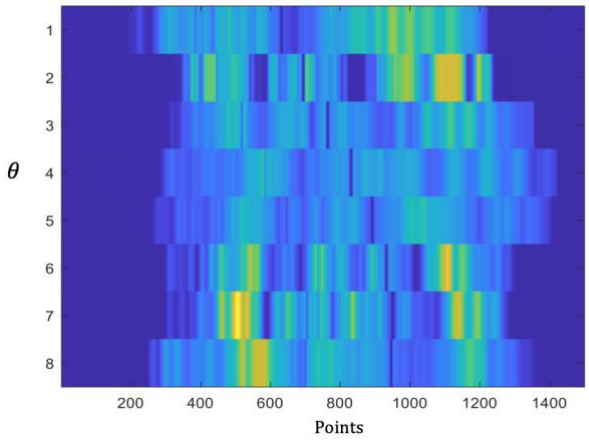


Figure 57: LIFT sinogram of a USAF target

In order to extract a final image from the sinogram domain, we smear the one dimensional projection information along the rotation angle for each acquired projection. Mathematically we can express this step as:

$$f_{bp} = \int p_\theta(x\ cos\theta\ + y\ sin\theta)d\theta \tag{48}$$

This will lead to an object reconstruction that will be blurred due to the nature of projection sampling. This effect can be explained in the frequency domain: low frequencies are oversampled and high frequencies undersampled. In order to solve this issue, a high pass filter is typically used. To do so, the projection function is transformed in the Fourier domain and multiplied by the filter. There are multiple filter designs. For brevity purposes, we will not dig into filters and consider the gold-standard for CT reconstruction: Ram-Lak filter. Then, the low frequencies are suppressed and the high frequencies are amplified. Finally, the filtered version is inverse Fourier transformed and later backprojected. Mathematically this looks like Equation 49:

$$f_{fpb} = \int q_\theta(x\ cos\theta\ + y\ sin\theta)d\theta \tag{49}$$

with

$$q_\theta(t) = \int P_\theta(\omega)|\omega|e^{i2\pi\omega t}d\omega;$$

Although backprojection allows us to reconstruct images from different projections, LIFT's sparse CT nature needs more advanced techniques to obtain high quality imaging metrics. Thus, iterative and deep algorithms will be now explained.

### *5.14.2 LIFT's forward model*

In order to understand the iterative reconstruction LIFT algorithm, let us first formulate the forward model. As previously mentioned, LIFT reformulates imaging as a CT problem. Now let us merge

both concepts into modeling equations. The 1D projection intensity at the sensor plane $L(\theta, t)$ can be considered as a convolution of an ideal pinhole image $o(x, y)$ and the line-shaped PSF from the cylindrical lens, that is:

$$L(\theta, t) = [o(x, y) * \delta(x \cos\theta + y \sin\theta)]_{x=k, y=0} \tag{50}$$

where $\delta(x, y)$ is the Delta Dirac function, x, $y$ denote the image space coordinates, and $k$ is the local coordinate on the sensor behind each lenslet. By convolution's definition, Equation 50 is equal to Equation 51:

$$L(\theta, t) = \iint_{-\infty}^{+\infty} o(x, y)[\delta(x - k)cos\theta + y\, sin\theta]\, dxdy \tag{51}$$

From this equation, we can extract that in LIFT the object projection along certain angle is equivalent to rotating the object and integrating along the $y$ direction. Then, by discretizing the model we can consider LIFT's forward model as:

$$L(\theta) = TR_\theta g \tag{52}$$

where $T$ is the integration, $R_\theta$ is the rotation matrix, and $g$ is the original object. We could use backprojection to reconstruct this data. However, since we now know the forward model, we can use inverse reconstruction algorithm to get a more accurate representation of the object.

### *5.14.3 Iterative reconstruction*

In previous Equation 52, the goal is to extract the unknown vector $g$ by solving the linear system of equations. Ideally, we would multiply the inverse of the integration and rotation matrix $T$, and $R_\theta$, respectively with the projection data. Unfortunately, the integration and rotation matrices are not invertible since they are not squared and the system is typically undetermined due to the relatively low number of projection lenses in LIFT system. Thus, we only have access to an

approximate solution given by the minimum projection distance in some norm. To find optimal value we need to solve this problem iteratively.

$$g^* = argmin \left||b - Ag|\right|^2 + \rho\Phi(\mathrm{g})_1 \tag{53}$$

where φ(g) is a transform function that sparsifies the image, $._1$is the l1 norm, and ρ is a regularization parameter. Various transform functions like total variation, wavelet transform, and discrete cosine transform, can be used to make the image representation sparse. This equation may be solved using an accelerated convergence version of the proximal gradient descent method: fast iterative shrinking thresholding algorithm (FISTA) [110]. For the sake of brevity, I will only explain the underlying algorithm [111].

Proximal gradient descent is a technique that solves L1 regularized least squares problem, comprised by a two-step alternating process. The first is two calculate least squares gradient descent from the current weight $g$, that is:

$$z_k = g_k - \tau A^T(Ag_k - b) \tag{54}$$

where τ is the step size. The second step is solving the close (proximal) regularization problem:

$$g_{k+1} = argmin_g \left||z_k - g_k|\right|_2^2 + \tau\lambda\left||\mathrm{g_k}|\right|_1 \tag{55}$$

### *5.14.4 Deep learning approaches*

As we know, LIFT is a compressive imaging technique that highly increases three-dimensional data acquisition at the cost of resolution. We are currently investigating how to compensate resolution loss using deep learning. It has already been demonstrated that some sparse CT algorithms are capable to reconstruct high resolution from low resolution ones with adequate

system training [112]–[116] . In this case, our ultimate goal is to make LIFT achieve diffraction limit resolution while maintaining kilohertz frame rate.

### 5.15 LIFT system characterization

In order to test LIFT  fluorescence microscope's lateral and axial resolution I placed an microLED screen (Microled-info) with 5μm pixel size at the sample stage and turned on two pixels with a one pixel separation and kept increasing the separation until resolving both points using LIFT in a 7 lenslet (projection) configuration: Figure 59 shows the line reconstruction results. As it can be seen, both points can be differentiated less than 10μm apart and that determines LIFT's lateral resolution between 5-10 μm. It is important to note that this resolution depends on the number of projections and the sample. For a more spatially complicated (non-sparse) sample, we usually scale the number of lenslets up to match the required resolution.

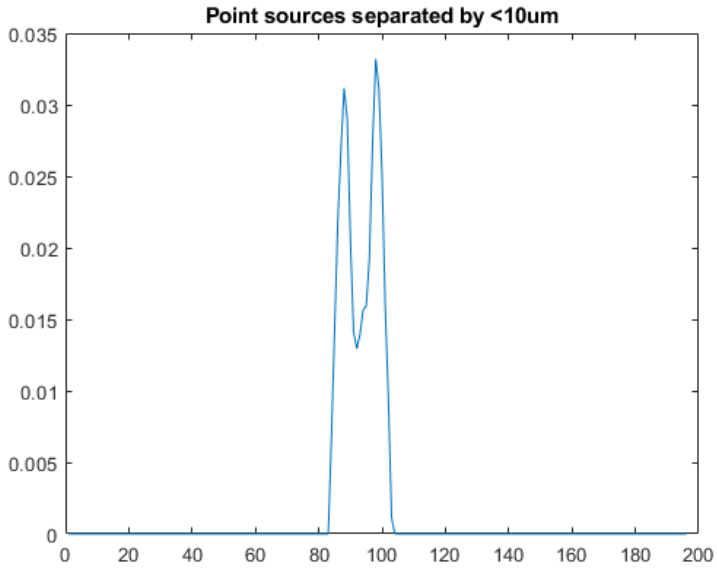


Figure 58: LIFT's lateral resolution

Regarding axial resolution, I took a single point source and scanned it in the axial direction with 5 μm increments. As a reminder, LIFT's axial resolution can be experimentally determined by the

amount of travel that takes cylindrical lens PSF to shift one pixel and thus be able to later differentiate. Figure 60 shows refocusing  collage of data from the summed images of two point located 40µm away from each other:

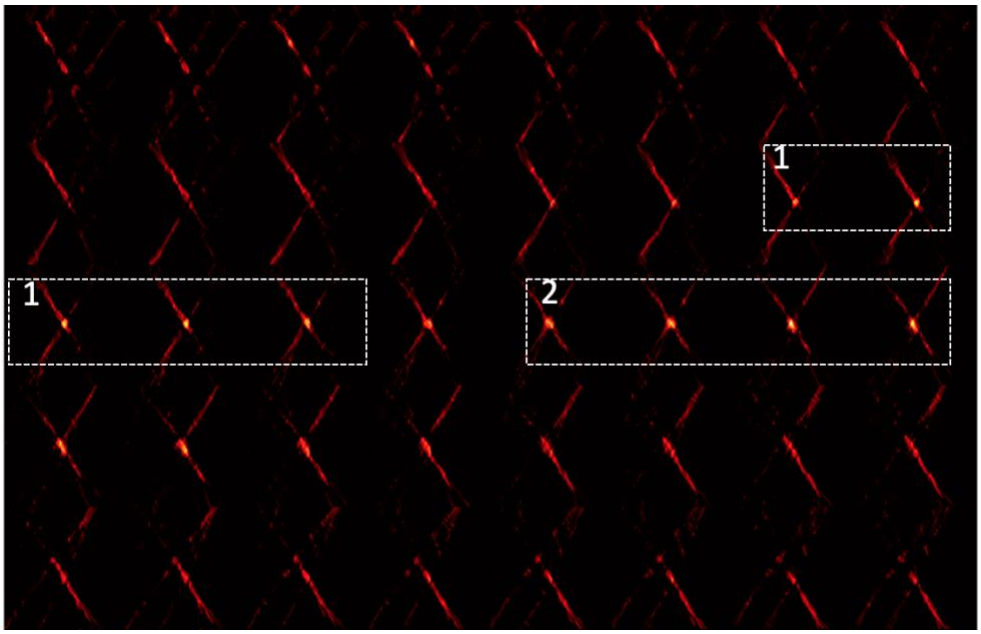


Figure 59: LIFT's experimental axial resolution

The highlighted areas showcase the first and second point being refocused, respectively. There is a profile separation similar to Figure 59 where the separation is less than the FWHM of each individual PSF thereby determining 40µm of axial resolution .

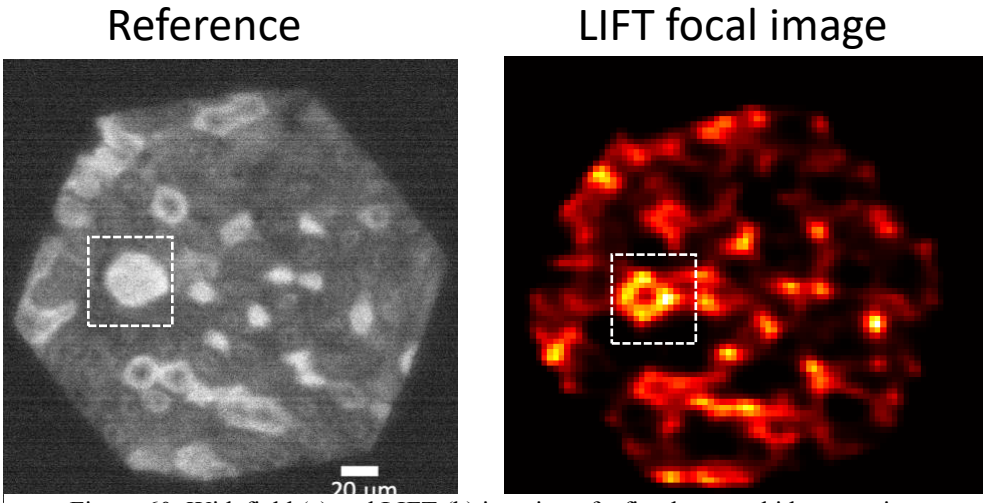


Figure 60: Widefield (a) and LIFT (b) imaging of a fixed mouse kidney section

Furthermore, in order to demonstrate that LIFT is able to accurately reconstruct fluorescent biological samples, I placed a prepared Thermofisher fluorescent slide of a mouse kidney section where the glomeruli and convoluted tubules are labeled by Alexa Fluor 488 wheat germ agglutinin dye. Figure 60a, and 60b show the reference widefield image and the LIFT enface focal image, respectively. As it can be seen, the resolution on the LIFT focal image is not diffraction limited, as with widefield. This is due to LIFT's sparse CT nature, in this case by using 16 projection lenses. However, the number of projections can be scaled up until achieving near diffraction limited resolution. In the highlighted region, we can already note a key difference between widefield and LIFT; this feature is hollow in LIFT. This is due to LIFT's 3D imaging nature in which we can see through some occlusions while widefield integrates the axial dimension hereby losing refocusing capabilities. In LIFT, we can extended the focal image to render a 3D volume. This is shown in Figure 61. The capability to image 3D scenes with a single snapshot at thousands of frames per second opens a huge number of applications including brain, cardiovascular, microfluidic, imaging that will be seen in depth in further sections.

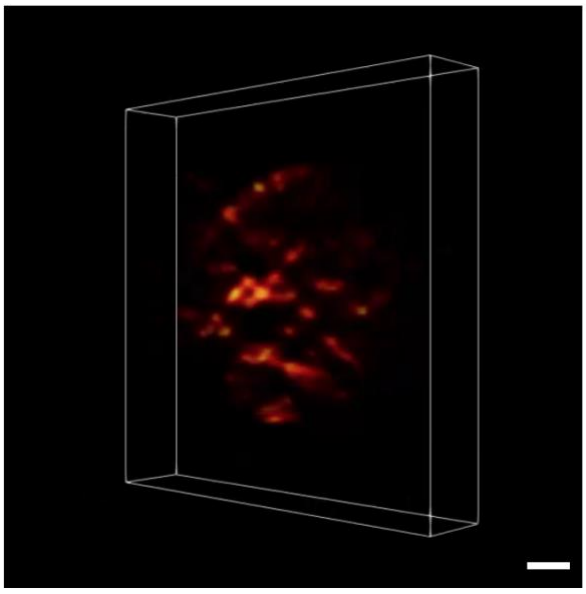

Figure 61: 3D LIFT rendering of mouse kidney section in Fig.60. Scalebar: 20um

## 5.13 Applications

LIFT is a general optical compressive technique that can potentially be applied to many scenarios such as tomography, microscopy, general-purpose cameras or hyperspectral imaging. During my graduate research, I focused on the LIFT applications that can have a greater impact in our society. One of them is neuronal imaging. To date there is no technique that can image three dimensional volumes at kilohertz rates of action potentials. Moreover, the study of microfluidics, the behavior of fluids constrained to a small scale, has a huge impact in DNA chips, molecular biology, evolutionary biology, optics, fuels, food science, etc. It is essential to understand such dynamics and LIFT could potentially provide 3D info at high speeds. Lastly, cardiovascular imaging plays a pivotal role in human biology. Particularly, cardiac atrial fibrillation is a common cardiac arrythmia and a major contributor to stroke.

### *5.15.1 Brain imaging*

High-speed volumetric imaging of dynamic neural activity over long periods still remains a big challenge in neuroscience. To this date, light field microscopy can get single snapshot three-dimensional reconstruction but its speed is still limited to a few hundred frames per second. This allows light field imaging systems to capture genetically encoded calcium indicators (CECIs). However, calcium imaging is not exactly related to the voltage change in neurons, it only provides a limited information about natural signal processing and little information about the inhibitory and exhibitory neural signals. In contrast, voltage imaging allows directly measuring neural electrical activity and can overcome calcium imaging limitations. Particularly, genetically encode voltage indicators (GEVIs) are fluorescent electrosensitive molecules that change it brightness depending on neural voltage. Unfortunately, the temporal resolution needed to image such neuronal action potential is on the order of milliseconds and conventional light field imaging is

not suitable for this application since there is a tradeoff between imaging speed and signal-to-noise ratio (SNR).

On the other hand, our LIFT microscope for fluorescent imaging meets all requirements for this application: high-resolution, high-volume, and high-speed. Our ultimate goal is to optimize LIFT for kilohertz volumetric imaging of neuronal action potentials. To prove this, I first tried to see lower temporal resolution dynamics and higher SNR molecules with GECIs to empirically optimize the system parameters for GEVIs. Thus, I set up a imaging chamber to record GCaMP activity from acute brain slices (see Appendix A for general protocol). Figure 6 illustrates such setup:

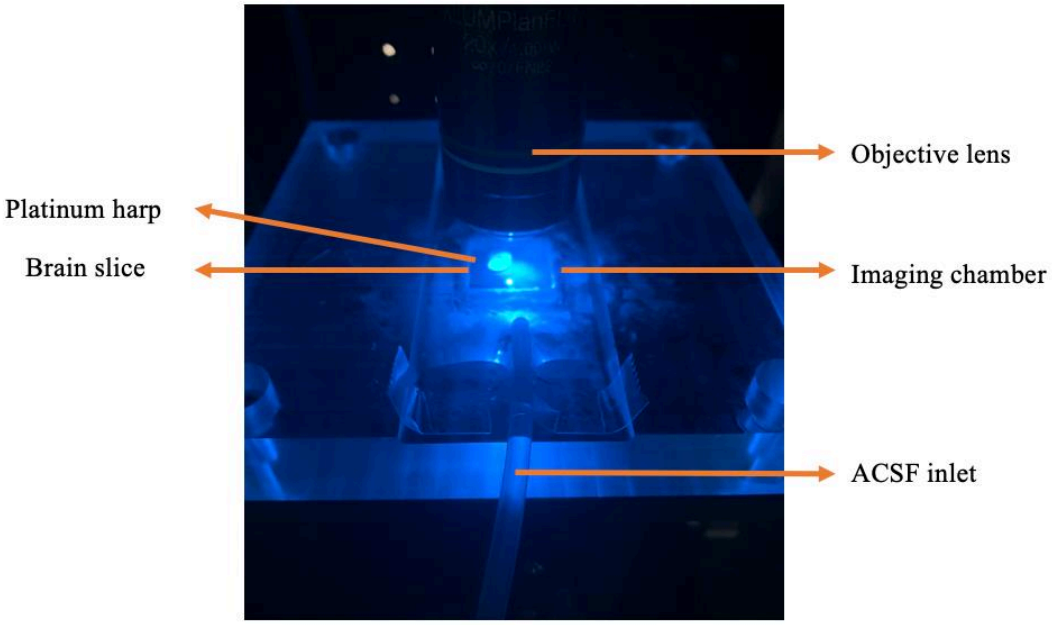


Figure 62: LIFT acute brain slice imaging setup

In order to preserve the physiological conditions of the brain slice we need to constantly perfuse fresh artificial cerebral spinal fluid (ACSF). A carbogen (95% O2, 5% CO2) tank keeps the ACSF solution saturated. Then, a 3D printed imaging chamber with an input channel for fresh ACSF and

output that goes to a discard chamber (not shown) perfuses the ACSF. The sample is held by a platinum harp to keep it steady at the bottom of the chamber. Once the slice is held in place we circulate a high potassium ACSF, which is known to activate neurons. Figure 63 shows such GCaMP activity in LIFT imaging. As it can be seen, after recording ACSF is applied, some neurons show a change in fluorescence with respect to its baseline. Our next step is to test these signal GCaMP in vivo by looking through an craniotomy window in brain and substitute GECIs with GEVIs.

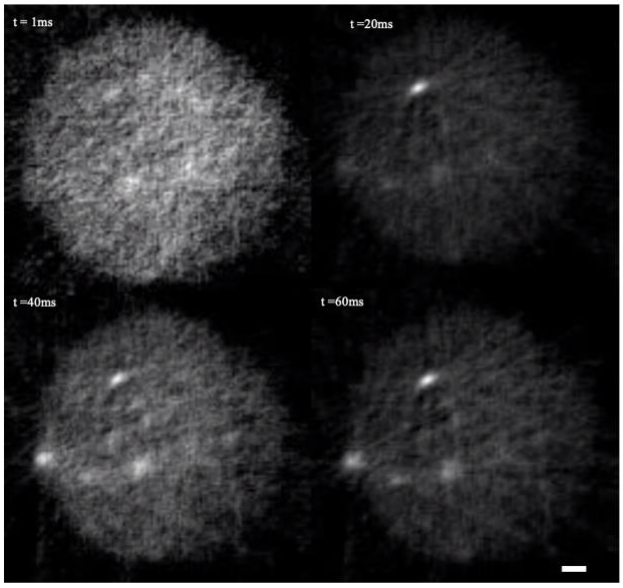


Figure 63: Acute brain slice GCaMP activity using LIFT microscopy. Scale bar: 10um

### *5.15.2 Microfluidics*

Three-dimensional high-speed imaging in microfluidics application is key requirement to understand its dynamics. To probe LIFT's capabilities, we tested 3D imaging on microfluidic sculpting channels. In this technique, we can place certain barriers in the microfluidic channel in a specific spatial location, predict, and sculpt how a liquid is going to flow through the channels. In this experiment, a barrier is placed at an arbitrary position in a microfluidic channel (Figure 64).

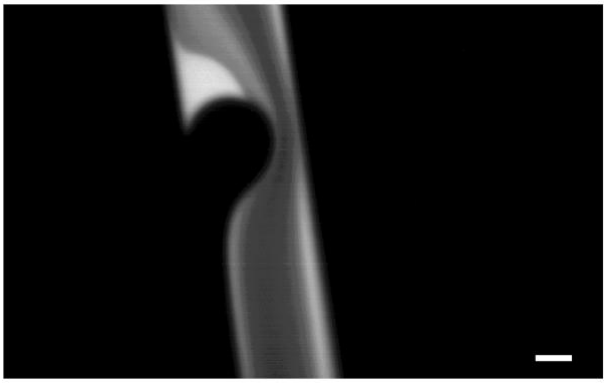

Figure 64: Barrier in a microfluidic channel for flow sculpting. Scale bar: 20um

Then, Figure 65 shows of how the fluid is shaped in 3D at 2000fps. Such frame rate is not a limitation: since this is an image with relatively low frequency features we could use a low number of projections, less ROIs and image at tens of thousands of frames per second.

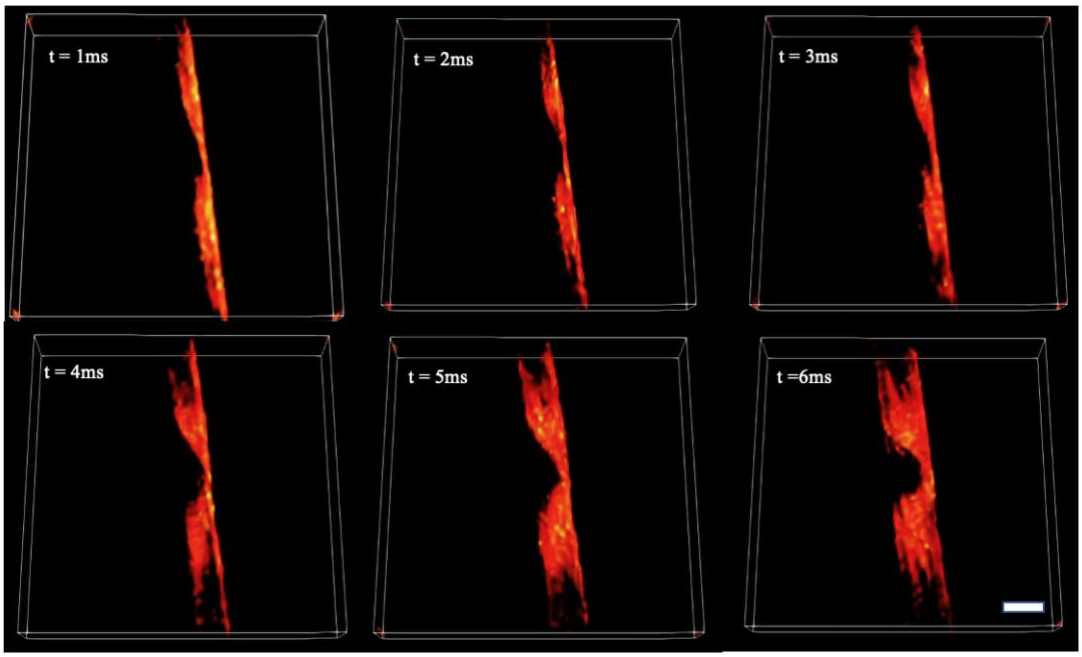


Figure 65: 3D flow sculpting through LIFT imaging. Scalebar: 50um

### *5.15.3 Cardiovascular imaging*

One of LIFT's main application is cardiovascular imaging of voltage waves in a fast beating zebrafish heart since it requires high spatiotemporal resolution and there is currently no technique that can address such needs. The embryonic zebrafish is a genetically tractable and transparent model that allows the study of electromechanical coupling in heart development: the dynamics and relationship between action potentials and myocardial contraction. This would help cardiologists better understand major fatal risk factors such as cardiac atrial fibrillation, a cardiac arrythmia and a major heart stroke cause in which there is a dysregulation of the electrical and mechanical coupling.

As a proof of concept, I demonstrated in vivo dynamic 3D blood flow imaging at near kHz speeds. We labelled RBCs in the tail of a zebrafish larvae (tg:gata1:dared, 4dpf) with dsRed fluorophore. Figure 66a shows the widefield (reference) camera dynamics while Figure 66b shows the LIFT images. LIFT also allows cross sectional imaging, which is shown in Figure 66c, we can now track single RBCs in 3D at thousands of frames per second.

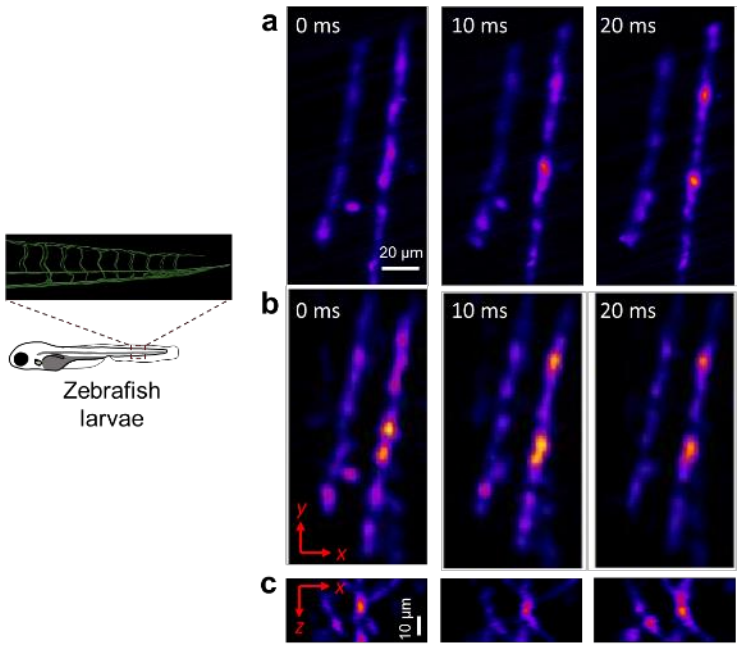


Figure 66: Dynamic imaging of red blood cells flowing in a zebrafish larvae in vivo

Furthermore, Figure 67 demonstrates calcium signaling imaging in LIFT microscope where a single cell expresses GCaMP. Calcium release from the sarcoplasmic reticulum occurs toward the myoplasm along the length of the cell. This figure shows how two signals propagate in opposite directions and later merge into a single signal.

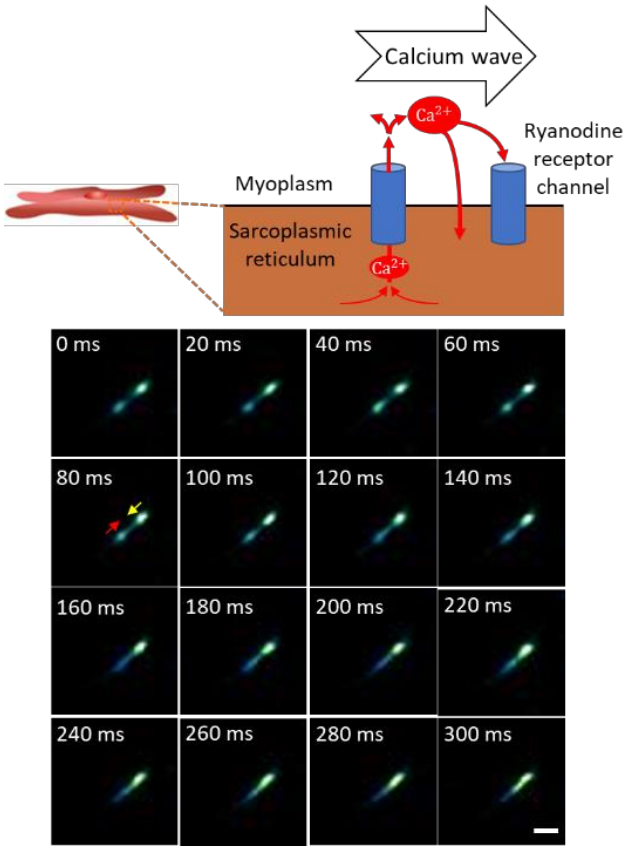


Figure 67: LIFT imaging of calcium waves propagating in a cultured cardiomyocyte expressing GCaMP. Scalebar: 40um

### 5.16 Discussion and future work

LIFT is a general optical technique that can span many applications. The basic principle is to compress three-dimensional information to a one-dimensional detector in order to highly increase data throughput. LIFT can extract 3D information from the same principle as conventional light field imaging: dividing the aperture into multiple sub apertures. Since each sub aperture has a different perspective of the object, we can see through occlusions assuming that the object is sparse. Then, the scene can be further compressed into a line sensor if we judiciously use cylindrical lenses and rotate them along certain orientations. This is a key step in LIFT: reformulating imaging as a CT problem . At the sensor plane, we detect projections from the object and each projection has a unique perspective of the object. We can later reconstruct the scene using

classic CT reconstruction techniques for 2D and light field shear and reconstruct algorithm for 3D. LIFT has the same refocusing and extended depth-of-field capabilities as with conventional light field imaging.

Since there is only a fairly limited number of lenses that we can fit within the objective's back aperture, LIFT is further considered as a sparse CT problem: a few number of projections are only able to image simpler objects. If we want to improve the system's imaging capabilities we can either reduce the size of each projection which reduces the NA of each lenslet or use more advanced reconstruction techniques such as iterative and deep learning methods which can effectively reduce imaging streaking artifacts. Moreover, I have demonstrated LIFT imaging in microscopy applications. LIFT enables high-speed 3D imaging of many biological events. Particularly, in this dissertation we have visited neuronal, microfluidic, and cardiovascular imaging.

Regarding future work, LIFT's microscope can be expanded to any applications that requires high speed 3D imaging. In our lab will focus on capturing neuronal action potentials in brain mouse in vivo at kilohertz rates, microfluidics for flow cytometry application collaborations, and cardiovascular voltage wave imaging.

## Appendix A

## Acute brain slice protocol

1. Mice. Since our goal is to image GCaMP activity in mouse brain slice we can select any transgenic mice expressing GCaMP or perform viral injection. In this case we opted for viral injection at prefrontal cortex due to familiarity with the protocol.
2. GCaMP injection.
3. Obtaining acute brain slices.

3.1 Materials:

- Nest beaker: BSK4 Brain Slice Keeper.
- Instant superglue.
- Large scissors.
- Straight fine scissors (Fisher Scientific, 12000155).
- Dissecting fine-pointed forceps (Fisher Scientific, 08875).
- Scalpel (Fisher Scientific, 08925).
- Curved spatula (Electron Microscopy Sciences, 7832612).
- Industrial general purpose razor blade (Surgical Design, 270B).
- Dropper bulb (Fisher Scientific, 14060-11).
- Carbogen tank (95% CO2, 5% O2).
- Modified Pasteur pipette dropper.

3.2 Reagents:

- Sodium chloride (Fisher Scientific, 7647-14-5).
- Glucose (Sigma Aldrich, G7201).

- Sodium bicarbonate (Fisher Scientific, 144-55-8).
- Sodium phosphate monobasic anhydrous (Sigma Aldrich, 7558-80-7).
- Potassium chloride (Fisher Chemical, 7447-40-7).
- D-glucose (Fisher Chemical, 50-99-7).
- Magnesium chloride (Sigma Aldrich, 7786-30-3).
- Calcium chloride (Sigma Aldrich, 10043-52-4).
- NMDA (Sigma Aldrich, 6384-92-5).
- Isoflurane chamber.
- Vibratome.
- Ice-cold cutting artificial cerebrospinal fluid (ACSF) solution, see Recipes subsection.
- Recovery ACSF solution, see Recipes subsection.
- High KCl ACSF solution, see Recipes subsection.
- NMDA ACSF solution, see Recipes subsection.

3.3 Recipes:

- Cutting ACSF (in mM): 222 sucrose, 11 D-Glucose, 1 sodium phosphate, 3 sodium chloride, 7 magnesium chloride, 0.5 calcium chloride.
- Recovery ACSF (in mM): 124 sodium chloride, 2.5 potassium chloride, 26 sodium bicarbonate, 1.25 sodium phosphate, 10 D-Glucose, 4 sucrose, 2.5 calcium chloride, 2 magnesium chloride.
- High Kcl ACSF (in mM): 124 sodium chloride, 10 potassium chloride, 26 sodium bicarbonate, 1.25 sodium phosphate, 10 D-Glucose, 4 sucrose, 2.5 calcium chloride, 2 magnesium chloride.

- NMDA ACSF (in mM): 0.2 NMDA, 124 sodium chloride, 2.5 potassium chloride, 26 sodium bicarbonate, 1.25 sodium phosphate, 10 D-Glucose, 4 sucrose, 2.5 calcium chloride, 2 magnesium chloride.

4. Procedure
    1. Prepare ACSF solutions preferably on the imaging experiment day.
    2. Saturate all solution using carbogen for ~20 mins.
    3. Place cutting ACSF in the freezer until it reaches ~4 degrees Celsius.
    4. Prepare cutting tools and vibratome.
    5. Place mouse in isoflurane chamber until deeply anesthetized.
    6. Decapitate mouse using large scissors.
    7. Quickly extract the brain while dipping in ice cold cutting solution every ~10-20s.
    8. Isolate the brain's region of interest using razor blade.
    9. Place brain section in the vibratome and attach it using a small glue amount.
    10. Cover the whole cutting chamber with cutting ACSF.
    11. Cut slices to desired thickness (~300um).
    12. Using modified Pasteur pipette transfer the slices into recovery chamber (BSK4) filled with recovery ACSF while keeping carbogen bubbling.
    13. Let the slices recovery from mechanical slicing shock for 30 mins.
    14. Put the slices in the imaging chamber with a continuous and laminar flow of recovery ACSF solution.
    15. Change the input solution to high KCl ACSF or NMDA ACSF to activate the GCaMP signals.

## Chapter 6 Bibliography


[1] L. Schermelleh *et al.*, "Super-resolution microscopy demystified," *Nature Cell Biology*, vol. 21, no. 1. Nature Publishing Group, pp. 72–84, Jan. 01, 2019. doi: 10.1038/s41556-018-0251-8.

[2] L. v Wang and S. Hu, "Photoacoustic Tomography: In Vivo Imaging from Organelles to Organs." [Online]. Available: https://www.science.org

[3] Ng Ren, "Digital light field photography," *Stanford University*, 2006.

[4] E. H. Adelson and J. R. Bergen, "The Plenoptic Function and the Elements of Early Vision," MIT Press, 1991.

[5] X. Jiang, A. J. Qavi, S. H. Huang, and L. Yang, "Whispering-Gallery Sensors," *Matter*, vol. 3, no. 2. Cell Press, pp. 371–392, Aug. 05, 2020. doi: 10.1016/j.matt.2020.07.008.

[6] J. T. Mora, X. Feng, and L. Gao, "Photoacoustic shadow-casting microscopy," *Opt Lett*, vol. 44, no. 15, p. 3897, Aug. 2019, doi: 10.1364/ol.44.003897.

[7] L. v. Wang and L. Gao, "Photoacoustic microscopy and computed tomography: From bench to bedside," *Annual Review of Biomedical Engineering*, vol. 16. Annual Reviews Inc., pp. 155–185, 2014. doi: 10.1146/annurev-bioeng-071813-104553.

[8] S. Hu and L. v. Wang, "Optical-resolution photoacoustic microscopy: Auscultation of biological systems at the cellular level," *Biophysical Journal*, vol. 105, no. 4. pp. 841–847, Aug. 20, 2013. doi: 10.1016/j.bpj.2013.07.017.

[9] S. Hu, K. Maslov, and L. v Wang, "Second-generation optical-resolution photoacoustic microscopy with improved sensitivity and speed," 2010.

[10] J. Yao and L. v. Wang, "Sensitivity of photoacoustic microscopy," *Photoacoustics*, vol. 2, no. 2. Elsevier GmbH, pp. 87–101, 2014. doi: 10.1016/j.pacs.2014.04.002.

[11] W. Liu and J. Yao, “Photoacoustic microscopy: principles and biomedical applications”, doi: 10.1007/s13534-018-0067-2.

[12] B. Lan, W. Liu, and J. Yao, “High-speed Wide-field Photoacoustic Microscopy,” 2018.

[13] W. G. Zijlstra and A. Buursma, “Spectrophotometry of Hemoglobin: Absorption Spectra of Bovine Oxyhemoglobin, Deoxyhemoglobin, Carboxyhemoglobin, and Methemoglobin,” 1997.

[14] “https://commons.wikimedia.org/wiki/File:HbAbs_v3.png.”

[15] C. Zhang, K. Maslov, J. Yao, and L. v Wang, “In vivo photoacoustic microscopy with 7.6-μm axial resolution using a commercial 125-MHz ultrasonic transducer,” 2012, doi: 10.1117/1.

[16] A. C. Tam, “Applications of photoacoustic sensing techniques.”

[17] A. Petschke and P. J. la Rivì, “Diode lasers; (170.3880) Medical and biological imaging; (170.5120) Photoacoustic imaging,” 2010.

[18] J. Zhang, L. P. Smaga, N. S. R. Satyavolu, J. Chan, and Y. Lu, “DNA Aptamer-Based Activatable Probes for Photoacoustic Imaging in Living Mice,” *J Am Chem Soc*, vol. 139, no. 48, pp. 17225–17228, Dec. 2017, doi: 10.1021/jacs.7b07913.

[19] A. M. Winkler, K. Maslov, and L. v Wang, “Noise-equivalent sensitivity of photoacoustics Noise-equivalent sensitivity of photoacoustics Downloaded From: https://www.spiedigitallibrary.org/journals/Journal-of-Biomedical-Optics on 22 Oct 2022 Terms of Use: https://www.spiedigitallibrary.org/terms-of-use Noise-equivalent sensitivity of photoacoustics,” 2013, doi: 10.1117/1.JBO.18.9.097003.

[20] A. Rosenthal *et al.*, “Sensitive interferometric detection of ultrasound for minimally invasive clinical imaging applications,” *Laser Photon Rev*, vol. 8, no. 3, pp. 450–457, 2014, doi: 10.1002/lpor.201300204.

[21] E. Z. Zhang and P. C. Beard, “A miniature all-optical photoacoustic imaging probe,” in *Photons Plus Ultrasound: Imaging and Sensing 2011*, Feb. 2011, vol. 7899, p. 78991F. doi: 10.1117/12.874883.

[22] B. Dong, S. Chen, Z. Zhang, C. Sun, and H. F. Zhang, “Photoacoustic probe using a microring resonator ultrasonic sensor for endoscopic applications,” *Opt Lett*, vol. 39, no. 15, p. 4372, Aug. 2014, doi: 10.1364/ol.39.004372.

[23] P. K. Upputuri, M. Krisnan, and M. Pramanik, “Microsphere enabled subdiffraction-limited optical-resolution photoacoustic microscopy: a simulation study,” *J Biomed Opt*, vol. 22, no. 4, p. 045001, Nov. 2016, doi: 10.1117/1.jbo.22.4.045001.

[24] P. C. Beard, “Transduction mechanisms of the Fabry-Perot polymer film sensing concept for wideband ultrasound detection,” *IEEE Trans Ultrason Ferroelectr Freq Control*, vol. 46, no. 6, pp. 1575–1582, 1999, doi: 10.1109/58.808883.

[25] “s41377-018-0036-7”.

[26] J. Buchmann *et al.*, “Characterization and modeling of Fabry–Perot ultrasound sensors with hard dielectric mirrors for photoacoustic imaging,” *Appl Opt*, vol. 56, no. 17, p. 5039, Jun. 2017, doi: 10.1364/ao.56.005039.

[27] P. C. Beard and T. N. Mills, “Extrinsic optical-fiber ultrasound sensor using a thin polymer film as a low-finesse Fabry-Perot interferometer.”

[28] B. T. Cox and P. C. Beard, "The frequency-dependent directivity of a planar Fabry-Perot polymer film ultrasound sensor," *IEEE Trans Ultrason Ferroelectr Freq Control*, vol. 54, no. 2, pp. 394–404, Feb. 2007, doi: 10.1109/TUFFC.2007.253.

[29] S. v. Thathachary and S. Ashkenazi, "Performance improvement of an all-optical Fabry Perot ultrasound detector," in *Optical Fibers and Sensors for Medical Diagnostics and Treatment Applications XVII*, Feb. 2017, vol. 10058, p. 100580M. doi: 10.1117/12.2250979.

[30] J. Batey and E. Tierney, "Low-temperature deposition of high-quality silicon dioxide by plasma-enhanced chemical vapor deposition," *J Appl Phys*, vol. 60, no. 9, pp. 3136–3145, 1986, doi: 10.1063/1.337726.

[31] M. Golda-Cepa, K. Engvall, M. Hakkarainen, and A. Kotarba, "Recent progress on parylene C polymer for biomedical applications: A review," *Progress in Organic Coatings*, vol. 140. Elsevier B.V., Mar. 01, 2020. doi: 10.1016/j.porgcoat.2019.105493.

[32] C. Stefanadis, C. K. Antoniou, D. Tsiachris, and P. Pietri, "Coronary atherosclerotic vulnerable plaque: Current perspectives," *Journal of the American Heart Association*, vol. 6, no. 3. John Wiley and Sons Inc., Mar. 01, 2017. doi: 10.1161/JAHA.117.005543.

[33] T. Ma, B. Zhou, T. K. Hsiai, and K. K. Shung, "A review of intravascular ultrasound-based multimodal intravascular imaging: The synergistic approach to characterizing vulnerable plaques," *Ultrason Imaging*, vol. 38, no. 5, pp. 314–331, Sep. 2016, doi: 10.1177/0161734615604829.

[34] A. M. Zysk, F. T. Nguyen, A. L. Oldenburg, D. L. Marks, and S. A. Boppart, "Optical coherence tomography: a review of clinical development from bench to bedside," *J Biomed Opt*, vol. 12, no. 5, p. 051403, 2007, doi: 10.1117/1.2793736.

[35] B. A. Flusberg *et al.*, “High-speed, miniaturized fluorescence microscopy in freely moving mice,” *Nat Methods*, vol. 5, no. 11, pp. 935–938, 2008, doi: 10.1038/nmeth.1256.

[36] “Method of the Year 2018: Imaging in freely behaving animals,” *Nature Methods*, vol. 16, no. 1. Nature Publishing Group, Jan. 01, 2019. doi: 10.1038/s41592-018-0292-8.

[37] Q. Fan *et al.*, “Perylene-diimide-based nanoparticles as highly efficient photoacoustic agents for deep brain tumor imaging in living mice,” *Advanced Materials*, vol. 27, no. 5, pp. 843–847, Feb. 2015, doi: 10.1002/adma.201402972.

[38] M. Mozaffarzadeh, Y. Yan, M. Mehrmohammadi, and B. Makkiabadi, “Enhanced linear-array photoacoustic beamforming using modified coherence factor,” *J Biomed Opt*, vol. 23, no. 02, p. 1, Feb. 2018, doi: 10.1117/1.jbo.23.2.026005.

[39] D. Wang, Y. Wang, Y. Zhou, J. F. Lovell, and J. Xia, “Coherent-weighted three-dimensional image reconstruction in linear-array-based photoacoustic tomography,” *Biomed Opt Express*, vol. 7, no. 5, p. 1957, May 2016, doi: 10.1364/boe.7.001957.

[40] M. Xu and L. v. Wang, “Universal back-projection algorithm for photoacoustic computed tomography,” *Phys Rev E Stat Nonlin Soft Matter Phys*, vol. 71, no. 1, Jan. 2005, doi: 10.1103/PhysRevE.71.016706.

[41] D. Finch, M. Haltmeier, and Rakesh, “Inversion of spherical means and the wave equation in even dimensions,” *SIAM J Appl Math*, vol. 68, no. 2, pp. 392–412, 2007, doi: 10.1137/070682137.

[42] B. E. Treeby, J. Jaros, A. P. Rendell, and B. T. Cox, “ Modeling nonlinear ultrasound propagation in heterogeneous media with power law absorption using a k -space pseudospectral method ,” *J Acoust Soc Am*, vol. 131, no. 6, pp. 4324–4336, Jun. 2012, doi: 10.1121/1.4712021.

[43] B. E. Treeby, E. Z. Zhang, and B. T. Cox, “Photoacoustic tomography in absorbing acoustic media using time reversal,” *Inverse Probl*, vol. 26, no. 11, 2010, doi: 10.1088/0266-5611/26/11/115003.

[44] S. Park, A. B. Karpiouk, S. R. Aglyamov, and S. Y. Emelianov, “Adaptive beamforming for photoacoustic imaging,” 2008.

[45] M. Mozaffarzadeh, “Linear-array photoacoustic imaging using minimum variance-based delay multiply and sum adaptive beamforming algorithm,” *J Biomed Opt*, vol. 23, no. 02, p. 1, Feb. 2018, doi: 10.1117/1.jbo.23.2.026002.

[46] D. Allman, A. Reiter, and M. A. L. Bell, “Photoacoustic Source Detection and Reflection Artifact Removal Enabled by Deep Learning,” *IEEE Trans Med Imaging*, vol. 37, no. 6, pp. 1464–1477, Jun. 2018, doi: 10.1109/TMI.2018.2829662.

[47] M. T. Graham and M. A. L. Bell, “Photoacoustic Spatial Coherence Theory and Applications to Coherence-Based Image Contrast and Resolution,” *IEEE Trans Ultrason Ferroelectr Freq Control*, vol. 67, no. 10, pp. 2069–2084, Oct. 2020, doi: 10.1109/TUFFC.2020.2999343.

[48] J. Camacho, M. Parrilla, and C. Fritsch, “Phase coherence imaging,” *IEEE Trans Ultrason Ferroelectr Freq Control*, vol. 56, no. 5, pp. 958–974, May 2009, doi: 10.1109/TUFFC.2009.1128.

[49] G. Matrone, A. S. Savoia, G. Caliano, and G. Magenes, “The delay multiply and sum beamforming algorithm in ultrasound B-mode medical imaging,” *IEEE Trans Med Imaging*, vol. 34, no. 4, pp. 940–949, Apr. 2015, doi: 10.1109/TMI.2014.2371235.

[50] H. Been Lim, N. Thi Tuyet Nhung, E. P. Li, and N. Duc Thang, “Confocal microwave imaging for breast cancer detection: Delay-multiply-and-sum image reconstruction

algorithm," *IEEE Trans Biomed Eng*, vol. 55, no. 6, pp. 1697–1704, Jun. 2008, doi: 10.1109/TBME.2008.919716.

[51] M. A. Lediju, G. E. Trahey, B. C. Byram, and J. J. Dahl, "Short-lag spatial coherence of backscattered echoes: Imaging characteristics," *IEEE Trans Ultrason Ferroelectr Freq Control*, vol. 58, no. 7, pp. 1377–1388, 2011, doi: 10.1109/TUFFC.2011.1957.

[52] S. Jeon, E. Y. Park, W. Choi, R. Managuli, K. jong Lee, and C. Kim, "Real-time delay-multiply-and-sum beamforming with coherence factor for in vivo clinical photoacoustic imaging of humans," *Photoacoustics*, vol. 15, Sep. 2019, doi: 10.1016/j.pacs.2019.100136.

[53] E. Gonzalez, A. Wiacek, and M. A. Lediju Bell, "Visualization of custom drill bit tips in a human vertebra for photoacoustic-guided spinal fusion surgeries," Feb. 2019, p. 205. doi: 10.1117/12.2510688.

[54] E. Gonzalez, A. Wiacek, and M. A. Lediju Bell, "Visualization of custom drill bit tips in a human vertebra for photoacoustic-guided spinal fusion surgeries," Feb. 2019, p. 205. doi: 10.1117/12.2510688.

[55] E. Gonzalez and M. A. L. Bell, "Segmenting Bone Structures in Ultrasound Images with Locally Weighted SLSC (LW-SLSC) Beamforming," in *IEEE International Ultrasonics Symposium, IUS*, 2018, vol. 2018-January. doi: 10.1109/ULTSYM.2018.8579732.

[56] A. A. Nair, T. D. Tran, and M. A. L. Bell, "Robust Short-Lag Spatial Coherence Imaging," *IEEE Trans Ultrason Ferroelectr Freq Control*, vol. 65, no. 3, pp. 366–377, Mar. 2018, doi: 10.1109/TUFFC.2017.2780084.

[57] E. Gonzalez, A. Wiacek, and M. A. Lediju Bell, “Visualization of custom drill bit tips in a human vertebra for photoacoustic-guided spinal fusion surgeries,” Feb. 2019, p. 205. doi: 10.1117/12.2510688.

[58] E. Gonzalez and M. A. L. Bell, “Segmenting Bone Structures in Ultrasound Images with Locally Weighted SLSC (LW-SLSC) Beamforming,” in *IEEE International Ultrasonics Symposium, IUS*, 2018, vol. 2018-January. doi: 10.1109/ULTSYM.2018.8579732.

[59] M. Mozaffarzadeh, S. R. Miri Rostami, A. . Hariri, J. v. Jokerst, and M. Ghaffari-Miab, “OpenACC GPU implementation of double-stage delay-multiply-and-sum algorithm: toward enhanced real-time linear-array photoacoustic tomography,” Feb. 2019, p. 195. doi: 10.1117/12.2511115.

[60] M. A. Lediju Bell, N. P. Kuo, D. Y. Song, J. U. Kang, and E. M. Boctor, “In vivo visualization of prostate brachytherapy seeds with photoacoustic imaging ,” *J Biomed Opt*, vol. 19, no. 12, p. 126011, Dec. 2014, doi: 10.1117/1.jbo.19.12.126011.

[61] Y. Lin, R. Zheng, X. Zhang, Z. Li, and H. Li, “Image enhancement of photoacoustic imaging for early endometrial cancer detection by employing a filtered delay multiply and sum beamforming algorithm,” *AIP Adv*, vol. 9, no. 12, Dec. 2019, doi: 10.1063/1.5122891.

[62] M. A. Lediju Bell, N. Kuo, D. Y. Song, and E. M. Boctor, “Short-lag spatial coherence beamforming of photoacoustic images for enhanced visualization of prostate brachytherapy seeds,” *Biomed Opt Express*, vol. 4, no. 10, p. 1964, Oct. 2013, doi: 10.1364/boe.4.001964.

[63] G. Matrone and A. Ramalli, “Spatial coherence of backscattered signals in multi-line transmit ultrasound imaging and its effect on short-lag Filtered-Delay Multiply and Sum

beamforming," *Applied Sciences (Switzerland)*, vol. 8, no. 4, Mar. 2018, doi: 10.3390/app8040486.

[64] G. Matrone, A. Ramalli, A. S. Savoia, P. Tortoli, and G. Magenes, "High frame-rate, high resolution ultrasound imaging with multi-line transmission and filtered-delay multiply and sum beamforming," *IEEE Trans Med Imaging*, vol. 36, no. 2, pp. 478–486, Feb. 2017, doi: 10.1109/TMI.2016.2615069.

[65] J. Tordera Mora, X. Feng, N. Nyayapathi, J. Xia, and L. Gao, "Generalized spatial coherence reconstruction for photoacoustic computed tomography," *J Biomed Opt*, vol. 26, no. 04, Apr. 2021, doi: 10.1117/1.jbo.26.4.046002.

[66] D. Hyun, A. L. C. Crowley, and J. J. Dahl, "Efficient Strategies for Estimating the Spatial Coherence of Backscatter," *IEEE Trans Ultrason Ferroelectr Freq Control*, vol. 64, no. 3, pp. 500–513, Mar. 2017, doi: 10.1109/TUFFC.2016.2634004.

[67] B. Stephanian, M. T. Graham, H. Hou, and M. A. Lediju Bell, "Additive noise models for photoacoustic spatial coherence theory," *Biomed Opt Express*, vol. 9, no. 11, p. 5566, Nov. 2018, doi: 10.1364/boe.9.005566.

[68] "Preface."

[69] C. Martinoli *et al.*, "Power Doppler sonography: clinical applications," 1998.

[70] K. M. Kempski, M. T. Graham, M. R. Gubbi, T. Palmer, and M. A. Lediju Bell, "Application of the generalized contrast-to-noise ratio to assess photoacoustic image quality," *Biomed Opt Express*, vol. 11, no. 7, p. 3684, Jul. 2020, doi: 10.1364/boe.391026.

[71] A. Rodriguez-Molares *et al.*, "The Generalized Contrast-to-Noise Ratio: A Formal Definition for Lesion Detectability," *IEEE Trans Ultrason Ferroelectr Freq Control*, vol. 67, no. 4, pp. 745–759, Apr. 2020, doi: 10.1109/TUFFC.2019.2956855.

[72] B. E. Treeby and B. T. Cox, “k-Wave: MATLAB toolbox for the simulation and reconstruction of photoacoustic wave fields,” *J Biomed Opt*, vol. 15, no. 2, p. 021314, 2010, doi: 10.1117/1.3360308.

[73] “preview_ANSI+Z136.3-2018”.

[74] Y. Wang, R. S. A. Lim, H. Zhang, N. Nyayapathi, K. W. Oh, and J. Xia, “Optimizing the light delivery of linear-array-based photoacoustic systems by double acoustic reflectors,” *Sci Rep*, vol. 8, no. 1, Dec. 2018, doi: 10.1038/s41598-018-31430-5.

[75] N. Nyayapathi *et al.*, “Dual Scan Mammoscope (DSM) - A New Portable Photoacoustic Breast Imaging System with Scanning in Craniocaudal Plane,” *IEEE Trans Biomed Eng*, vol. 67, no. 5, pp. 1321–1327, May 2020, doi: 10.1109/TBME.2019.2936088.

[76] Y. Wang, Y. Zhan, M. Tiao, and J. Xia, “Review of methods to improve the performance of linear array-based photoacoustic tomography,” *Journal of Innovative Optical Health Sciences*, vol. 13, no. 2. World Scientific Publishing Co. Pte Ltd, Mar. 01, 2020. doi: 10.1142/S1793545820300037.

[77] E. A. Gonzalez and M. A. L. Bell, “GPU implementation of photoacoustic short-lag spatial coherence imaging for improved image-guided interventions,” *J Biomed Opt*, vol. 25, no. 07, p. 1, Jul. 2020, doi: 10.1117/1.jbo.25.7.077002.

[78] A. Wiacek, K. C. Wang, H. Wu, and M. Bell, “Dual-wavelength photoacoustic imaging for guidance of hysterectomy procedures,” Feb. 2020, p. 44. doi: 10.1117/12.2544906.

[79] A. Wiacek, K. C. Wang, H. Wu, and M. A. L. Bell, “Photoacoustic-Guided Laparoscopic and Open Hysterectomy Procedures Demonstrated with Human Cadavers,” *IEEE Trans Med Imaging*, vol. 40, no. 12, pp. 3279–3292, Dec. 2021, doi: 10.1109/TMI.2021.3082555.

[80] K. Sivasubramanian, “Hand-held, clinical dual mode ultrasound-photoacoustic imaging of rat urinary bladder and its applications,” 2018, doi: 10.13039/501100001459.

[81] K. Sivasubramanian, “Hand-held, clinical dual mode ultrasound-photoacoustic imaging of rat urinary bladder and its applications,” 2018, doi: 10.13039/501100001459.

[82] N. Nyayapathi and J. Xia, “Photoacoustic imaging of breast cancer: a mini review of system design and image features,” *J Biomed Opt*, vol. 24, no. 12, p. 1, Nov. 2019, doi: 10.1117/1.jbo.24.12.121911.

[83] M. S. Singh and A. Thomas, “Photoacoustic elastography imaging: a review,” *J Biomed Opt*, vol. 24, no. 04, p. 1, Apr. 2019, doi: 10.1117/1.jbo.24.4.040902.

[84] B. Yao *et al.*, “High-speed, whole-column fluorescence imaging detection for isoelectric focusing on a microchip using an organic light emitting diode as light source,” *Anal Chem*, vol. 78, no. 16, pp. 5845–5850, Aug. 2006, doi: 10.1021/ac060445r.

[85] J. L. Fan *et al.*, “High-speed volumetric two-photon fluorescence imaging of neurovascular dynamics,” *Nat Commun*, vol. 11, no. 1, Dec. 2020, doi: 10.1038/s41467-020-19851-1.

[86] J. L. Fan *et al.*, “High-speed volumetric two-photon fluorescence imaging of neurovascular dynamics,” *Nat Commun*, vol. 11, no. 1, Dec. 2020, doi: 10.1038/s41467-020-19851-1.

[87] R. Wolleschensky, B. Zimmermann, and M. Kempe, “High-speed confocal fluorescence imaging with a novel line scanning microscope,” *J Biomed Opt*, vol. 11, no. 6, p. 064011, 2006, doi: 10.1117/1.2402110.

[88] J. v. Thompson, J. D. Mason, H. T. Beier, and J. N. Bixler, “High speed fluorescence imaging with compressed ultrafast photography,” in *High-Speed Biomedical Imaging and*

*Spectroscopy: Toward Big Data Instrumentation and Management II*, Feb. 2017, vol. 10076, p. 1007613. doi: 10.1117/12.2251025.

[89] C. A. Werley, M.-P. Chien, and A. E. Cohen, "Ultrawidefield microscope for high-speed fluorescence imaging and targeted optogenetic stimulation," *Biomed Opt Express*, vol. 8, no. 12, p. 5794, Dec. 2017, doi: 10.1364/boe.8.005794.

[90] H. P. Joon, V. Pieribone, D. Kim, J. V. Verhagen, C. von Hehn, and E. Culurciello, "High-speed fluorescence imaging system for freely moving animals," in *Proceedings - IEEE International Symposium on Circuits and Systems*, 2009, pp. 2429–2432. doi: 10.1109/ISCAS.2009.5118291.

[91] J. v. Thompson, J. D. Mason, H. T. Beier, and J. N. Bixler, "High speed fluorescence imaging with compressed ultrafast photography," in *High-Speed Biomedical Imaging and Spectroscopy: Toward Big Data Instrumentation and Management II*, Feb. 2017, vol. 10076, p. 1007613. doi: 10.1117/12.2251025.

[92] R. Ng and P. M. Hanrahan, "Digital Correction of Lens Aberrations In Light Field Photography," 2006.

[93] R. Ng, "Fourier Slice Photography," 2005.

[94] R. Ng, M. Levoy, M. Brédif, G. Duval, M. Horowitz, and P. Hanrahan, "Light Field Photography with a Hand-held Plenoptic Camera." [Online]. Available: https://hal.archives-ouvertes.fr/hal-02551481

[95] M. Levo, R. Ng, A. Adams, M. Footer, and M. Horowitz, "Light Field Microscopy," 2006.

[96] T. Schrödel, R. Prevedel, K. Aumayr, M. Zimmer, and A. Vaziri, “Brain-wide 3D imaging of neuronal activity in Caenorhabditis elegans with sculpted light,” *Nat Methods*, vol. 10, no. 10, pp. 1013–1020, Oct. 2013, doi: 10.1038/nmeth.2637.

[97] L. Bai *et al.*, “Volumetric Imaging of Neural Activity by Light Field Microscopy,” *Neuroscience Bulletin*. Springer, 2022. doi: 10.1007/s12264-022-00923-9.

[98] Y.-G. Yoon *et al.*, “Sparse decomposition light-field microscopy for high speed imaging of neuronal activity,” *Optica*, vol. 7, no. 10, p. 1457, Oct. 2020, doi: 10.1364/optica.392805.

[99] M. A. Taylor, T. Nöbauer, A. Pernia-Andrade, F. Schlumm, and A. Vaziri, “Brain-wide 3D light-field imaging of neuronal activity with speckle-enhanced resolution,” *Optica*, vol. 5, no. 4, p. 345, Apr. 2018, doi: 10.1364/optica.5.000345.

[100] X. Feng and L. Gao, “Ultrafast light field tomography for snapshot transient and non-line-of-sight imaging,” *Nat Commun*, vol. 12, no. 1, Dec. 2021, doi: 10.1038/s41467-021-22461-0.

[101] M. E. Davison, “THE ILL-CONDITIONED NATURE OF THE LIMITED ANGLE TOMOGRAPHY PROBLEM*,” 1983. [Online]. Available: https://epubs.siam.org/terms-privacy

[102] H. Villarraga-Gómez and S. T. Smith, “Effect of the number of projections on dimensional measurements with X-ray computed tomography,” *Precis Eng*, vol. 66, pp. 445–456, Nov. 2020, doi: 10.1016/j.precisioneng.2020.08.006.

[103] A. Buratti, M. Ferrucci, S. ben Achour, W. Dewulf, and R. H. Schmitt, “An analytical method for optimizing imaging parameters in industrial x-ray computed tomography for

dimensional measurements on multimaterial workpieces," in *Developments in X-Ray Tomography X*, Oct. 2016, vol. 9967, p. 99671C. doi: 10.1117/12.2240566.

[104] G. Wu *et al.*, "Light Field Image Processing: An Overview," *IEEE Journal on Selected Topics in Signal Processing*, vol. 11, no. 7. Institute of Electrical and Electronics Engineers Inc., pp. 926–954, Oct. 01, 2017. doi: 10.1109/JSTSP.2017.2747126.

[105] Y. Boykov, O. Veksler, and R. Zabih, "Fast Approximate Energy Minimization via Graph Cuts."

[106] Y. Y. Schechner and N. Kiryati, "Depth from Defocus vs. Stereo: How Different Really are They?," 1998.

[107] S. Zhu, A. Lai, K. Eaton, P. Jin, and L. Gao, "On the fundamental comparison between unfocused and focused light field cameras," *Appl Opt*, vol. 57, no. 1, p. A1, Jan. 2018, doi: 10.1364/ao.57.0000a1.

[108] A. Lumsdaine and T. Georgiev, "The focused plenoptic camera," in *2009 IEEE International Conference on Computational Photography, ICCP 09*, 2009. doi: 10.1109/ICCPHOT.2009.5559008.

[109] M. Bertero, P. Boccacci, and C. de MoI, "Introduction to Inverse Problems in Imaging; Second Edition."

[110] A. Beck and M. Teboulle, "A fast iterative shrinkage-thresholding algorithm for linear inverse problems," *SIAM J Imaging Sci*, vol. 2, no. 1, pp. 183–202, 2009, doi: 10.1137/080716542.

[111] Y. LeCun, L. Bottou, Y. Bengio, and P. Haffner, "Gradient-based learning applied to document recognition," *Proceedings of the IEEE*, vol. 86, no. 11, pp. 2278–2323, 1998, doi: 10.1109/5.726791.

[112] M. U. Ghani and W. C. Karl, "Deep Learning-Based Sinogram Completion for Low-Dose CT," in *2018 IEEE 13th Image, Video, and Multidimensional Signal Processing Workshop, IVMSP 2018 - Proceedings*, Aug. 2018. doi: 10.1109/IVMSPW.2018.8448403.

[113] D. Lee, S. Choi, and H. J. Kim, "High quality imaging from sparsely sampled computed tomography data with deep learning and wavelet transform in various domains," *Med Phys*, vol. 46, no. 1, pp. 104–115, Jan. 2019, doi: 10.1002/mp.13258.

[114] H. Chen *et al.*, "LEARN: Learned Experts' Assessment-Based Reconstruction Network for Sparse-Data CT," *IEEE Trans Med Imaging*, vol. 37, no. 6, pp. 1333–1347, Jun. 2018, doi: 10.1109/TMI.2018.2805692.

[115] Y. Han and J. C. Ye, "Framing U-Net via Deep Convolutional Framelets: Application to Sparse-View CT," *IEEE Trans Med Imaging*, vol. 37, no. 6, pp. 1418–1429, Jun. 2018, doi: 10.1109/TMI.2018.2823768.

[116] A. Zheng, H. Gao, L. Zhang, and Y. Xing, "A dual-domain deep learning-based reconstruction method for fully 3D sparse data helical CT," *Phys Med Biol*, vol. 65, no. 24, Dec. 2020, doi: 10.1088/1361-6560/ab8fc1.